Inversion of time-lapse seismic waveform data using integral equation methods

Lars André Fardal Refsland

A thesis for the degree
Master of Science in Petroleum Geophysics

Department of Earth Science
University of Bergen

June 2018

Abstract

Time-lapse seismic data are considered a valuable tool for monitoring hydrocarbon reservoirs. Since the changes in elastic parameters associated with production of hydrocarbons, or injection of CO_2 into a reservoir, tend to be relatively small compared to that of the geological surroundings, scattering integral equation methods have been chosen for the task of modelling time-lapse seismic data. Full waveform inversion (FWI) is a comprehensive imaging technique that employs all of the information contained in seismic data, including travel times, amplitudes, internal multiples and diffractions. This was first performed using the distorted Born iterative T-matrix (DBIT) method, an iterative inversion approach that solved linear inverse problems at every iteration. This method has been performed on two models. Two time-lapse experiments was performed using a sequential strategy. First a time-lapse effect was reconstructed on a simple 2D reservoir model. This was followed by a demonstration of the time-lapse inversion of a re-sampled version of the Marmousi model. For future applications in ensemble based history matching, a linear Bayesian approach, using the distorted Born approximation, has been examined. The inversion process was linearised around a reconstructed inhomogeneous baseline model, for which Green's functions were calculated. The distorted Born approximation was then used with explicit Bayesian expressions, resulting in a maximum a posteriori (MAP) solution of time-lapse effect. Posterior uncertainties were also obtained. The Bayesian inversion method has been tested in two different time-lapse scenarios. First the Marmousi model was introduced with a relatively large time-lapse velocity change. The linear Bayesian time-lapse inversion was also tested on a smaller contrast. The DBIT method did prove to be able to reconstruct both models to a satisfying degree. The linear Bayesian time-lapse inversion was also able to reconstruct a time-lapse effect in the Marmousi model, even with a high level of noise.

Acknowledgments

I would like to thank my main supervisor, Prof. Morten Jakobsen, of whom I am in great debt to for many reasons. First of all for being patient when introducing me to the world of scattering theory, and always providing motivation and encouragement to continue researching. Also, I would like to show my appreciation to him, for always having time to meetings and discussions at least once every week. It was only through his inspiring character, excellent way of problem solving, and not less his guidance and professional advice along the way, that this work was made possible to accomplish.

I also owe a great deal to PhD Candidate, Xingguo Huang, first for providing the MATLAB code to the DBIT method. I am also very grateful to him for taking his time for discussions and providing suggestions that were implemented in this thesis.

Next I would like to thank Geir Nævdal, Kjersti Solberg Eikrem and all of your colleges at IRIS, for allowing me to join your meeting group. To be able to present my work in front of you and the opportunity to listen in on your discussions and present research, gave me an incredible motivation for continuing my experiments and to expand the work to also include Bayesian formulations.

I would like to thank my friends, and fellow students at UiB, for all the good times we have had.

Lastly, I would like to show my appreciation to my entire family, and especially to my parents, for always showing love and continuous support.

Contents

List of Figures

List of abbreviations

2D Two-dimensional

3D Three-dimensional

AVO Amplitude versus offset

FWI Full waveform inversion

BIT Born iterative T-matrix

DBIT Distorted Born iterative T-matrix

MVN Multivariate normal (distribution)

MAP Maximum a posteriori

Chapter 1

Introduction

A seismic trace is the recording of ground motion caused by a source, for example an explosion, and is a function of time. Furthermore, a seismogram can be described as a finite number of individual amplitude signals that each show the receiver's response to ground motion caused by the emitted seismic wave. Using knowledge about how a seismic wave behave in a media of certain physical properties, geophysicists and geologists can study the seismograms and make interpretations of structures in the sub-surface that the seismic wave has propagated through. Multiple source and receiver combinations make up a seismic survey and can provide detailed insight to the geology of the sub-surface. Seismic surveying has been extensively used in the petroleum industry to study areas of expected hydrocarbon discoveries. Furthermore, it has been used to monitor changes over time in oil and gas reservoirs during production. In order to observe changes in a petroleum reservoir, seismic data at different time steps of the production can be compared. This is often referred to in literature as time-lapse seismic data (sometimes repeated seismic or 4D seismic) and is well established in the oil and gas industry. It is important to note that the term 4D seismic data is often used to describe multiple 3D seismic data sets at different time steps corresponding to the different stages of oil or gas production. In order to prevent confusion, the term *time-lapse* is used in this thesis to indicate the comparison of spatial 2D sets at different time steps. As a consequence of hydrocarbon production, reservoir parameters, like fluid saturation, pore pressure, and thickness of the reservoir, may change (Landrø, 2010). Time-lapse analysis has thus become an important tool for locating remaining oil pockets and water-flooded areas so that high production rates are retained. This is especially crucial for mature oil and gas fields that have already been under production for a couple of decades. Additionally, a growing ambition has been witnessed to capture and store CO2 in sub-surface reservoirs due to its effects on oceans and atmosphere. Also these reservoirs can be monitored using time-lapse seismic data (Muhumuza, 2015; Muhumuza et al., 2018).

A reservoir model contains a set of numerical variables describing some physical properties of the system, for instance saturation and porosity. The process of updating a reservoir model is called history matching. Even today, history matching is considered a difficult task. The process can be described as the estimation of a set of reservoir model variables based on its observed behaviour (Oliver and Chen, 2011; Eikrem et al., 2016). In order to achieve this, history matching strives to quantitatively integrate production data and time-lapse seismic data. Using theories given by rock physics, one can be able to use information about seismic elastic parameters, to draw conclusions about important reservoir parameters (see for example Guéguen and Palciauskas, 1994; Landrø, 2010). Ensemble based history matching methods represents the probability distribution for the state of a reservoir (see for example Oliver and Chen, 2011; Eikrem et al., 2016). Since the use of such stochastic methods has increased lately, a Bayesian formulation of time-lapse seismic data could prove to be beneficial.

Traditionally, time-lapse seismic data are based on changes in travel-time or amplitude versus offset (AVO) analyses (Landrø, 2001). These seismic data have undergone different amount of data processing steps, for example migration and stacking procedures, hence the time-lapse data are then affected by uncertainties associated with these data manipulations (for example error in the velocity models of migration). The promising methods of full waveform inversion (FWI) techniques (see for example Tarantola, 1984; Pratt, 1999; Virieux and Operto, 2009; Jakobsen, 2012; Jakobsen and Ursin, 2015; Asnaashari et al., 2015), operates on the pre-processed (raw) seismic data that remains untouched by errors produced in different processing steps. Furthermore, FWI makes use of all the information in seismic data. This includes travel times, amplitudes, internal multiples and diffractions (Jakobsen and Ursin, 2015). FWI would then appear quite attractive for model reconstruction and time-lapse analysis. Due to its huge computational cost, FWI has been of somewhat limited practical use in the past. During the last couple of decades, however, there has been progress in the field of computational sciences and development of more powerful computers. Because of that and a growing demand of higher image quality, FWI methods are presently becoming more appealing.

Seismic FWI can be performed in time-domain or in frequency domain (Virieux and Operto, 2009). One way of dealing with the computational cost in the latter approach, is to only invert for a limited set of frequencies. Since there is a redundancy of information contained in different frequencies, the computational cost of the inversion process in frequency domain could be reduced by choosing a limited set of frequencies for inversion. Jakobsen and Ursin (2015) have developed two direct iterative inverse scattering methods, namely the Born Iterative T-matrix (BIT) and distorted Born iterative T-matrix (DBIT) methods. Both are modified versions of the Born iterative and distorted Born iterative methods that were originally developed for electromagnetic inverse scattering problems (Wang and Chew, 1989; Chew and Wang, 1990). However, scattering theory could also provide a means of calculating the scattered seismic wave-field that originates from a perturbation in the elastic medium parameters, for example velocity. This perturbation could for example originate from time-lapse changes in a reservoir. For that reason, scattering integral equations was a natural choice of methods to assign for the task of modelling full seismic waveforms and inverting time-lapse seismic data.

Thesis objective

The objective of this thesis, is to study seismic waveform modelling based on integral equation methods by performing seismic FWI using deterministic and Bayesian formulations of the inverse problem. The two methods provide fundamentally different estimates of the model parameters. Thus, a comparison of the results would be beneficial and could contribute to the research on seismic imaging. The objective will be reached by performing a set of numerical experiments where the presented methods have been implemented in the essential study of time-lapse analysis.

Thesis overview

The thesis consists of 6 chapters, in which the structure is such that each chapters containing numerical experiments are treated individually with introductory text, methodology, numerical experiment(s) and discission. In the current chapter, Chapter 1, the reader has been presented with an introduction to time-lapse seismic problems and the main topics of this thesis. The motivation for developing this thesis, has been given. Following there will be an overview of the next chapters which briefly mentions the main topics discussed in each chapter.

In Chapter 2, the theory of seismic forward modelling using integral equation methods, will be presented. First, there will be a derivation of the Lippmann-Schwinger equation. This will be followed by the well known Born approximation. The integral equations will then be discretized, followed by a derivation of the T-matrix. At the end of the chapter, there will be a numerical experiment showing the synthetic seismic data calculated using Born approximation and exact integral T-matrix method in time domain for a time-lapse model.

In Chapter 3, the fundamentals of deterministic and Bayesian linear inverse theory and regularization of ill-posed problems will be covered. A simple example will be given in order to demonstrate the theory.

In Chapter 4, the deterministic inverse problem theory will be directed towards seismic waveform data, and the direct iterative integral method of DBIT will be derived. Then there will be a discussion of two inversion strategies to time-lapse seismic data, known as sequential- and double-difference strategies. In the end of the chapter, full waveform inversion using the DBIT method will be performed on time-lapse seismic data using the sequential strategy. This will first be done for a simple 2D model of a reservoir, followed by a time-lapse inversion of the Marmousi model.

In Chapter 5, the Bayesian inverse problem theory, presented in Chapter 3, will be applied on time-lapse seismic waveform data. An inverse Bayesian time-lapse method will be presented, and the theory will be demonstrated in a numerical experiment on two different time-lapse scenarios, the first which is equal to the time-lapse introduced in the Marmousi model of the previous chapter, and secondly, inversion of a much smaller time-lapse effect will be investigated.

In Chapter 6, the conclusions of the thesis is reviewed and followed by a final summary. The chapter also provides suggestions for future research that can expand beyond the framework of this thesis.

Chapter 2

Seismic waveform modelling

2.1 Introduction

Topic sentence Seismic forward modelling can be described as the calculation of wave-field propagation using the wave equation in a geological model with known seismic properties, like density and velocity. A seismogram is then response of a seismic wave on a receiver (e.g. geophone or hydrophone, for land or ocean seismic surveys) for a given source-receiver distribution. A synthetic seismogram can be made by calculating the wave-field in a given position over time, or in frequency domain by use of the FFT (fast Fourier transform)-method. Some commonly used methods for seismic modelling are ray tracing (RT), finite difference (FD) and integral equation methods (Schuster, 2017; Virieux and Operto, 2009; Sayers and Chopra, 2009; Krebes, 2004). The focus of this thesis will be on the scattering integral method.

In this chapter there will first be a presentation of Green's functions and how they are used to solve the acoustic wave-equation. In Section 2.3 the Lippmann-Schwinger (LS) equation will be derived in the acoustic approximation. Section 2.4 will show an approximate solution of the LS equation, namely Born approximation. In Section 2.5, the exact of these two techniques will be rewritten into matrix notation for implementation on a computer, followed by the derivation of the T-matrix in Section 2.6. In the end of this chapter, numerical examples of forward modelling will be given using Born approximation and the exact integral T-matrix method.

2.2 The acoustic wave equation and Green's functions

If one assumes the earth to have a constant density, the wave propagation of P-waves is described by the acoustic wave equation (Auld, 1973)

$$\left(\nabla^2 - \frac{1}{c^2(\boldsymbol{x})}\frac{\partial^2}{\partial t^2}\right)\Psi(\boldsymbol{x},t) = -F_s(\boldsymbol{x},t). \tag{2.1}$$

In Equation 2.1, ∇^2 is the Laplace operator, $\Psi(\boldsymbol{x},t)$ is the seismic (pressure) wave-field at position $\boldsymbol{x}$ and time t, $c(\boldsymbol{x})$ is the P-wave velocity and $F_s(\boldsymbol{x},t)$ is the source function. In this thesis, the acoustic wave equation is used instead of the elastic wave equation for reduction of computational cost and easy implementation. The time-independent Helmholtz equation in frequency domain is found by applying the Fourier transform on Equation 2.1, resulting in

$$L(\boldsymbol{x},\omega)\psi(\boldsymbol{x},\omega) = -f_s(\boldsymbol{x},\omega), \tag{2.2}$$

where the wave operator $L(\boldsymbol{x},\omega)$ is given by

$$L(\boldsymbol{x},\omega) = \nabla^2 + k^2(\boldsymbol{x},\omega). \tag{2.3}$$

In Equation 2.2, $\psi(\boldsymbol{x},\omega)$ and $f_s(\boldsymbol{x},\omega)$ is the Fourier transform of $\Psi(\boldsymbol{x},t)$ and $F_s(\boldsymbol{x},t)$, respectively. The wavenumber $k(\boldsymbol{x},w)$ is given by

$$k(\boldsymbol{x},\omega) = \frac{\omega}{c(\boldsymbol{x})}. \tag{2.4}$$

If the source function $f_s(\boldsymbol{x},\omega)$ in Equation 2.2 is a point source placed at $\boldsymbol{x}$ and oscillating with frequency ω, then there exists a fundamental solution to Equation 2.2 known as the Green's function $G(\boldsymbol{x},\boldsymbol{x'},\omega)$. Replacing the right-hand side of Equation 2.2 with the theoretical representation of a point source, given by the Dirac-delta function, it becomes (Morse and Feshback, 1953)

$$L(\boldsymbol{x},\omega)G(\boldsymbol{x},\boldsymbol{x'},\omega) = -\delta(\boldsymbol{x}-\boldsymbol{x'}). \tag{2.5}$$

Equation 2.5 defines the Green's function for the Helmholtz equation. Following Schuster (2017), the seismic wave-field in a homogeneous medium can be represented by the following volume integral over all space (see the condition of Sommerfeld radiation in Morse and

Feshback, 1953)

$$\psi(\boldsymbol{x},\omega) = \int G(\boldsymbol{x},\boldsymbol{x'},\omega) f_s(\boldsymbol{x'},\omega)\mathrm{d}\boldsymbol{x'}. \tag{2.6}$$

Explicit expressions for the Green's function for an outgoing wave in a homogeneous medium are given in one, two and tree dimensions, as (Snieder, 2004)

$$\begin{aligned} G^{1D}(\boldsymbol{x},\boldsymbol{x'}) &= -\frac{i}{2k} e^{ik|x-x'|}, \\ G^{2D}(\boldsymbol{x},\boldsymbol{x'}) &= -\frac{i}{4} H_0^{(1)}(k|\boldsymbol{x}-\boldsymbol{x'}|), \\ G^{3D}(\boldsymbol{x},\boldsymbol{x'}) &= \frac{1}{4\pi}\frac{e^{-ik|\boldsymbol{x}-\boldsymbol{x'}|}}{|\boldsymbol{x}-\boldsymbol{x'}|}. \end{aligned} \tag{2.7}$$

In the Green's function for the 2D case, $H_0^{(1)}$ is the first Hankel function of degree zero.

2.3 Seismic modelling using integral equation

The aim of this section is to derive an integral equation for the seismic wave-field in, namely the Lippmann-Schwinger (LS) equation, starting from the acoustic wave-equation in frequency domain(see for example Huang et al., 2018; Jakobsen and Wu, 2016; Jakobsen and Ursin, 2015; Jakobsen, 2012; Ikelle and Amundsen, 2005; Morse and Feshback, 1953). In general, the LS equation could be derived for any anisotropic visco-elastic media (see Appendix A of Jakobsen and Ursin, 2015). The first step is to decompose the wave operator $L(\boldsymbol{x},\omega)$ in Equation 2.2 as

$$L(\boldsymbol{x},\omega) = L^{(0)}(\boldsymbol{x},\omega) + \omega^2\chi(\boldsymbol{x}), \tag{2.8}$$

where $L^{(0)}(\boldsymbol{x},\omega) = \nabla^2 + k_0^2(\boldsymbol{x},\omega)$ is the wave operator associated with an arbitrary background medium (sometimes called a reference medium), and $\chi(\boldsymbol{x})$ is a contrast function given by

$$\chi(\boldsymbol{x}) = \frac{1}{c^2(\boldsymbol{x})} - \frac{1}{c_0^2(\boldsymbol{x})}. \tag{2.9}$$

The contrast function describes difference in slowness between the actual medium and background medium. The decomposition can be easily verified by substituting the definitions of $L^{(0)}(\boldsymbol{x},\omega)$ and $\chi(\boldsymbol{x})$ in to Equation 2.8 and see that $L(\boldsymbol{x},\omega)$ becomes $\nabla^2 + k^2(\boldsymbol{x},\omega)$. Next, the wave-field is decomposed into a field in the background medium, given by $\psi^{(0)}(\boldsymbol{x},\omega)$, and a scattered field (also named the perturbed field), given by $\Delta\psi(\boldsymbol{x},\omega)$. The total wave-field can now be written as

$$\psi(\boldsymbol{x},\omega) = \psi^{(0)}(\boldsymbol{x},\omega) + \Delta\psi(\boldsymbol{x},\omega). \tag{2.10}$$

If the velocity perturbation is set equal to zero, i.e. the velocity in the background medium is exactly the velocity of the actual medium, the solution to Equation 2.2 would be $\psi^{(0)}(\boldsymbol{x},\omega)$, and can be written as

$$L^{(0)}(\boldsymbol{x},\omega)\psi^{(0)}(\boldsymbol{x},\omega) = -f_s(\boldsymbol{x},\omega). \tag{2.11}$$

Using the source representation integral (Equation 2.6), the solution for the wave-field in the background medium is given by the following volume integral over the survey domain $\mathcal{D}$

$$\psi^{(0)}(\boldsymbol{x},\omega) = \int_{\mathcal{D}} G^{(0)}(\boldsymbol{x},\boldsymbol{x'},\omega) f_s(\boldsymbol{x'},\omega)\mathrm{d}\boldsymbol{x'}. \tag{2.12}$$

Here, the Green's function $G^{(0)}(\boldsymbol{x},\boldsymbol{x'},\omega)$, is associated with that of the (arbitrary) background medium. The next step is to find an expression for the scattered wavefield given by the contrast function, defined by Equation 2.9. Toward this goal, the wave operator $L(\boldsymbol{x},\omega)$, and the wave-field $\psi(\boldsymbol{x},\omega)$ in Equation 2.2, are substituted with the decomposed wave operator (Equation 2.8) and the decomposed wave-field (Equation 2.10), respectively. The result is the Helmholtz equation for a decomposed wavefield, within the background medium and the perturbated medium, written as

$$\left(L^{(0)}(\boldsymbol{x},\omega) + \omega^2\chi(\boldsymbol{x})\right)\left(\psi^{(0)}(\boldsymbol{x},\omega) + \Delta\psi(\boldsymbol{x},\omega)\right) = -f_s(\boldsymbol{x},\omega). \tag{2.13}$$

Using Equation 2.11, $f_s(\boldsymbol{x},\omega)$ is cancelled out from the equation above, and the relationship between $\Delta\psi(\boldsymbol{x},\omega)$ and $\chi(\boldsymbol{x})$ can now be rewritten as

$$L^{(0)}(\boldsymbol{x},\omega)\Delta\psi(\boldsymbol{x},\omega) = \omega^2\chi(\boldsymbol{x})\left(\psi^{(0)}(\boldsymbol{x},\omega) + \Delta\psi(\boldsymbol{x},\omega)\right). \tag{2.14}$$

Note that the factor $\psi^{(0)}(\boldsymbol{x},\omega) + \Delta\psi(\boldsymbol{x},\omega)$ on the right-hand-side of Equation 2.14 can be substituted with $\psi(\boldsymbol{x},\omega)$ using the definition of the decomposed wave-field (Equation 2.10). Since the product of the scattering potential $\chi(\boldsymbol{x})$ and the wave-field $\psi(\boldsymbol{x},\omega)$ represents a virtual source (Jakobsen, 2012), the source representation integral (Equation 2.6) can be used to re-write the scattered wave-field as the following volume integral

$$\Delta\psi(\boldsymbol{x},\omega) = \omega^2 \int_{\mathcal{D}} G^{(0)}(\boldsymbol{x},\boldsymbol{x'},\omega)\chi(\boldsymbol{x'})\psi(\boldsymbol{x'},\omega)\mathrm{d}\boldsymbol{x'}, \tag{2.15}$$

where the volume $\mathcal{D}$ is the domain in which the velocity perturbation is non-zero. Finally, using Equation 2.10 and 2.15, the well-known Lippmann-Schwinger equation for the total wave-field, $\psi(\boldsymbol{x},\omega)$, takes its form (Schuster, 2017; Jakobsen and Ursin, 2015; Ikelle and Amundsen, 2005)

$$\psi(\boldsymbol{x},\omega) = \psi^{(0)}(\boldsymbol{x},\omega) + \omega^2 \int_{\mathcal{D}} G^{(0)}(\boldsymbol{x},\boldsymbol{x'},\omega)\chi(\boldsymbol{x'})\psi(\boldsymbol{x'},\omega)\mathrm{d}\boldsymbol{x'}, \tag{2.16}$$

where $\psi^{(0)}(\boldsymbol{x},\omega)$ and $\chi(\boldsymbol{x})$ are given by Equation 2.12 and 2.9, respectively. The Green's function, $G^{(0)}(\boldsymbol{x},\boldsymbol{x'},\omega)$, in Equation 2.15 and 2.16 is associated with that of the background medium and is assumed to be known. In the case of a homogeneous background medium, analytical expressions for the Green's function exists and are given in Equation 2.7. The LS Equation (Equation 2.16) is the sum of the reference field and the scattered field from potential virtual sources, $\psi^{(0)}(\boldsymbol{x},\omega)$ and $\Delta\psi(\boldsymbol{x},\omega)$, respectively. All points in the defined volume are potentially virtual sources. If a point is defined with a non-zero scatter potential, and if it is illuminated by an incoming wave, a second wave (the scattered wave) starts propagating from the virtual source-point. This is called the scattering process, and is illustrated in Figure 2.1.

Untill now, it has been assumed that the Green's function for the background medium was known. For a homogeneous medium, explicit expresisons for the Green's function exists. In the case of an inhomogeneous, but smooth, background medium, the Green's function can be approximated using ray-theory (Cerveny, 2001). For an arbitrary heterogeneous background medium, the Green's function can be calculated numerically using the method of finite difference (Kirchner and Shapiro, 2001). The Green's functions for an arbitrary inhomogeneous background medium could also be calculated by the use of an integral equation for Green's functions. This will now be discussed further. From Equation 2.6, 2.12 and 2.16 it follows that the Green's function for a heterogeneous background medium $G(\boldsymbol{x},\boldsymbol{x}',\omega)$ can be expressed by the following Lippmann-Schwinger like integral equation (Jakobsen and

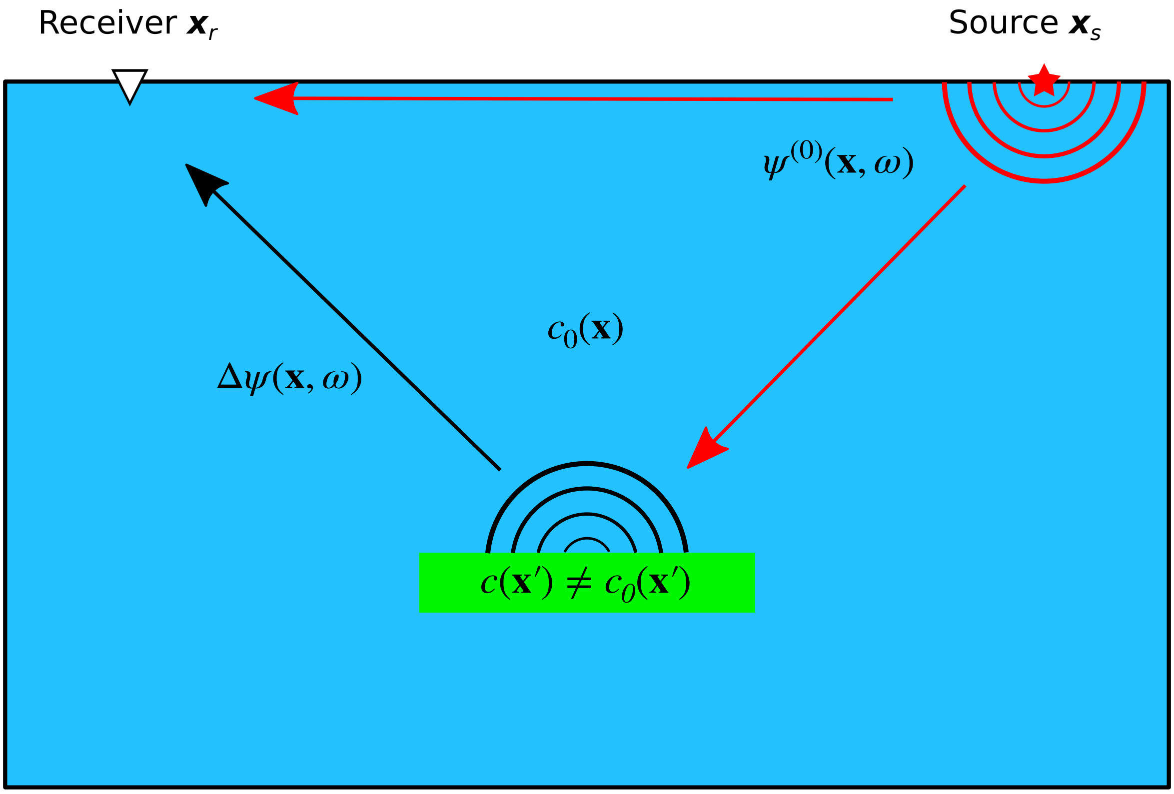

Figure 2.1: *Illustrative figure of the scattering problem. A wave-field (in red), generated by a source at position* $\boldsymbol{x}_s$*, propagates to the virtual source-point located at* $\boldsymbol{x}'$ *where the scatter potential is nonzero. An interaction causes the scatter-point to generate a second wave (in black), propagating away from position* $\boldsymbol{x}'$*. This wave is recorded by the receiver at* $\boldsymbol{x}_r$*, as the reflected wave from the scatter point.*

Ursin, 2015)

$$G(\boldsymbol{x},\boldsymbol{x}',\omega) = G^{(0)}(\boldsymbol{x},\boldsymbol{x}',\omega) + \omega^2 \int_{\mathcal{D}} G^{(0)}(\boldsymbol{x},\boldsymbol{x}'',\omega)\chi(\boldsymbol{x}'')G(\boldsymbol{x}'',\boldsymbol{x}',\omega)\mathrm{d}\boldsymbol{x}'', \tag{2.17}$$

where ω is the angular frequency and $G^{(0)}(\boldsymbol{x},\boldsymbol{x}',\omega)$ and are the Green's function associated with the homogeneous background medium, respectively. $\chi(\boldsymbol{x}'')$ is the perturbation describing the velocity contrast between the homogeneous and inhomogeneous background medium given by Equation 2.9. Equation 2.17 suggest that the Green's function in the background medium and actual medium are related through a multiple scattering process because of the velocity contrasts in the respective media. Following Jakobsen and Ursin (2015), Equation 2.16 and 2.17 can be rewritten exactly to the form of a product of continuous matrices, which is more appropriate for the purpose of discretization. Using the definition of Dirac's delta-function, this becomes

$$\psi(\boldsymbol{x},\omega) = \psi^{(0)}(\boldsymbol{x},\omega) + \int_{\mathcal{D}}\int_{\mathcal{D}} \bar{G}^{(0)}(\boldsymbol{x},\boldsymbol{x}_1)\tilde{V}(\boldsymbol{x}_1,\boldsymbol{x}_2)\psi(\boldsymbol{x}_2)\mathrm{d}\boldsymbol{x}_2\mathrm{d}\boldsymbol{x}_1 \tag{2.18}$$

and

$$\bar{G}(\boldsymbol{x},\boldsymbol{x}',\omega) = \bar{G}^{(0)}(\boldsymbol{x},\boldsymbol{x}',\omega) + \int_{\mathcal{D}}\int_{\mathcal{D}} \bar{G}^{(0)}(\boldsymbol{x},\boldsymbol{x}_1,\omega)\tilde{V}(\boldsymbol{x}_1,\boldsymbol{x}_2)\bar{G}(\boldsymbol{x}_2,\boldsymbol{x}'\omega)\mathrm{d}\boldsymbol{x}_2\mathrm{d}\boldsymbol{x}_1. \tag{2.19}$$

The scattering potential is now given by

$$\tilde{V}(\boldsymbol{x}_1,\boldsymbol{x}_2) = \chi(\boldsymbol{x}_1)\delta(\boldsymbol{x}_1 - \boldsymbol{x}_2), \tag{2.20}$$

and the ω^2 factor has been absorbed into the modified Green's function $\bar{G}^{(0)}(\boldsymbol{x}, x', \omega)$, defined as

$$\bar{G}^{(0)}(\boldsymbol{x},\boldsymbol{x}',\omega) \equiv \omega^2 G^{(0)}(\boldsymbol{x},\boldsymbol{x}',\omega). \tag{2.21}$$

It can be shown that if the inner integral with variable $\boldsymbol{x}_2$ is integrated out, then Equation 2.18 and 2.19, would be equal to Equation 2.16 and 2.17, respectively. In inverse problem solving, as will be discussed in Chapter 3, the contrast function $\chi(\boldsymbol{x})$ is considered as the unknown, because the goal is to determine some model parameters, i.e. the contrast function, from the measured seismic waveform data. Equation 2.16 is then a non-linear equation in $\chi(\boldsymbol{x}')$, since the wavefield, $\psi(\boldsymbol{x}',\omega)$, also depends on $\chi(\boldsymbol{x}')$ (Schuster, 2017). Next, the well known Born approximation, which linearises the LS equation, will be discussed.

2.4 Born approximation

The Born approximation (see for example Schuster, 2017; Eikrem et al., 2016; Jakobsen, 2012; Ikelle and Amundsen, 2005; Wang and Chew, 1989) is a linearisation of the Lippmann-Schwinger equation by only taking into account first order scattering. Here, a linear relation between the scattered wavefield and the scattering potential will be given, but first, let it be mentioned that when the term Born approximation is used, this thesis is referring to the use of a homogeneous background medium. Moreover, if the term distorted Born approximation is used, the use of a heterogeneous background medium is implied. Nevertheless, assuming that the scattered wave-field $\Delta\psi(\boldsymbol{x}, \boldsymbol{x'}, \omega)$ is sufficiently weaker than the background field $\psi^{(0)}(\boldsymbol{x}, \boldsymbol{x'}, \omega)$

$$\psi(\boldsymbol{x}, \omega) = \psi(\boldsymbol{x}, \omega) + \Delta\psi(\boldsymbol{x}, \omega) \approx \psi^{(0)}(\boldsymbol{x}, \omega). \tag{2.22}$$

The Born approximation of LS, Equation 2.16, becomes:

$$\psi(\boldsymbol{x}, \omega) = \psi^{(0)}(\boldsymbol{x}, \omega) + \omega^2 \int_{\mathcal{D}} G^{(0)}(\boldsymbol{x}, \boldsymbol{x'}, \omega)\chi(\boldsymbol{x'}, \omega)\psi^{(0)}(\boldsymbol{x'}, \omega)\mathrm{d}\boldsymbol{x'}, \tag{2.23}$$

where $\psi^{(0)}(\boldsymbol{x}, \omega)$ and $k_0(\boldsymbol{x}, \omega)$ is the wave-field and wave-number associated with the background medium, and $\chi(\boldsymbol{x}, \omega)$ is as defined in Equation 2.9.

Application of Born approximation may not always be appropriate. The Born approximation can be considered as the first two terms of the Neumann series for the LS equation. The Neumann series for the LS equation is only guaranteed to converge if (Schuster, 2017)

$$\left|\left|\omega^2 \int_{\mathcal{D}} G^{(0)}(\boldsymbol{x}, \boldsymbol{x}', \omega)\chi(\boldsymbol{x}', \omega)\mathrm{d}\boldsymbol{x}'\right|\right|_2 < 1. \tag{2.24}$$

According to Moser (2012), this means that each scattering term must be small compared to the previous term. The Born approximation becomes practical if higher order terms can be ignored. Since the Born approximation is only the first two terms of this series, the convergence criterium is given by (Moser, 2012)

$$\left|\left|\omega^2 \int_{\mathcal{D}} G^{(0)}(\boldsymbol{x}, \boldsymbol{x}', \omega)\chi(\boldsymbol{x}', \omega)\mathrm{d}\boldsymbol{x}'\right|\right|_2 \ll 1. \tag{2.25}$$

The physical interpretation is very clear in the sense that the background medium must be close to the actual medium such that the scattered field (second term of the Born series) can be considered small, compared to the background wave-field (first term of the Born series).

2.5 Discretization and matrix representation

2.5.1 Lippmann-Schwinger equation

There are numerous ways of designing acquisition geometries in exploration seismology, that are all depending on the source and receiver configuration (e.g. in marine surveys, receivers can be located near sea-surface or on the sea-bed. On land surveys, receivers can be located close to the surface or in bore-holes). Following the discretization scheme by Jakobsen and Ursin (2015), assume that N_s number of sources and N_r number of receivers have positions $\boldsymbol{x}_s$ and $\boldsymbol{x}_r$, respectively, where $s = 1, \dots, N_s$ and $r = 1, \dots, N_r$. The target domain $\mathcal{D}$, which is defined as the volume where the velocity perturbations $\chi(\boldsymbol{x})$ is non-zero, is divided into $p = 1, \dots, N$ scattering blocks with volume ΔV_p and centroids at $\boldsymbol{x}_p$. . Assuming the lowest frequency is given by $\delta\omega$, the frequencies can be divided into N_j number of frequencies, $\omega_j = j\delta\omega$, where $j = 1, \dots, N_j$. To avoid aliasing and discretization errors, N_j must be chosen high enough and ΔV_n sufficiently small, compared to the dominant wavelength of the source. The indices m and n are also introduced and can be associated either with a given receiver, or by a given scattering block. The rewritten Lippmann-Schwinger equations for the wavefield (Equation 2.18) and Green's function (Equation 2.19) can now be written as

$$\psi_n = \psi_n^{(0)} + \sum_{p=1}^{N} \sum_{q=1}^{N} \bar{G}_{np}^{(0)} V_{pq} \bar{G}_{qm} \tag{2.26}$$

and

$$\bar{G}_{mn} = \bar{G}_{mn}^{(0)} + \sum_{p=1}^{N} \sum_{q=1}^{N} \bar{G}_{mp}^{(0)} V_{pq} \bar{G}_{qn}, \tag{2.27}$$

on a discrete form, where

$$V_{pq} = \chi_p \delta_{pq} \Delta V_q. \tag{2.28}$$

In the equation above, δ is the Kronecker-delta. By definition, it gives $\delta_{pq} = 1$ if $p = q$ and $\delta_{pq} = 0$ if $p \neq q$. The discretization of the Green's functions is given by (Levinson and Markel, 2016)

$$G_{pq}^{(0)} = G^{(0)}(\boldsymbol{x}_p, \boldsymbol{x}_q), \text{ for } p \neq q, \tag{2.29}$$

and

$$\Delta V_p G_{pp}^{(0)} = \int_{\mathcal{D}_p} G^{(0)}(\boldsymbol{x}_p, \boldsymbol{x}) \mathrm{d}\boldsymbol{x}, \tag{2.30}$$

where $\mathcal{D}_p$ is the domain given by the volume of a single grid block, centred at $\boldsymbol{x}_p$.

The discretized wavefield at receiver positions (R) and in scattering volume (V) can be arranged into vectors $\boldsymbol{\Psi}_R$ and $\boldsymbol{\Psi}_V$. The vectors $\boldsymbol{\Psi}_R^{(0)}$ and $\boldsymbol{\Psi}_V^{(0)}$ are the wavefield in the background medium at receiver position and scattering volume, respectively. Equation 2.26

can now be represented by the following matrix equation (Jakobsen and Ursin, 2015)

$$\mathbf{\Psi}_R = \mathbf{\Psi}_R^{(0)} + \bar{\mathbf{G}}_{RV}^{(0)} \mathbf{V} \mathbf{\Psi}_V, \tag{2.31}$$

where

$$\mathbf{\Psi}_V = \mathbf{\Psi}_V^{(0)} + \bar{\mathbf{G}}_{VV}^{(0)} \mathbf{V} \mathbf{\Psi}_V. \tag{2.32}$$

From the definition of V_{pq} (Equation 2.28), $\boldsymbol{V}$ is an $N \times N$ diagonal matrix and contains the products $\chi_p \Delta V_q$ on the diagonal. Similarly, the discrete version of the Lippmann-Schwinger equation for the Green's function, Equation 2.27, can be written as the matrix equation

$$\bar{\mathbf{G}}_{RV} = \bar{\mathbf{G}}_{RV}^{(0)} + \bar{\mathbf{G}}_{RV}^{(0)} \mathbf{V} \bar{\mathbf{G}}_{VV}, \tag{2.33}$$

where

$$\bar{\mathbf{G}}_{VV} = \bar{\mathbf{G}}_{VV}^{(0)} + \bar{\mathbf{G}}_{VV}^{(0)} \mathbf{V} \bar{\mathbf{G}}_{VV}. \tag{2.34}$$

In the equation above, $\bar{\mathbf{G}}_{RV}$ and $\bar{\mathbf{G}}_{VV}$ are the Green's function for volume-receiver domain and volume-volume domain, respectively. Equation 2.31 - 2.34 are often called the source-independent Lippmann-Schwinger equations for wave-fields and Green's functions.

Clearly, the wavefield in the background medium depends on the source distribution. In the case where multiple sources are used, a vector $\tilde{\boldsymbol{f}}_s$ is introduced. This is an N_s dimensional vector, containing all the information about the source distribution. The wavefield in the background medium can be expressed using a source-dependent Green's function (to be defined), as

$$\mathbf{\Psi}_R^{(0)} = \mathbf{G}_{RS}^{(0)} \tilde{\mathbf{f}}_s, \tag{2.35}$$

for the receiver surface, and

$$\mathbf{\Psi}_V^{(0)} = \mathbf{G}_{VS}^{(0)} \tilde{\mathbf{f}}_s, \tag{2.36}$$

for the scattering domain. Equivalently, the wavefields in the actual medium are given by

$$\mathbf{\Psi}_R = \mathbf{G}_{RS} \tilde{\mathbf{f}}_s \tag{2.37}$$

and

$$\mathbf{\Psi}_V = \mathbf{G}_{VS} \tilde{\mathbf{f}}_s. \tag{2.38}$$

The corresponding source-dependent Green's functions in Equation 2.35 - 2.38, are given by (Jakobsen and Ursin, 2015)

$$\mathbf{G}_{RS} = \mathbf{G}^{(0)}_{RS} + \bar{\mathbf{G}}^{(0)}_{RV}\mathbf{V}\mathbf{G}_{VS} \tag{2.39}$$

and

$$\mathbf{G}_{VS} = \mathbf{G}^{(0)}_{VS} + \bar{\mathbf{G}}^{(0)}_{VV}\mathbf{V}\mathbf{G}_{VS}. \tag{2.40}$$

Equation 2.37 and 2.38 gives the total wave-field in the receiver and scatter domain, respectively. The Green's function, $\mathbf{G}_{VS}$, in equation 2.40 can be calculated as following, using direct matrix inversion

$$\mathbf{G}_{VS} = (\mathbf{I} - \bar{\mathbf{G}}^{(0)}_{VV}\mathbf{V})^{-1}\mathbf{G}^{(0)}_{VS}. \tag{2.41}$$

For the calculation of the scattered wave-field data using multiple sources and frequencies, forward modelling can be implemented by discretizing the frequencies. From now on, the scattered wavefield, given by $\Delta\mathbf{\Psi}$, will be recognized as the vector $\mathbf{d}$ (due to the fact that in later experiments, the scattered wave-field will be considered as the data). From Equation 2.10 the scattered wavefield can be written as

$$\mathbf{d} \equiv \mathbf{\Psi}_R - \mathbf{\Psi}^{(0)}_R, \tag{2.42}$$

Now, substituting $\mathbf{\Psi}^{(0)}_R$ and $\mathbf{\Psi}_R$ using Equation 2.35 and 2.37, in conjunction with Equation 2.39, the scatteded wavefield (Equation 2.42) can be rewritten as

$$\mathbf{d} = \left[\mathbf{G}_{RS} - \mathbf{G}^{(0)}_{RS}\right]\tilde{\mathbf{f}} = \bar{\mathbf{G}}^{(0)}_{RV}\mathbf{V}\mathbf{G}_{VS}\tilde{\mathbf{f}}_s. \tag{2.43}$$

The Green's function, $\boldsymbol{G}_{VS}$, for the propagation between the source to scatter domain, can be calculated using Equation 2.41 (or alternatively using the T-matrix, which will be presented in Section 2.6). For the discretization of the frequencies, one can assume that N_j number of discrete frequency components are given by $\omega_j = j\delta\omega$, where $\delta\omega$ is the lowest frequency and $j = 1, \ldots, N_j$. Equation 2.43 can then be organized into its component form, as

$$d^{(sj)}_r = \sum_{n=1}^{N} J^{(sj)}_{rn}\chi_n, \tag{2.44}$$

where

$$J^{sj}_{rn} \equiv \bar{G}^{(0)}_{rn}(\omega_j)\Delta V_n G_{ns}(\omega_j)\tilde{f}_s(\omega_j). \tag{2.45}$$

In the equation above, the model parameter χ_n are the elements of a vector, $\boldsymbol{\chi}$, containing all of the N elements of χ, given in Equation 2.9. Next, the indices r, s and j are replaced by a single index, α, used for combination counting, such that (Jakobsen and Ursin, 2015)

$$r, s, j \rightarrow \alpha = 1, \dots, N_d = N_r N_s N_j.$$

Equation 2.44 can now be written as

$$d_\alpha = \sum_{n=1}^{N} J_{\alpha n} \chi_n, \tag{2.46}$$

or in matrix notation

$$\mathbf{d} = \mathbf{J}(\chi)\boldsymbol{\chi}, \tag{2.47}$$

The matrix $\mathbf{J}(\chi)$ gives the non-linear relation between the seismic data and the contrast function, due to the fact that the the matrix $\mathbf{J}$ is itself depending on the contrast function. Furthermore, it can be used for the forward simulation of scattered wave-fields for multiple sources, receivers and frequencies. The vector $\boldsymbol{\chi}$ can be recognized as the vector containing the model parameters on the form of general inverse problems, and will be discussed in more details in Chapter 3. Note that there is a nonlinear relation between the scattered wavefield, and the model parameters, and a linearised solution for this inverse problem will be discussed in Chapter 4.2.

2.5.2 Born approximation

As mentioned in Section 2.4, the scattered wavefield, d, can be approximated by assuming single scattering. From Equation 2.43, substitute $\mathbf{G}_{VS}$ with $\mathbf{G}_{VS}^{(0)}$. The Born approximated scattered wavefield can then be written as (Eikrem et al., 2016)

$$d_r^{(sj)} = \sum_{n=1}^{N} J_{rn}^{(sj)} \chi_n, \tag{2.48}$$

where χ_n is the discretization of the contrast function defined in Equation 2.9 and $L_{rn}^{(sj)}$ is given by

$$J_{rn}^{(sj)} \equiv \bar{G}_{rn}^{(0)}(\omega_j) \Delta V_n G_{ns}^{(0)}(\omega_j) \tilde{f}(\omega)_s. \tag{2.49}$$

The next step is to rewrite Equation 2.48 into a matrix equation which is more suitable for inversion. The three indices r, s and j in Equation 2.48 are now replaced by a singel index α, as

$$r, s, j \to \alpha = 1, \ldots, N_d = N_r N_s N_j. \tag{2.50}$$

The discrete Equation 2.48, can now be re-written as the following sum

$$d_\alpha = \sum_{n=1}^{N} J_{\alpha n} \chi_n, \tag{2.51}$$

or in matrix notation

$$\mathbf{d} = \mathbf{J}\boldsymbol{\chi}. \tag{2.52}$$

In the Born approximation, the model operator, **J**, gives a linear relation between the model parameters and data. The concepts of forward and inverse problems will be discussed further in Chapter 3.

2.6 The T-matrix method

The T-matrix (or the transition operator) was developed in quantum mechanical potential scattering theory. For nonlinear inverse scattering problems, updates of the wave-fields, and hence Green's functions, at every iteration step, are necessary. The T-matrix has proven to be quite useful in speeding up the iterative inversion processes (Jakobsen and Ursin, 2015). The T-matrix can also be used for domain decomposition, which can be used to accelerate the T-matrix approach (Jakobsen and Wu, 2018) and in the inverse time-lapse seismic waveform problem in the reconstruction of more than one reservoir. Following the derivation of the T-matrix in Jakobsen (2012), the T-matrix is defined as

$$\mathbf{V}\mathbf{G}_{VV} = \mathbf{T}\mathbf{G}_{VV}^{(0)}. \tag{2.53}$$

Next, the Lippmann-Schwinger equation for the Green's function (Equation 2.34) is multiplied with the scattering potential **V**, giving

$$\mathbf{V}\mathbf{G}_{VV} = \mathbf{V}\mathbf{G}_{VV}^{(0)} + \mathbf{V}\mathbf{G}_{VV}^{(0)}\mathbf{V}\mathbf{G}_{VV}. \tag{2.54}$$

Substitute $\mathbf{VG}_{VV}$ in Equation 2.54 using the relation in Equation 2.53

$$\mathbf{TG}_{VV}^{(0)} = \mathbf{VG}_{VV}^{(0)} + \mathbf{VG}_{VV}^{(0)}\mathbf{TG}_{VV}^{(0)}. \tag{2.55}$$

Since the Green's function, $\mathbf{G}_{VV}^{(0)}$, is arbitrary, the above equation can be reduced to the Lippmann-Schwinger equation for the T-matrix (see e.g. Jakobsen, 2012; Jakobsen and Ursin, 2015; Eikrem et al., 2017)

$$\mathbf{T} = \mathbf{V} + \mathbf{VG}_{VV}^{(0)}\mathbf{T}, \tag{2.56}$$

or

$$\mathbf{T} = (\mathbf{I} - \mathbf{VG}_{VV}^{(0)})^{-1}\mathbf{V}. \tag{2.57}$$

The T-matrix (2.57) offers a full numerical solution, including all the effects of multiple scattering in the Born-Neumann series (Jakobsen, 2012). This solution is convenient if the model size is not too large. Computational cost and convergence problems using the T-matrix can be dealt with using domain decomposition and renormalization methods (see Jakobsen and Wu, 2018, 2016). Using the T-matrix defined above, it is possible to calculate the Green's function for any inhomogeneous medium using the Lippmann-Schwinger equation for Green's functions in conjunction with the definition of the T-matrix (Equation 2.53):

$$\mathbf{G}_{VV} = \mathbf{G}_{VV}^{(0)} + \mathbf{G}_{VV}^{(0)}\mathbf{VG}_{VV} = \mathbf{G}_{VV}^{(0)} + \mathbf{G}_{VV}^{(0)}\mathbf{TG}_{VV}^{(0)}. \tag{2.58}$$

Consequently, the full integral equation T-matrix method can be used to calculate the scattered wavefield in any inhomogeneous model using (Jakobsen, 2012)

$$\mathbf{\Psi}_R = \mathbf{\Psi}_R^{(0)} + \mathbf{G}_{RV}^{(0)}\mathbf{T}\mathbf{\Psi}_R^{(0)}. \tag{2.59}$$

2.7 Numerical results

Two methods for numerical calculation of seismic data have been presented in this chapter: (1) *Born approximation* which linearises the LS equation by assuming only single scattering; (2) *full integral equation T-matrix method* which includes all the effects of multiple scattering in the Born-Neumann series (Jakobsen, 2012). In this numerical experiment, calculation of synthetic waveform data will be performed, demonstrating the process of seismic forward modelling using both methods mentioned above. The reservoir model is a two-dimensional P-wave velocity model, and contains a dipping layer and a structure which is supposed to resemble a petroleum anticline trap at approximately 650 m depth. The reservoir model has of a total number of 3772 elements, with grid size 82×46 in x and z direction, respectively. The total length is 1640 m in the horizontal direction and 920 m in the vertical direction. The velocity in the model varies from 2000 m/s near the surface and increases up 2400 m/s in the lowermost layer. This model is from now on referred to as the baseline model (see Figure 2.3a). To be able to mimic a time-lapse effect, for instance caused by some production-related change in the reservoir, a velocity perturbation of 300 m/s is added to the velocities in the baseline reservoir. The modified model, which is equal to the baseline model except for a velocity perturbation in the reservoir, is from now on referred to as the monitor model (see Figure 2.3b). The time-lapse velocities (see Figure 2.3c) are considered to be relatively large in a production based viewpoint, but the contrast is considered small enough to be evaluated by the Born approximation (see Section 2.4). A homogeneous background medium of 2000 m/s was used for two applications: (1) the homogeneous background medium is used in the Born approximation to approximate the scattered wave-field from the reservoir model; (2) an arbitrary homogeneous medium is needed to calculate the Green's function for the actual reservoir model, using the LS equation for Green's functions (i.e. Equation 2.58), to be used in the exact integral method.

The following seismic survey was used for both the baseline and monitor. 82 receivers with 20 m equidistant spacing was placed on the surface, and a single source was placed in the middle of the model at the surface (known in literature as common shot gather). A sampling time of 0.01 s and a total recording time of 3 s was used. A Ricker wavelet has been used as source and can be seen in time domain in Figure (2.2a). Furthermore, since the Nyquist frequency was 50 Hz, a low dominant frequency of 7.5 Hz was chosen for the source to ensure that most of the energy would be sampled correctly. In Figure 2.2b, it can be seen that there is practically low energy in frequencies higher than 20 Hz.

The synthetic seismic data were first generated for the baseline model. The baseline data calculated using the Born approximation can be seen in Figure 2.4a and 2.7a. In this thesis, the seismic data has been shown in time-domain. It could also have been visualized in frequency domain (Jakobsen and Ursin, 2015). The synthetic data were also calculated

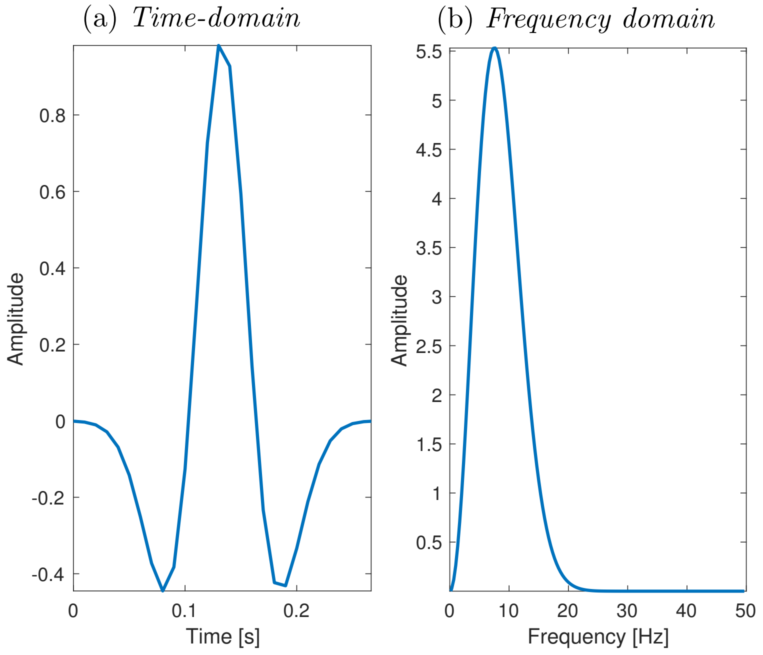
(a) *Time-domain* (b) *Frequency domain*

Figure 2.2: *Ricker wavelet withf centre frequency of 7.5 Hz in (2.2a) time domain and (2.2b) frequency domain.*

using the full integral T-matrix method and can be seen in Figure 2.4b and 2.7b.

Furthermore, since the main focus of this thesis is in the application of seismic data to time-lapse analyses, a repeat survey was performed and synthetic data were generated for the monitor model. The results from the Born approximation can be seen in Figure 2.5a and 2.8a, while the results from the full integral T-matrix method can be seen in Figure 2.5b and 2.8b. The time-lapse data were then obtained by subtracting the baseline data from the monitor data, calculated using the same method. Thus, there were two sets of time-lapse data. One containing the difference of the Born approximated data (see Figure 2.6a and 2.9a), and the other with full integral equation T-matrix methods (see Figure 2.6b and 2.9b).

2.8 Discussion

The numerical experiment performed in the previous section, was intended to demonstrate the Born approximation. Also, another reason was to visualize the seismic data that are of great importance in the Geosciences, including time-lapse seismic studies. It is also important to be aware of the weaknesses that may follow the employment of the Born approximation.

By comparing Figure 2.4a and 2.4b, the first thing to notice is that the Born approximated seismogram appears more clean, while the seismogram calculated by the T-matrix tend to look more chaotic. This can be explained by the fact that the Born approximation only takes into account single order scattering. In other words, internal multiples and diffracted waves will not be modelled by the Born approximation. Hence, the synthetic seismogram generated by the Born approximation, will tend to look more clean.

In Figure 2.6a and 2.6b, the time-lapse seismic data are visualized using Born approximation and the exact integral T-matrix equation, respectively. As previously mentioned, these seismograms are made by subtracting the baseline data from the monitor data. Thus, the wiggles that can be seen in the time-lapse seismograms, represent the scattered wave-field from the time-lapse effect, i.e. the reflected data from the reservoir. Figure 2.6 does clearly demonstrate the lack of data, for instance multiples, in the Born approximation. In full waveform inversion (to be presented in Chapter 4.2), also the information in these waves will be used.

In Figure 2.9a and 2.9b, yet another weakness of the Born approximation is revealed. In the former figure, it can be observed that the first wave arrives at the receiver after approximately 0.7 seconds. In the latter figure, calculated using full integral equation T-matrix, the same wave arrives only after 0.5 seconds. This is due to the fact that the wave-field in the Born approximation is travelling through a background medium with the constant velocity of 2000 m/s. However, in Figure 2.9b the waves were travelling in the inhomogeneous monitor model (see Figure 2.3b) with velocities higher than 2000 m/s. Thus, the waves generated using the T-matrix method have travelled to the receiver in a shorter amount of time. Jakobsen and Ursin (2015) have demonstrated that the full integral equation T-matrix method gives results that are very close to the ones obtained by finite difference method. Assuming that the medium intended to be modelled is inhomogeneous, the use of a heterogeneous background medium close to (or equal to) the actual medium, will provide a more accurate generation of data. Since the wave-field travels through the background medium, travel-times will be affected by the choice of background medium. The Born approximation also result in a slightly different amplitude, compared to the full integral equation T-matrix method. This can be seen both the baseline, monitor and time-lapse seismic data by comparing the two methods in Figure 2.7, 2.8 and 2.9.

These weaknesses with the Born approximation is very important to be aware of, because the data that is generated may not be very accurate. However, the late arrival problem of the Born approximation can be reduced (or completely eliminated) by choosing an appropriate background medium that may be close to (or equal to) the actual medium that the seismic data is supposed to travel through. The use of the Born approximation, in combination to a heterogeneous background model, is hence forth referred to as the distorted Born approximation.

(a) *Baseline model*

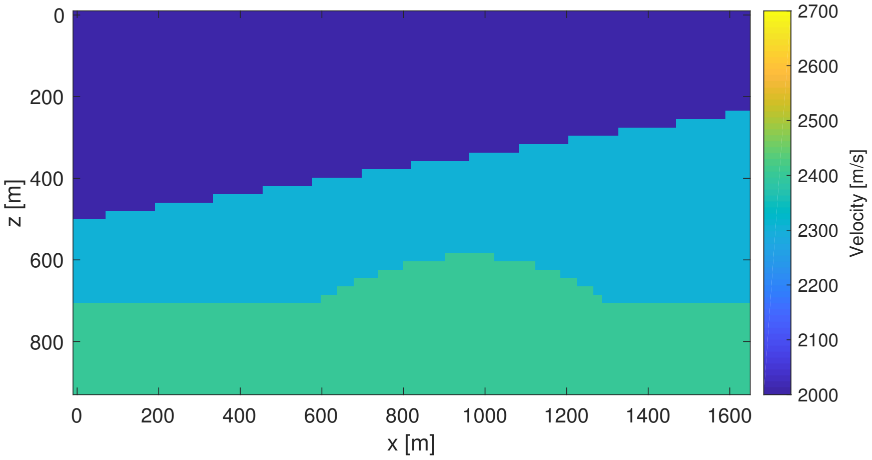

(b) *Monitor model*

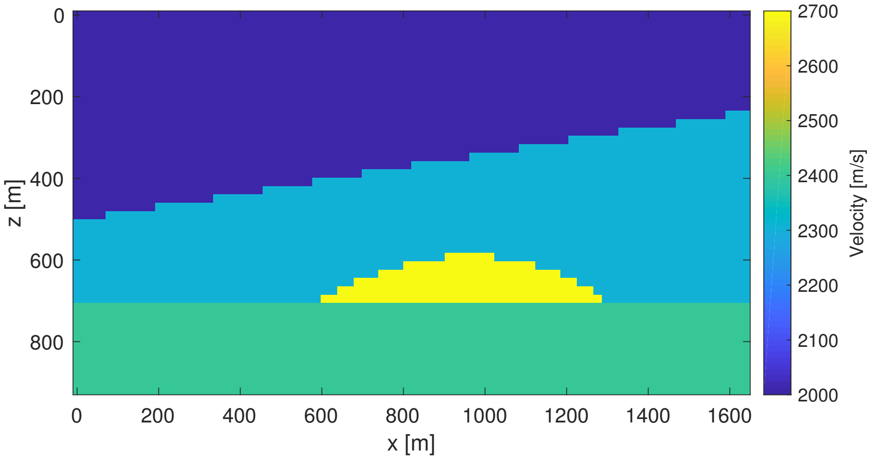

(c) *Time-lapse model*

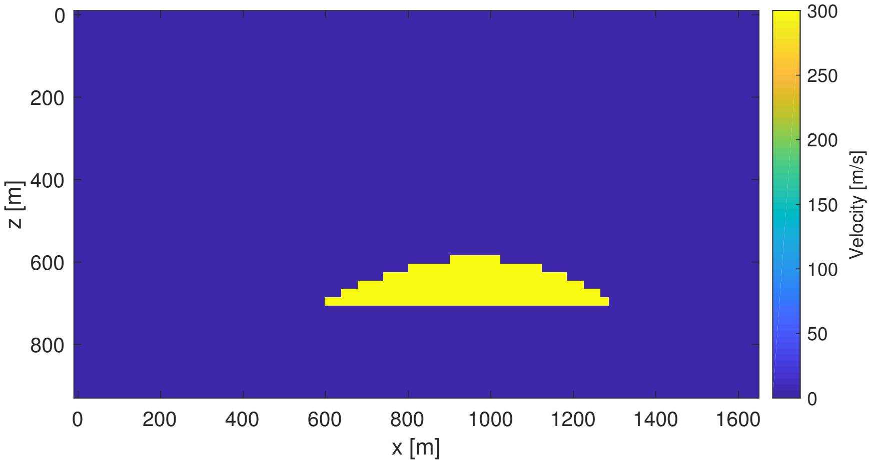

Figure 2.3: *2D reservoir model of P-wave velocities in a time-lapse perspective. Figure 2.3a shows the baseline model, middle Figure 2.3b shows the monitor model, where some change in the reservoir has occured with the consequence of an increase of 300 m/s in P-wave velocity. Figure 2.3c shows the time-lapse difference between the monitor and baseline model.*

(a) *Born approximation*

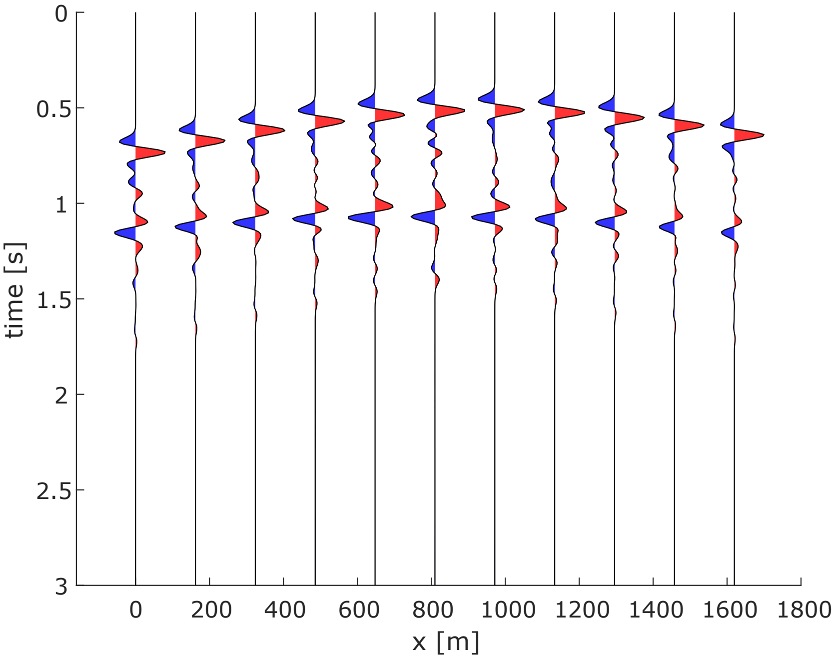

(b) *T-matrix*

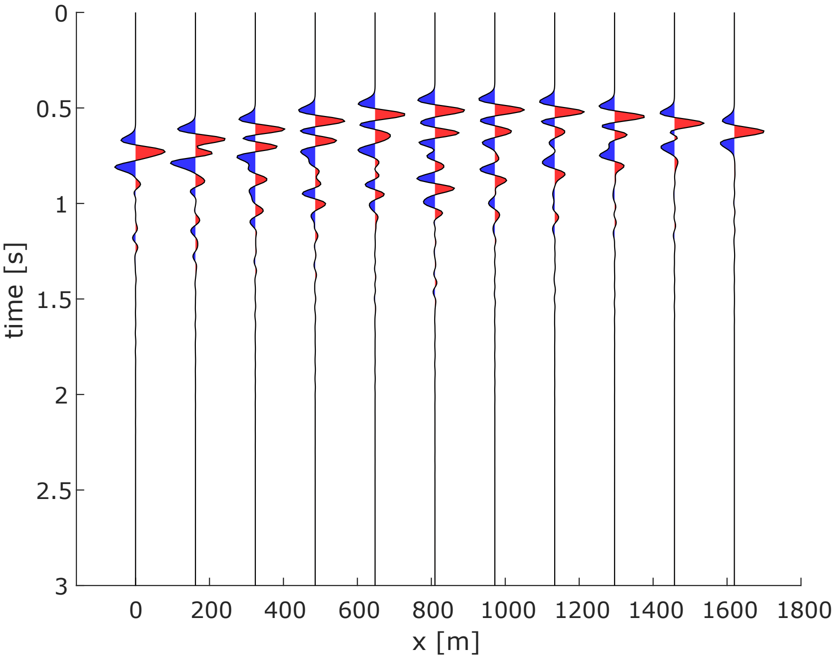

Figure 2.4: *Plot of selected traces, generated in the baseline model (Figure 2.3a) using Born approximation (2.4a) and the exact integral equation T-matrix method (2.4b).*

(a) *Born approximation*

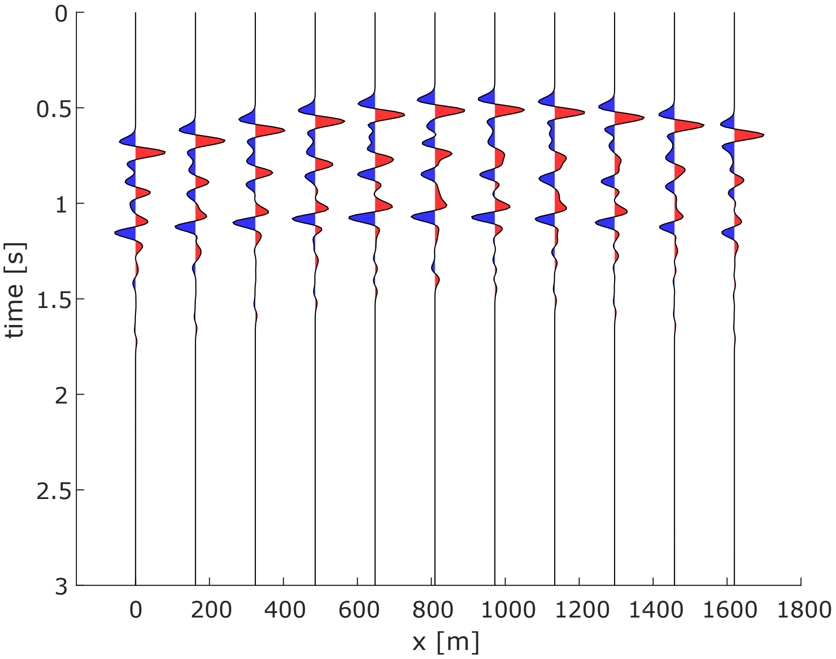

(b) *T-matrix*

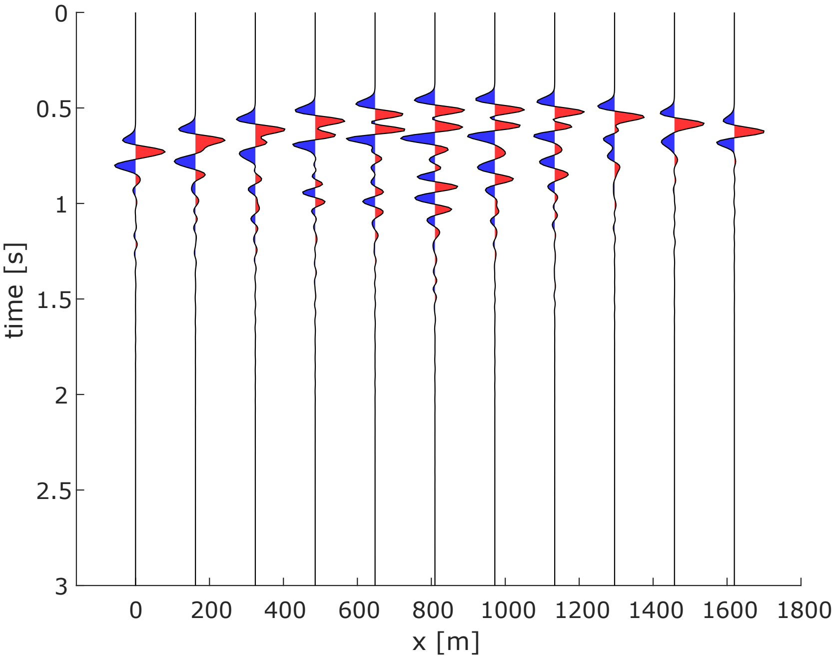

Figure 2.5: *Plot of selected traces, generated in the monitor model (Figure 2.3b) using Born approximation (2.5a) and the exact integral equation T-matrix method (2.5b).*

(a) *Born approximation*

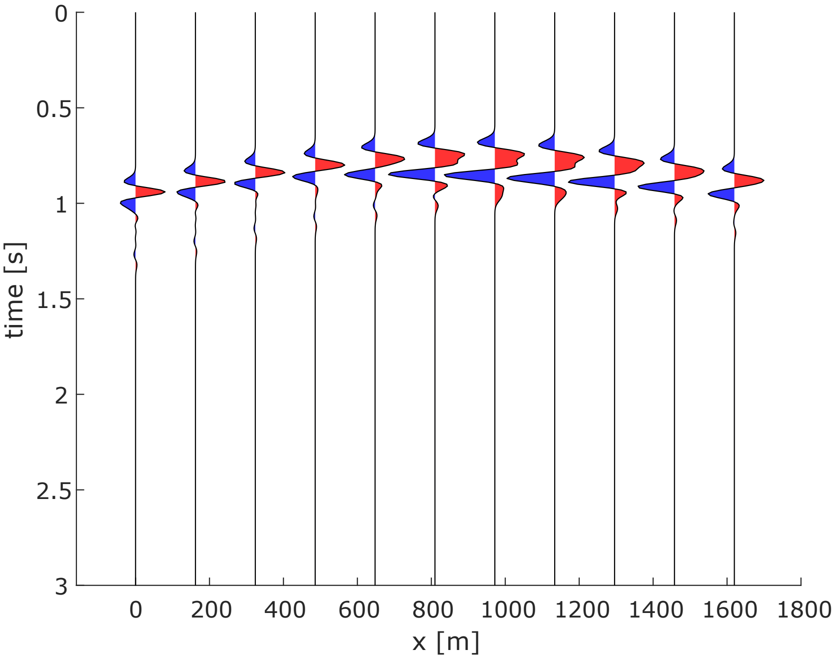

(b) *T-matrix*

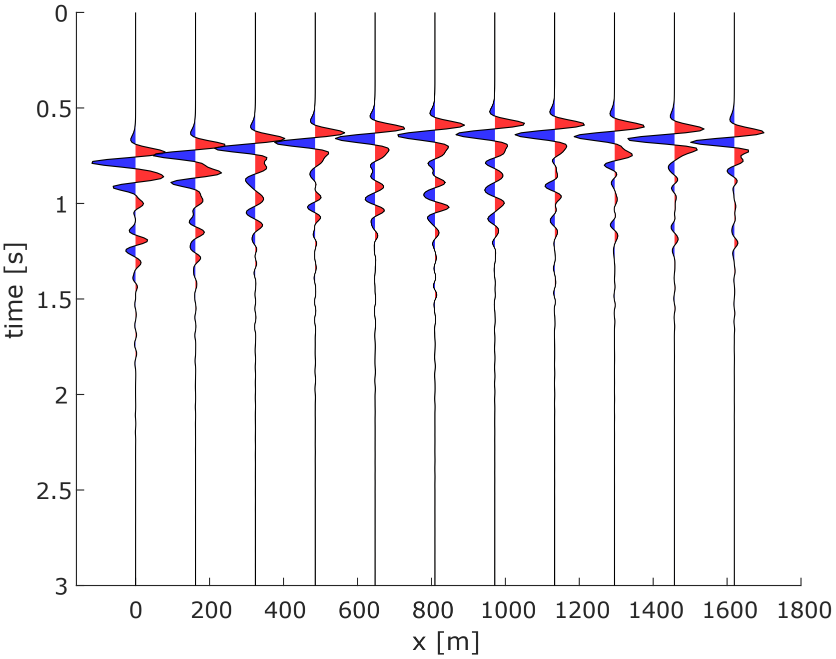

Figure 2.6: *Plot of selected traces, generated in the time-lapse model (Figure 2.3c) using Born approximation (2.6a) and the exact integral equation T-matrix method (2.6b).*

(a) *Born approximation*

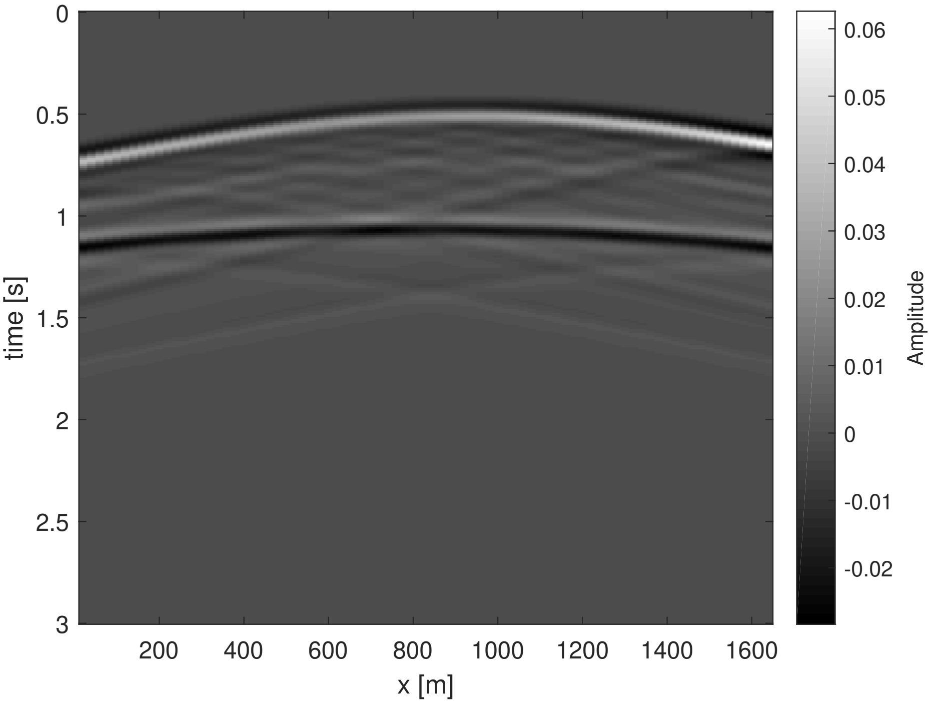

(b) *T-matrix*

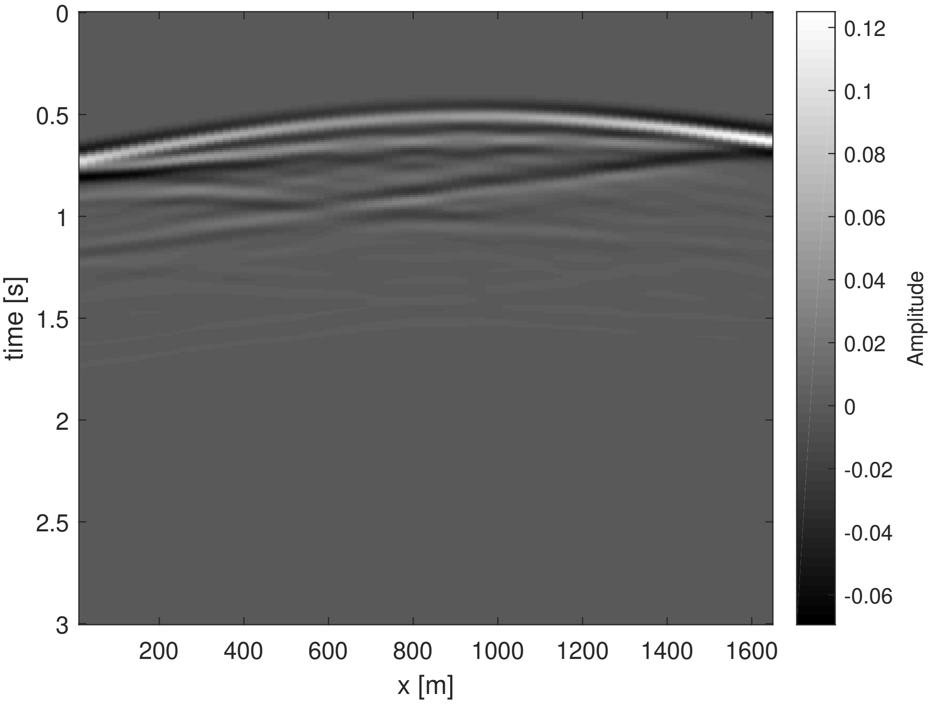

Figure 2.7: *Synthetic data generated of the baseline model (Figure 2.3a) using Born approximation (2.7a) and the exact integral equation T-matrix method (2.7b).*

(a) *Born approximation*

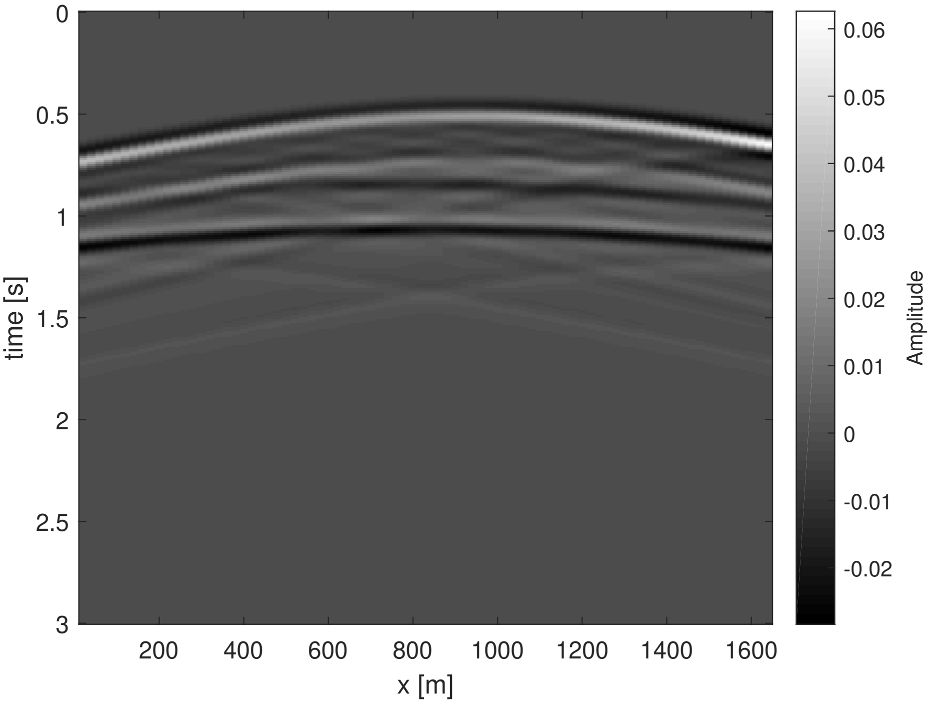

(b) *T-matrix*

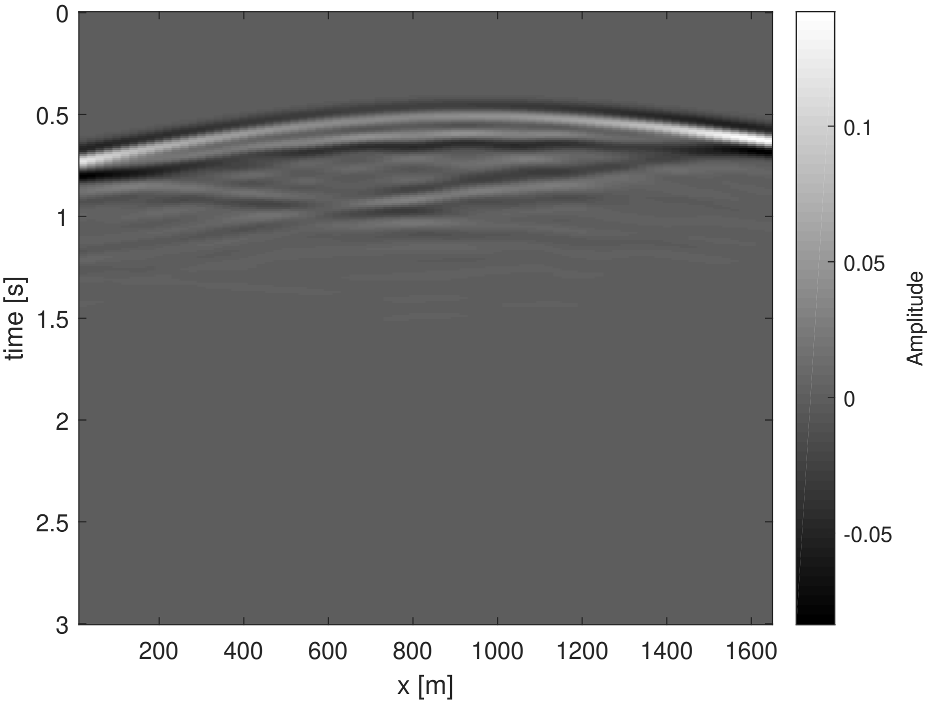

Figure 2.8: *Synthetic data generated of the monitor model (Figure 2.3b) using Born approximation (2.8a) and the exact integral equation T-matrix method (2.8b).*

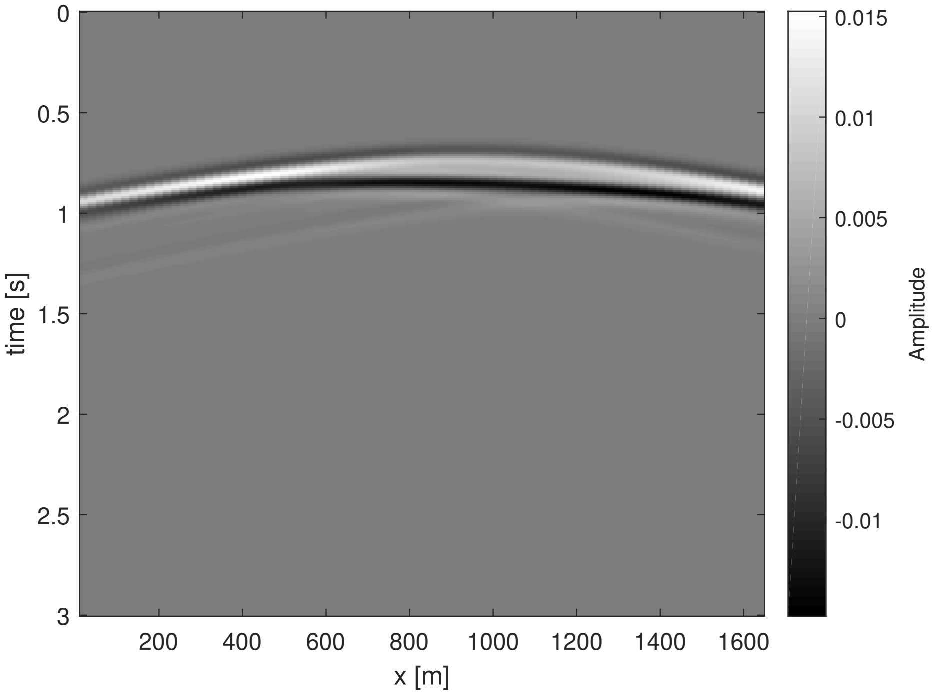
(a) *Born approximation*

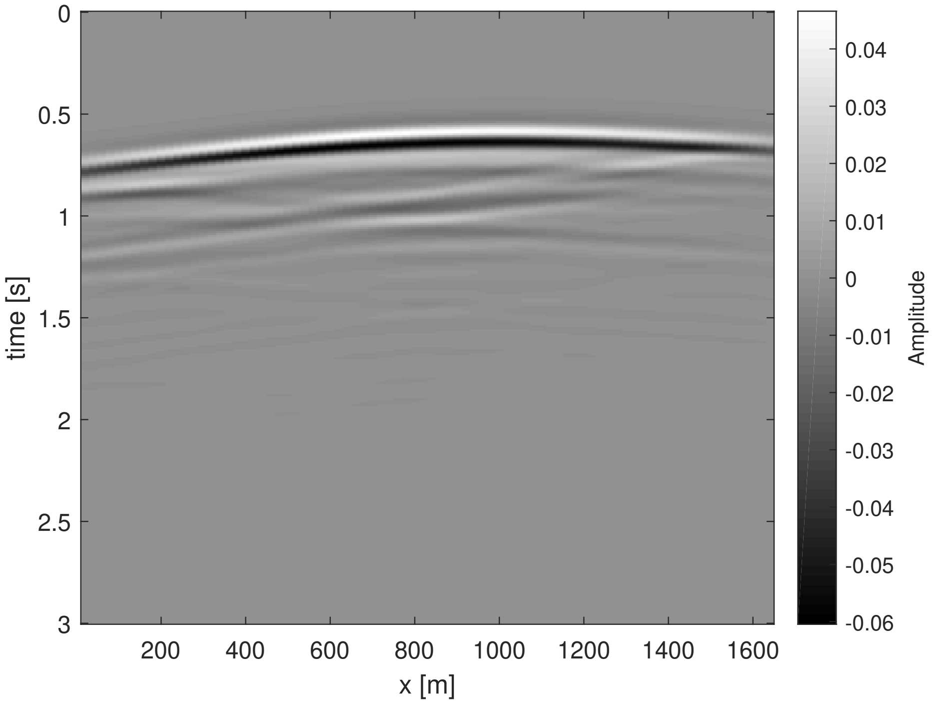
(b) *T-matrix*

Figure 2.9: *Synthetic data generated of the time-lapse model (Figure 2.3c) using Born approximation (2.9a) and the exact integral equation T-matrix method (2.9b).*

Chapter 3

Theory of linear inverse problems

> *For now we see through a glass, darkly, but then ...*
>
> Paul of Tarsus

Problem solving in physical sciences normally involves using well-established theories to make predictions of observable measurements for given values of some model parameters. For instance, in the previous chapter on forward modelling, the acoustic wavefield was calculated based on the knowledge of the P-wave velocity in the survey domain. This chapter will present the general concepts on how the inverse of that problem can be solved, i.e. how to estimate the P-wave velocity based on the measured acoustic wave-field. Non-linear inverse problems can in some cases be linearised by reducing it to a series of linear inverse problems. It could then be solved iteratively, by applying linear inverse methods at each iteration step. For that reason, this chapter will focus on solving a linear inverse problem.

This chapter is split into two parts. The first covers fundamentals of inverse theory and discusses the concepts of ill- and well-posed problems. Then there will be a description of the general deterministic least squares method, which will be demonstrated with an experiment of fitting a straight line to data points. In the end there will be a description of the Bayesian approach where it is shown how an inverse problem can be solved in a probabilistic manner.

3.1 General considerations

The process of solving an inverse problem would in general include three main steps: (1) *Model parameter estimation*, which involves finding an optimal set of parameters to characterize the model; (2) *Forward modelling*, allowing for the prediction of data; (3) *Inverse problem*, where the inversion is done to estimate model parameters based on the observed data (Ikelle and Amundsen, 2005). Usually, there exist some theory that describes the relationship between data and model parameters that can be written on the form (Schuster, 2017)

$$\mathbf{d} = \mathbf{J}(\mathbf{m}) \tag{3.1}$$

In Equation 3.1, $\mathbf{J}$ is the forward operator, describing the linear, or nonlinear, relationship between the data and model parameters. In the linear case, the problem is often written as

$$\mathbf{d} = \mathbf{J}\mathbf{m}. \tag{3.2}$$

and inverse problem can then be formulated as

$$\mathbf{m} = \mathbf{J}^{-1}\mathbf{d}, \tag{3.3}$$

where $\mathbf{J}^{-1}$ is the inverse of the operator $\mathbf{J}$. There exists several techniques for approximating continuous and numerical inverse problems (see for example Tarantola (2005); Menke (2012); Aster et al. (2013)). In this thesis, the focus is on the numerical calculation of model parameters and therefore the following inverse theory is described in a discrete sense. The data often come as a list of numerical values by nature, because they in most cases are individual measurements varying in time and space. Thus, they are accordingly represented by a vector $\mathbf{d}$, containing $[d_1, d_2, \ldots, d_N]^T$ with N number of data measurements. Here the upper-case letter T signifies the transpose of vector $\mathbf{d}$. For numerical calculation of the model parameters, they are in a simular way described by vector $\mathbf{m} = [m_1, m_2, \ldots, m_M]^T$, with M number of individual parameters. Then it follows that $\mathbf{J}$ is given by a $N \times M$ matrix.

It should be obvious that the existence of $\mathbf{J}^{-1}$ is not guaranteed. This is rarely the case because there would have to be exactly enough (noise less) data to determine each model parameter uniquely. Hadamard (1902) categorized inverse problems into ill- and well-posed. An inverse problem is defined as well-posed if: (1) *A solution exists*; (2) *The solution is unique*, i.e. there exists only one solution to the inverse problem; (3) *The solution is stable*, i.e. it would depend continuously on the data and not change drastically with small amounts of change in the data measurements. A problem is defined as ill-posed if one or more of the criteria above is not satisfied. Consequently, there exists different kind of ill-posed problems.

Menke (2012) divides ill-posed inverse problems into under-determined, over-determined, and mixed-determined. An inverse problem is said to be under-determined if Equation 3.1 does not contain enough information to solve each model parameter uniquely (for example the case when there are more model parameters to be determined, than available data measurements). On the other hand, if Equation 3.1 contains too much information to give a unique solution of the model parameters, it is called an over-determined problem. This can be illustrated by an inconsistent set of equations, $x = 1$ and $x = 2$. Because of noisy data measurements, it will be impossible to find a unique solution. If the inverse problem is neither completely under-determined nor over-determined, it is spoken of as a mixed-determined problem. This occurs when the data measurements contains more than enough information to satisfy some model parameters in an over-determined way, but lack information for solving the rest. The most encountered kind of inverse problem in geophysics are the mixed-determined types. The problem lies in the nature of many geophysical problems, where the interest is in finding physical properties beneath the Earth's surface, but the data measurements are often made on the surface of the Earth. The data could then have more than enough information to solve some model parameters (e.g. close to the surface), but not the whole model (e.g. deep within complex structures). Following, there will be given methods that will be essential for dealing with the ill-posed inverse problems that will be presented in this thesis.

3.2 Deterministic approach

3.2.1 Least squares solution to the linear inverse problem

In the deterministic approach, only the one solution that best fits the data is sought. According to Menke (2012), the simplest method to solve an inverse problem on the form Equation 3.2, is based on the length of both the estimated model parameters $\mathbf{m}^{est}$, and the predicted data using forward modelling with estimated model parameters $\mathbf{Jm^{est}}$. For a linear over-determined problem, there is inconsistent measurements because of noisy data. To find the solution that best fits the data, one can minimize the squared L_2 norm of the data residual, defined as the difference between the observed and the predicted data (Schuster, 2017). The total error is then defined as following

$$E = ||\mathbf{d}^{obs} - \mathbf{J}\mathbf{m}^{est}||_2^2. \tag{3.4}$$

To minimize the total error, Equation 3.4 is differentiated with respect to $\mathbf{m}$ and set equal to zero (see Menke (2012) for full derivation). The least squares solution of an over-determined problem can then be written as

$$\mathbf{m}^{est} = [\mathbf{J}^T\mathbf{J}]^{-1}\mathbf{J}^T\mathbf{d}^{obs}. \tag{3.5}$$

Below, there will be an example of how to implement Equation 3.5 to an overdetermined inverse problem.

3.2.2 The least squares problem for a straight line

The principles of inversion theory may be somewhat difficult to grasp at the first glanse. One of the best ways of explaining the basic principles behind this very counterintuitive theory, is by giving a simple example. Say one want to fit a straight line to N number of individual data points, given by $[x_i, d_i]$, where $i = 1, 2, \ldots, N$. The equation for a straight line is given by $d = ax + b$. The problem can then be written to the form of Equation 3.2 as

$$\begin{bmatrix} d_1 \\ d_2 \\ \vdots \\ d_i \end{bmatrix} = \begin{bmatrix} x_1 & 1 \\ x_2 & 1 \\ \vdots & \vdots \\ x_i & 1 \end{bmatrix} \begin{bmatrix} a \\ b \end{bmatrix}, \tag{3.6}$$

where a and b are the model parameters, describing a straight line, that is sought. If the number of data points equals two, then the inverse problem is well-posed and it is possible to invert the matrix $\mathbf{J}$ to find the model parameters that describes the straight line passing through both data points. If there are more than two data points, the problem is of ill-posed, overdetermined kind. It is impossible to fit a straight line that passes through all, except in the case when the points actually lie on a straight line. To simulate data measurements, $N = 10$ different data points were created by the linear equation $y = ax + b$, with $a = 1$ and $b = 0$. A random noise vector $\boldsymbol{\eta}$, containing elements with values ranging from -1 to 1, was created from a uniform distribution and added to the straight line points y_i s.t. the data was given by $d_i = y_i + \eta_i$. The least squares method was then used, and Equation 3.5 was solved for the model parameters. In this example, 10 data points were used to estimate 2 model parameters. This is clearly an over-determined problem, and in Figure 3.1, it can be

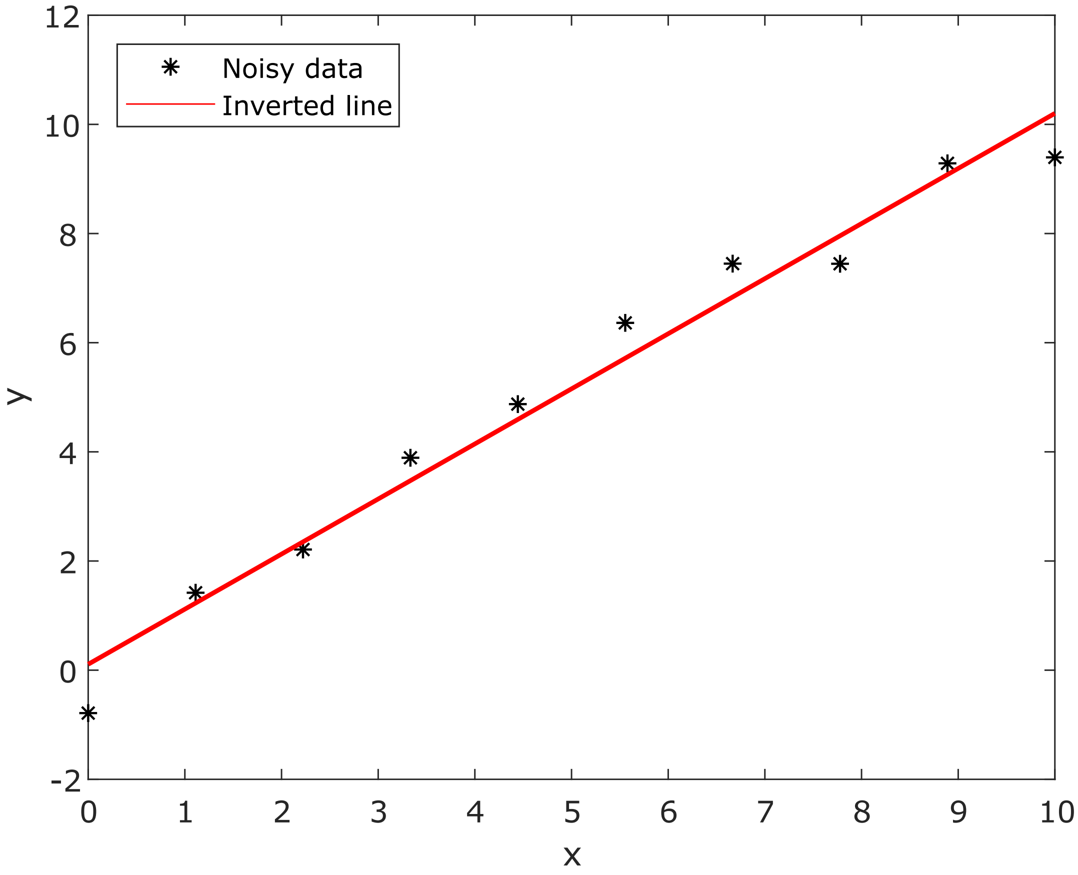

Figure 3.1: *Inverted straight line from $N = 10$ individual data points, using the least squares solution of the minumum L_2 norm.*

observed that it is impossible for the straight line to pass through all data points. Instead, a and b were chosen based on the minimum total error, i.e. the L_2 norm of the data residual, as defined in Equation 3.4.

3.2.3 Tikhonov regularization

Inverse geophysical problems are often mixed-determined. To dampen the ill-posedness of a linear mixed-determined problem, a method called Tikhonov regularization may be utilized. In the general Tikhonov regularization method, the goal is to minimize an objective function $E(\mathbf{m}^{est})$, given by (Aster et al., 2013)

$$E(\mathbf{m}^{est}) = \left|\left|\mathbf{d}^{obs} - \mathbf{J}\mathbf{m}^{est}\right|\right|_2^2 + \lambda^2 \left|\left|\mathbf{F}\mathbf{m}^{est}\right|\right|_2^2 . \tag{3.7}$$

The first term in Equation 3.7 is the squared L_2 norm of the data residual and the second term is a regularization parameter λ multiplied with the squared L_2 norm of the penalty term $\mathbf{F}\mathbf{m}^{est}$. The choice of this term depends on what kind of solution is wanted. If one chooses the penalty term equal to the identity matrix, $\mathbf{F}\mathbf{m}^{est} = \mathbf{m}^{est}$, minimization of the penalty term constrains the solution of the model parameters to its minimum L_2 length. An expression for $\mathbf{m}^{est}$ can then be written as

$$\mathbf{m}^{est} = [\mathbf{J}^T\mathbf{J} + \lambda^2\mathbf{I}]^{-1}\mathbf{J}^T\mathbf{d}. \tag{3.8}$$

Equation 3.8 is often referred to as the damped least squares solution of the inverse problem (see Menke, 2012; Aster et al., 2013), and solves the linear ill-posed inverse problem for the model parameters of minimum length (minimum squared L_2 norm). There are several ways of determining the regularization parameter λ. Farquharson and Oldenburg (2004) have compared automatic techniques for estimating the regularization parameter. One popular method is to use the L-curve method (see e.g. Hansen, 1997). Alternatively, one can employ the discrepancy principle (Constable et al., 1987), which uses the calculated misfit between measured and estimated data.

3.3 Bayesian inversion

In the previous section, a classic inversion technique was demonstrated. This section is going to present an alternative methodology where the solution is not only given by the single best fit, but instead a random variable giving the probability distribution of the model parameters. This solution is often referred to as the posterior distribution and can be written as the conditional probability of the model parameters, given the data, $q(\mathbf{m}|\mathbf{d})$. The data is the conditional probability, $f(\mathbf{d}|\mathbf{m})$. The prior distribution of the model parameters is given by $p(\mathbf{m})$, and describes the probability of $\mathbf{m}$. These three distributions can be combined using Bayes' theorem

$$q(\mathbf{m}|\mathbf{d}) = \frac{f(\mathbf{d}|\mathbf{m})p(\mathbf{m})}{c}, \tag{3.9}$$

where c is the integral over all models $\mathcal{M}$, given by

$$c = \int_{\mathcal{M}} f(\mathbf{d}|\mathbf{m})p(\mathbf{m})\mathrm{d}\mathbf{m}. \tag{3.10}$$

Note that it is not necessary to solve the integral in Equation 3.10, because it is simply a normalization of the posterior conditional distribution. Thus Equation 3.9 can be written as the following proportionality

$$q(\mathbf{m}|\mathbf{d}) \propto f(\mathbf{d}|\mathbf{m})p(\mathbf{m}). \tag{3.11}$$

Assume that the a priori distributions for model and data are given by multivariate normal (MVN) distributions. The model prior is then characterized by a mean, $\mathbf{m}_p$, and a covariance matrix, $\mathbf{C}_m$. Additionally, let the data covariance be given by $\mathbf{C}_d$. The model prior distribution can then be written as (Aster et al., 2013)

$$p(\mathbf{m}) \propto \exp\left[-\frac{1}{2}(\mathbf{m}-\mathbf{m}_p)^T\mathbf{C}_m^{-1}(\mathbf{m}-\mathbf{m}_p)\right], \tag{3.12}$$

and the conditional distribution for the data, given the model parameters is

$$f(\mathbf{d}|\mathbf{m}) \propto exp\left[-\frac{1}{2}(\mathbf{J}(\mathbf{m})-\mathbf{d})^T\mathbf{C}_d^{-1}(\mathbf{J}(\mathbf{m})-\mathbf{d})\right]. \tag{3.13}$$

Using Equation 3.12 and 3.13, in combination with Equation 3.11, an expression for the conditional distribution for the model parameters are given as

$$q(\mathbf{m}|\mathbf{d}) \propto \exp\left[-\frac{1}{2}\left((\mathbf{J}(\mathbf{m})-\mathbf{d})^T\mathbf{C}_d^{-1}(\mathbf{J}(\mathbf{m})-\mathbf{d})+(\mathbf{m}-\mathbf{m}_p)^T\mathbf{C}_m^{-1}(\mathbf{m}-\mathbf{m}_p)\right)\right]. \tag{3.14}$$

Since the logarithm is a monotonic function, maximizing the logarithm of Equation 3.14 gives the same result as maximizing the exponential. Thus, the argument of the exponential is considered as the objective function in the inverse problem. Using the matrix square roots of $\mathbf{C}_m^{-1}$ and $\mathbf{C}_d^{-1}$, this objective function can be rewritten into the standard least squares problem (Aster et al., 2013).

For a linear measurement operation $\mathbf{Jm}$, a closed form of the maximum a posteriori (MAP) solution of the model parameters is then given by (Tarantola, 2005)

$$\tilde{\mathbf{m}} = \mathbf{m}_p + \tilde{\mathbf{C}}_m\mathbf{J}^T\mathbf{C}_d^{-1}\left(\mathbf{d}-\mathbf{J}\mathbf{m}_p\right), \tag{3.15}$$

where $\tilde{\mathbf{C}}_m$ is the posterior covariance matrix of the model parameters given by

$$\tilde{\mathbf{C}}_m = \left(\mathbf{J}^T \mathbf{C}_d^{-1} \mathbf{J} + \mathbf{C}_m^{-1}\right)^{-1}. \tag{3.16}$$

3.4 Summary

In this chapter, the reader has been presented with the general case of solving ill-posed inverse problems. The deterministic method for solving overdetermined inverse problems was demonstrated by the classical example of fitting a straight line to points by minimizing the error. Furthermore, the method of Tikhonov regularization for solving the ill-posed inverse problem, was presented.

At the end of this chapter, a Bayesian approach, which is a fundamentally different alternative method of solving inverse problems, was discussed. By formulating the data and model parameters as Gaussian distributions, Baye's theorem gave an expression for the posterior objective function, which was solved using the maximum likelihood principle. The MAP solution was expressed by the data vector, model operator and prior distributions. Thus, the Bayesian approach provides a natural way of incorporating prior information to solve ill-posed inverse problems.

In the next chapters, these methods will be used for solving inverse seismic waveform problems, with the purpose of reconstructing velocities, given some seismic data measurements.

Chapter 4

Deterministic inversion of time-lapse seismic waveform data

4.1 Introduction

There exist numerous different approaches for inverse waveform modelling. Two well-known methods for classical inversion, originating from inverse scattering theory, are the Born iterative (Wang and Chew, 1989), and Distorted Born iterative (Chew and Wang, 1990). The main difference between these two methods, is that the distorted Born iterative method also update the background medium at each iteration. In both methods, at every inversion step, a computationally expensive forward simulation is required. Jakobsen and Ursin (2015) modified the Born iterative and distorted Born iterative methods to eliminate the need to do a full forward simulation by the use of the T-matrix, which is derived in Chapter 2.6. The use of a static background medium may provide sufficient inversion results using Born iterative T-matrix inversion (provided the velocity contrast are moderate), but it was concluded that the distorted Born iterative T-matrix method provided superior inversion results using a dynamic (variational) background medium. For that reason, distorted Born iterative T-matrix is used in the deterministic inversions in this thesis.

In this chapter, there will be a derivation of the distorted Born iterative T-matrix method. Then there will a discussion of different time-lapse inversion strategies. In the end, a full waveform inversion is performed in two time-lapse experiments, first using the 2D reservoir model presented in Chapter 2.7, then in the Marmousi model which is to be presented in this chapter.

4.2 Distorted Born iterative T-matrix method

The distorted Born iterative T-matrix method is a frequency domain full waveform inversion method, developed by Jakobsen and Ursin (2015), and is an iterative solver that utilizes the variational T-matrix for updating the Green's functions, given by

$$\mathbf{G}^{(i+1)} = \mathbf{G}^{(i)} + \bar{\mathbf{G}}^{(i)} \delta\mathbf{T}^{(i+1)} \mathbf{G}^{(i)}, \tag{4.1}$$

where $\bar{\mathbf{G}}$ is the discretized source-dependent Green's function which includes the ω^2 factor, as defined in Equation 2.29. The variational T-matrix is defined as

$$\delta\mathbf{T} = (\mathbf{I} - \delta\mathbf{V}^{(i+1)} \bar{\mathbf{G}}_{VV}^{(i)})^{-1} \delta\mathbf{V}^{(i+1)}, \tag{4.2}$$

where the perturbed contrast for the next iteration is calculated as

$$\delta\mathbf{V}^{(i+1)} = \mathbf{V}^{(i+1)} - \mathbf{V}^{(i)}, \tag{4.3}$$

using the definition of the matrix $\mathbf{V}$, which is given by Equation 2.28. Following Jakobsen and Ursin (2015), the data residual, $\delta\mathbf{d}^{(i)}$, is defined as the scattered wavefield for the difference in estimated scattering potential between two iterations, written as

$$\delta\mathbf{d}^{(i)} \equiv \left(\mathbf{G}_{RS} - \mathbf{G}_{RV}^{(i)}\right) \mathbf{f}_S = \bar{\mathbf{G}}_{RV}^{(i)} \delta\mathbf{V}^{(i+1)} \mathbf{G}_{VS}^{(i)} \tilde{\mathbf{f}}_S. \tag{4.4}$$

This can be interpreted as a linearization of the forward model around the i'th inversion result. Assume N_j discrete frequencies are are given by $\omega_j = j\delta\omega$, where $\delta\omega$ is the lowest frequency and $j = 1, \ldots, N_j$. Using same the discretizaiton scheme from Chapter 2.5, and the definition of $\mathbf{V}$ given by Equation 2.28, the above Equation 4.4 can be rewritten into it's component form exactly, as

$$\delta d_{r,sj}^{(i)} = \sum_{n=1}^{N} J_{rn,sj}^{(i)} \delta\chi_n^{(i+1)}. \tag{4.5}$$

In the equation above, $\delta\chi_n^{(i+1)}$ gives the difference of estimated contrast function between two iterations,

$$\delta\boldsymbol{\chi}^{(i+1)} = \boldsymbol{\chi}^{(i+1)} - \boldsymbol{\chi}^{(i)}, \tag{4.6}$$

and the model operator $J_{rn,sj}$ at the i'th iteration is given by

$$J_{rn,sj} = [\bar{G}^{(i)}_{rn,j} \Delta V_n G^{(i)}_{ns,j}]\tilde{\mathbf{f}}_s. \tag{4.7}$$

The components of Equation 4.6 is defined as

$$\chi_n^{(i)} = \left(\frac{1}{c_n^{(i)}}\right)^2 - \left(\frac{1}{c_n^{(0)}}\right)^2, \tag{4.8}$$

where c_n and $c_n^{(0)}$ are the estimated wave velocity in grid block n at the ith iteration in the actual and background medium. This implies that $\delta\chi_n^{(i+1)}$ can be written as

$$\delta\chi_n^{(i+1)} = \left(\frac{1}{c_n^{(i+1)}}\right)^2 - \left(\frac{1}{c_n^{(i)}}\right)^2. \tag{4.9}$$

$J_{rn,sj}$ is the sensitivity of the scattered wavefield data, and can be associated with the Born operator. For easy implementation, the three indices r, s and j is replaced by the combination counter α, where

$$\alpha = 1, \ldots, N_d, \tag{4.10}$$

where

$$N_d = N_r N_s N_j. \tag{4.11}$$

Thus, Equation (4.5) can be rewritten as

$$\delta d_\alpha^{(i)} = \sum_{n=1}^{N} J^{(i)}_{\alpha,n} \delta\chi_n^{(i+1)}, \tag{4.12}$$

or in matrix notation,

$$\delta\mathbf{d}^{(i)} = \mathbf{J}^{(i)} \delta\boldsymbol{\chi}^{(i+1)}. \tag{4.13}$$

Equation 4.13 gives a linear relationship between the (change in) model parameters and the calculated scattered wavefield, and can be solved using Tikhonov regularization, presented in Section (3.2.3), by minimizing the following objective function for each iteration

$$E(\delta\boldsymbol{\chi}^{(i+1)}) = \left|\left|\delta\mathbf{d}^{(i)} - \mathbf{J}^{(i)}\boldsymbol{\chi}^{(i+1)}\right|\right|^2 + (\lambda^{(i)})^2 \left|\left|\delta\boldsymbol{\chi}^{(i+1)}\right|\right|. \tag{4.14}$$

This may be a highly ill-posed problem, and may be stabilized at every iteration by using the cooling scheme given by (Farquharson and Oldenburg, 2004)

$$\lambda^{(i)} = max(\lambda a^{(i-1)}, \lambda^*), \tag{4.15}$$

where $0.1 < a < 0.9$ and λ^* is an optimal value determined by for example the L-curve method (Hansen, 1997) or the discrepancy principle (Constable et al., 1987), which will be further explained in Section 4.4.1. The regularization parameter, λ^*, is the one for which the data error, defined by $||\delta\mathbf{d}^{(i)} - \mathbf{J}^{(i)}\boldsymbol{\chi}^{(i}|| \;/\; ||\delta\mathbf{d}^{(i)}||$, is at minimum (Farquharson and Oldenburg, 2004). Choice of initial regularization parameter may depend on the amount of random noise and size of the inverted model. Thus, the choice of λ will be discussed each individual experiment. The closed form solution of the distorted Born iterative T-matrix for the model parameters can then be written as

$$\boldsymbol{\chi}^{(i+1)} = \boldsymbol{\chi}(i) + \left(\mathbf{H}^{(i)} + (\lambda^{(i)})^2\mathbf{I}\right)^{-1}\mathbf{V}^{(i)}, \tag{4.16}$$

where $\mathbf{V}^{(i)}$, and $\mathbf{H}^{(i)}$, are the gradient vector, and the Hessian matrix, at the i'th iteration, respectively. They are given by (Jakobsen and Ursin, 2015)

$$\mathbf{V}^{(i)} = \Re\left[\left(\mathbf{J}^{(i)}\right)^{\dagger}\delta\mathbf{d}^{(i)}\right], \tag{4.17}$$

and

$$\mathbf{H}^{(i)} = \Re\left[\left(\mathbf{J}^{(i)}\right)^{\dagger}\left(\mathbf{J}^{(i)}\right)\right], \tag{4.18}$$

and the data residual, $\delta\mathbf{d}^{(i)}$ in Equation 4.16 and 4.17 is given by

$$\delta\mathbf{d}^{(i)} = \delta\mathbf{d}_{obs} - \mathbf{J}^{(i)}\boldsymbol{\chi}^{(i)}, \tag{4.19}$$

where $\delta\mathbf{d}_{obs}$ is the observed scattered wavefield. Using this iterative method, it is possible to invert the scattered data for complex geological structures.

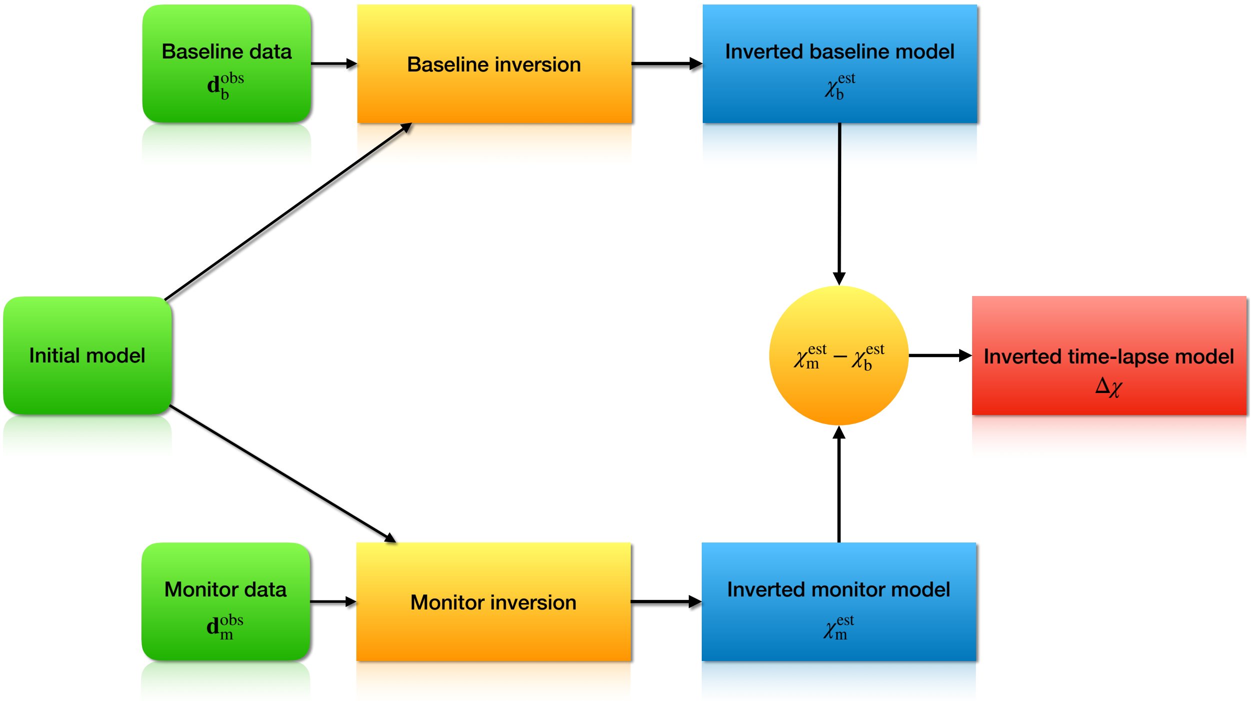

Figure 4.1: *Diagram of the work flow for the parallel-difference strategy*

4.3 Time-lapse inversion strategies

Seismic time-lapse inversion, which is sometimes called 4D seismic inversion due to the acquisition of multiple 3D data-sets through the passing of time, can be defined as the inversion for the change of elastic parameters in a reservoir. The inversion is based on seismic data before production, $\mathbf{d_b}$ (b for baseline data), and data after some time of production, $\mathbf{d_m}$, (m for monitor data). The inverted time-lapse model is then obtained by subtracting the inverted baseline model, $\boldsymbol{\chi}_b$, from the inverted monitor model, $\boldsymbol{\chi}_m$

$$\Delta\boldsymbol{\chi} = \boldsymbol{\chi}_m - \boldsymbol{\chi}_b.$$

There are different ways of obtaining inverted time-lapse models of the change in velocities. Inversion of the baseline and monitor models can be performed completely separately parallel strategy (Plessix et al., 2010), as seen in Figure 4.1. In this case, no additional information from baseline inversions is used as prior in monitor inversions. There will now be given some details regarding two alternative approaches, known as the sequential difference and double difference time-lapse strategies.

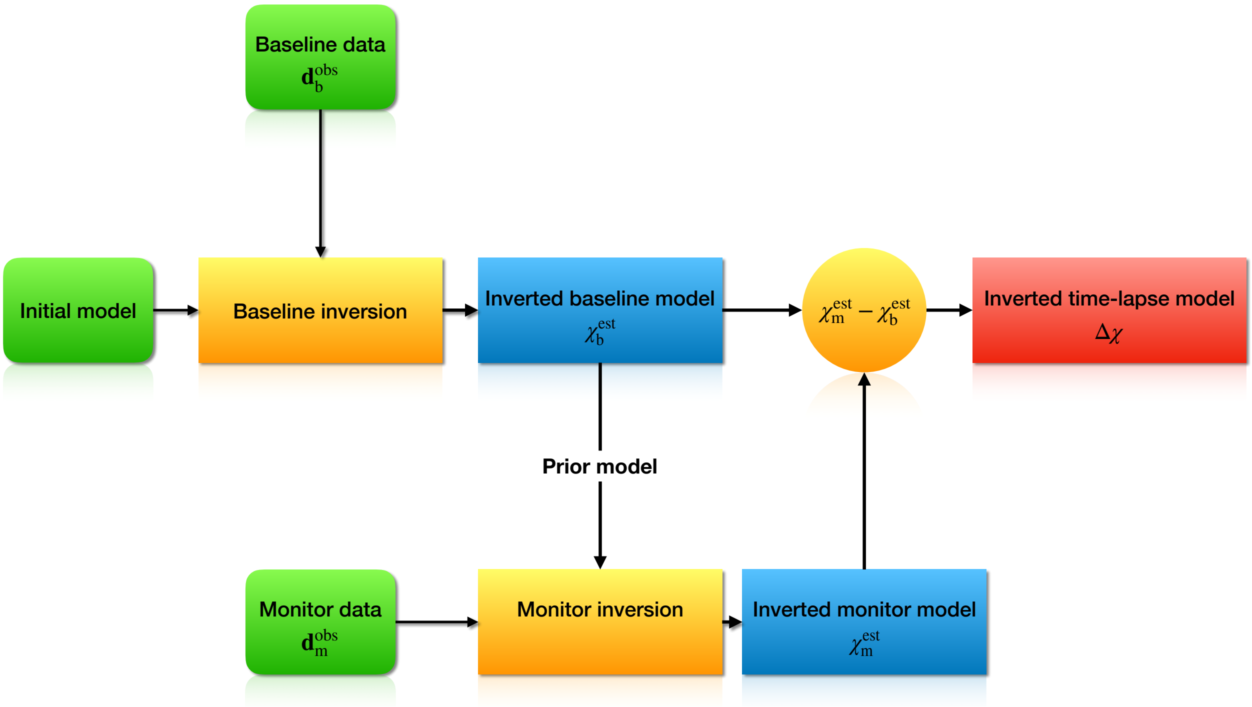

Figure 4.2: *Diagram of the work-flow for the sequential-difference strategy*

4.3.1 Sequential difference strategy

The sequential difference time-lapse is based on the parallel approach. While the baseline inversion is performed in the same manner for parallel and sequential-difference, the monitor inversion for the sequential strategy, is slightly different. Since the time-lapse effects can be assumed to be small compared to the geological complexity of a realistic model, the inverted baseline model seems a natural choice as the initial model used in the monitor inversion. Given that a reservoir would already be under production, it would be reasonable to assume that some prior information about the reservoir already exists when the monitor survey is performed. It would then be beneficial to use posterior knowledge from the baseline inversion as prior in the monitor inversion. This is often called sequential time-lapse, since the monitor inversion is done in a succeeding manner. This may motivate for faster convergence and more accurate inversion results. The inverse problem of finding the model parameters for the baseline and monitor can be solved separately using Tikhonov regularization by minimizing Equation 3.7 for the baseline and monitor as

$$E(\boldsymbol{\chi}_b^{(est)}) = ||\mathbf{d}_b - \mathbf{J}_b\boldsymbol{\chi}_b^{(est)}||_2^2 - \lambda_b^2||\mathbf{F}\boldsymbol{\chi}_b^{(est)}||_2^2 \tag{4.20}$$

and

$$E(\boldsymbol{\chi}_m^{(est)}) = ||\mathbf{d}_m - \mathbf{J}_m\boldsymbol{\chi}_m^{(est)}||_2^2 - \lambda_m^2||\mathbf{F}\boldsymbol{\chi}_m^{(est)}||_2^2, \tag{4.21}$$

respectively. $\mathbf{J}_b$ and $\mathbf{J}_m$ are the linearized model operators, and $\boldsymbol{\chi}_b^{(est)}$ and $\boldsymbol{\chi}_m^{(est)}$ are the model parameters for the baseline and monitor, respectively. The time-lapse of the change in model parameters is obtained by subtracting the inverted baseline model from the inverted monitor model, as can be seen in the work-flow in Figure (4.2).

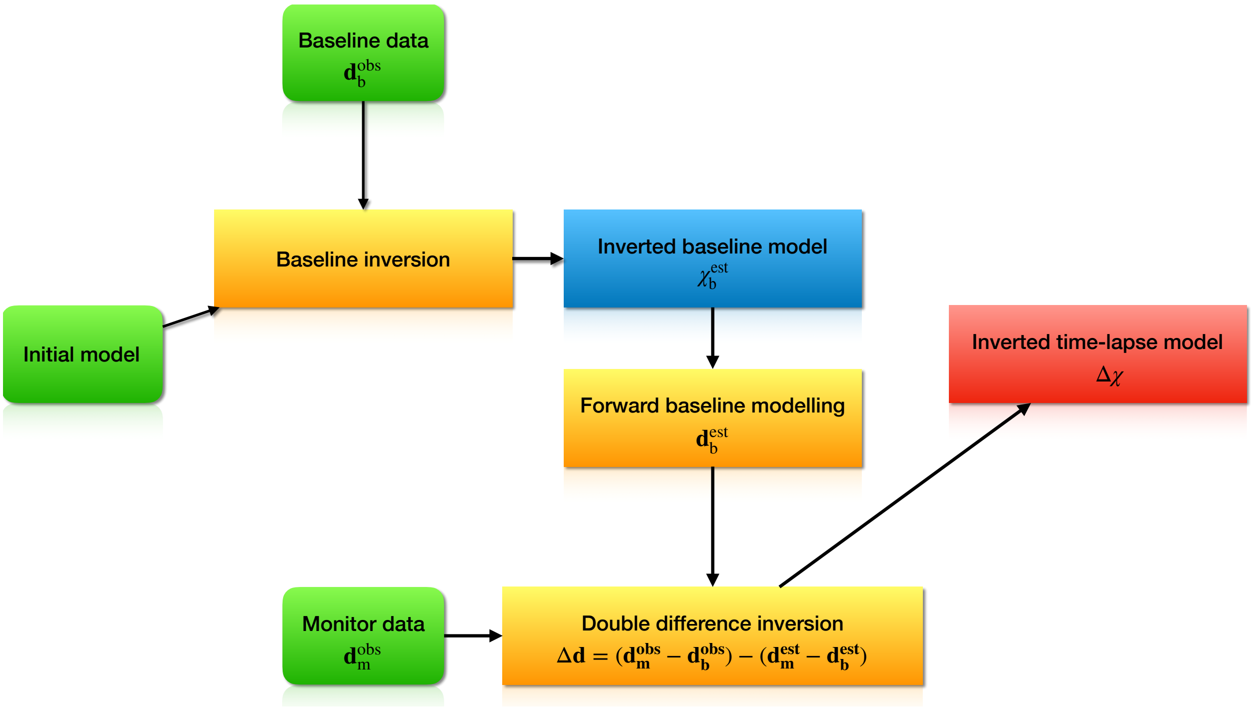

Figure 4.3: *Diagram of the work-flow for the double-difference strategy*

4.3.2 Double difference strategy

The strategy was originally developed by Waldhauser and Ellsworth (2000) for the double difference of the measured and estimated travel-time as an improvement of obtaining earthquake hypocenter locations. In a similar way, double difference waveform inversion in frequency domain was proposed by Watanabe et al. (2004). The time-lapse estimation of the double difference strategy is obtained by minimizing the difference in the observed data, between monitor and baseline and the difference in the estimated data, between monitor and baseline (see for example Watanabe et al., 2004; Denli and Huang, 2009; Asnaashari et al., 2015). This requires that a reconstruction of the baseline model has already been performed (see the work-flow is illustrated in Figure 4.3). The time-lapse difference can then be expressed as

$$\Delta \mathbf{d} = (\mathbf{d}_m^{(obs)} - \mathbf{d}_b^{(obs)}) - (\mathbf{d}_m^{(est)} - \mathbf{d}_b^{(est)}) = \mathbf{d}_{time-lapse}^{(obs)} - \mathbf{d}_{time-lapse}^{(est)}. \tag{4.22}$$

It is then possible to solve the minimization problem (for example by the use of distorted Born T-matrix method, as discussed in the previos section) for the estimated change in model parameters, i.e.

$$\Delta \boldsymbol{\chi} = \boldsymbol{\chi}_m - \boldsymbol{\chi}_b. \tag{4.23}$$

4.4 Numerical results

In this section, two time-lapse full waveform inversion experiments have been performed using the DBIT method. The first experiment was performed on the 2D reservoir P-wave velocity model, presented in Chapter 2. The second experiment was performed on the re-sampled sub-grid of the Marmousi model (to be presented). For the time-lapse experiments to be more realistic, complex random Gaussian noise has been added to the data. This was done by constructing a vector $\mathbf{w} = \mathbf{v}_1 + i\mathbf{v}_2$, where $\mathbf{v}_1$ and $\mathbf{v}_2$ contains normally distributed random numbers of the same length as the data. The vector $\mathbf{w}$ was scaled according to a desired noise level, given by a signal to noise ratio (SNR) is defined as

$$SNR = 10^{\frac{SNR_{dB}}{20}}, \tag{4.24}$$

where SNR_{dB} is the SNR given in decibels. The vector $\mathbf{w}$ was then scaled and added to the synthetic data, using (Jakobsen and Ursin, 2015)

$$d_{noisy} = d + \frac{||\mathbf{d}||_2}{\sqrt{SNR}||\mathbf{w}||_2}\mathbf{w}. \tag{4.25}$$

4.4.1 Sequential time-lapse inversion of a simple reservoir model

In this experiment, an attempt was made to reconstruct a time-lapse effect in the 2D reservoir model, shown in Figure 2.3. The sequential time-lapse inversion strategy, illustrated in Figure 4.2, has been used. The numerical experiment was done in the following order. First the baseline model was reconstructed. This was followed by the inversion of the monitor model. The time-lapse effect was then obtained by subtracting the inverted baseline model from the inverted monitor model.

A survey design, consisting of a total number of 82 receivers and 46 sources, were used in both the baseline and monitor survey of the reservoir model. The sources and receivers were uniformly distributed on the surface at $z = 0$ m. Synthetic data were generated using the full integral equation T-matrix method with a source function corresponding to a Ricker wavelet with a centre frequency of 7.5 Hz that was sampled every 10 ms for a total of 3 s. The source function in time and frequency domain can be seen in Figure 2.2. Complex Gaussian noise was added to the synthetic waveform data for both baseline and monitor data, corresponding to a SNR of 30 dB, in order to make the experiment more realistic. For the baseline inversion, a model with gradual increasing velocity as a function of depth was used as initial model (see Figure 4.4). The inversion process was done in a sequential manner, starting with the lowest frequency of 2 Hz and inverting for every integer frequency up to 20 Hz. Thus, a total number of 19 frequencies were used in the inversion process. A regularization parameter at every iteration was chosen by the following cooling scheme

$$\lambda^{(i)} = \lambda_0 \alpha^{(i-1)}. \tag{4.26}$$

Both the initial regularization and cooling parameter, $\lambda_0 = 0.01$ and $\alpha = 0.8$, respectively, were chosen by trial and error. The discrepancy principle was used, i.e. the program were set to iterate until a satisfactory low data error was obtained for each frequency. A maximum of 30 iterations were allowed. The inversion result for the reconstructed baseline model is shown i Figure 4.5a.

The monitor inversion was performed in the exact same manner as the baseline reconstruction, except for the choice of initial model. For this purpose, the reconstructed baseline model was used. The inverted monitor model can be seen in Figure 4.5b. To obtain the estimated time-lapse effect, the baseline model was subtracted from the monitor model. The predicted time-lapse is shown in Figure 4.5c.

4.4.2 Sequential time-lapse inversion of the Marmousi model

The Marmousi2 P-wave velocity model, made by Martin et al., 2006, is a part of the elastic upgrade that was made based on the original Marmousi model. It contains a gas-reservoir surrounded by complex geology, such as tilted fault blocks and varying sediment deposits.

For the studies performed in this thesis, a sub-set of the Marmousi2 model has been re-sampled to 49 × 109 number of grid blocks with equal size of 20 m in each direction. The horizontal length of the survey area is 2180 m and the depth is 980 m. The re-sampled sub-set of the Marmousi2 P-wave velocity model is from now on referred to as the baseline Marmousi model and can be seen in Figure 4.6a. A velocity change of 300 m/s in the have been added to a small region of the baseline Marmousi model. This is performed to mimic a time-lapse effect that could for instance be caused by the production of hydrocarbons from the gas reservoir. This new model is referred to as the monitor Marmousi model and can be seen in Figure 4.6b. The main goal in this time-lapse inversion is to reconstruct the actual time-lapse effect which can be seen in Figure 4.6c.

The following source and receiver configurations were used in both the baseline and monitor survey. 109 receivers and 49 sources were deployed on the surface of the model at $z = 0$ m with uniform spacing. To generate synthetic waveform data, a Ricker wavelet with centre frequency of 7.5 Hz was used as source function with a sampling interval of 10 ms and a total recording length of 3 s. Synthetic waveform data were generated using the full integral equation T-matrix method, first for the baseline model, then for the monitor model. The same parameters in the forward modelling was used in both baseline and monitor data generations. Complex Gaussian noise was added to both baseline and monitor data, with a corresponding SNR of 30dB. Inversion was performed using the DBIT method. The initial model for the baseline inversion can be seen in Figure 4.4b, and is a laterally homogeneous, depth-dependent velocity model. The regularization parameter was chosen according to the cooling sceme given in Equation 4.26, with initial regularization and cooling parameter, $\lambda_0 = 0.01$ and $\alpha = 0.75$, respectively, chosen by trial and error. The inversion for both baseline and monitor was done in a sequential manner, starting with the lowest frequency of 2 Hz and inverting for every integer frequencies up to 20 Hz. The iterations continued until the stopping criterion of a low data error was obtained or a maximum of 30 iterations had been performed. The inverted baseline model can be seen in Figure 4.7a

For the monitor inversion, the reconstructed baseline model was used as initial model. This assured faster convergence and considerable amount of fewer iterations were observed. In other words. One can say the inversion result was ”pushed” closer to the actual monitor model. For this inversion, an initial regularization and cooling parameter, $\lambda_0 = 0.01$ and $\alpha = 0.5$, were chosen, respectively. The resulting inverted monitor model can be seen in

Figure 4.7b. By subtracting the reconstructed baseline model from the inverted monitor model, a time-lapse image of the change in model parameters was obtained and can be seen in Figure 4.7c.

4.5 Discussion

Full waveform inversion using the DBIT method has successfully been able to reconstruct the baseline and monitor model of the 2D reservoir. Good results were even obtained in the more complex Marmousi model. A relatively accurate reconstruction of the time-lapse effect in the 2D reservoir model, was obtained. Almost no artefacts can be observed outside the area with time-lapse change (see Figure 4.5c). On the other hand, the time-lapse effect itself contains some over- and underestimations. The time-lapse effect of the Marmousi model was very accurately reconstructed, however, there are a considerate amount of noise outside the area of the time-lapse effect (see Figure 4.7c). This is most likely due to the fact that in the inversion process of the monitor model, the reconstructed baseline model was used as initial model. This may have caused the monitor inversion to recover properties that were not properly recovered in the baseline model. Thus, in the subtraction of the baseline model from the monitor model, some extra recovered information contained in the monitor model was transformed into artefacts in the reconstructed time-lapse model.

The double difference time-lapse strategy have previously been demonstrated to be more robust than the sequential difference (see for example Zhang and Huang, 2013). On the other hand, application of the double difference strategy to real seismic data could be dangerous if some of the data differences in the monitor and baseline model does not originate from the seismic response (Yang et al., 2015). Furthermore, if the baseline model has been accurately recovered, the sequential strategy can be attractive because it tend to recover parts of the model that would not have been fully reconstructed before (Asnaashari et al., 2015).

This experiment has demonstrated the importance of being aware of the cause of artefacts in seismic time-lapse imaging, and the seriousness of having an accurate recovered baseline model when performing time-lapse experiments using the sequential difference. If, however, one possesses sufficient prior knowledge about the reservoir location, in addition to some insight on the time-lapse effect itself, the artefacts outside the area of time-lapse change could in some cases be ignored.

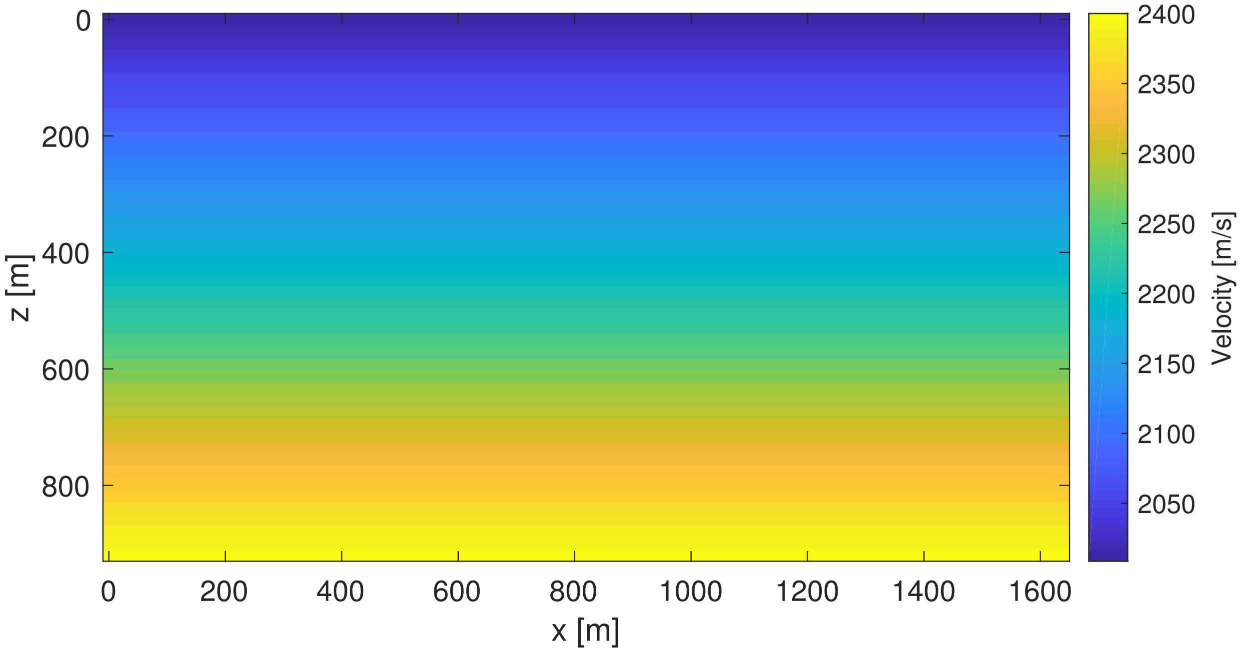
(a) *Initial model for reservoir model*

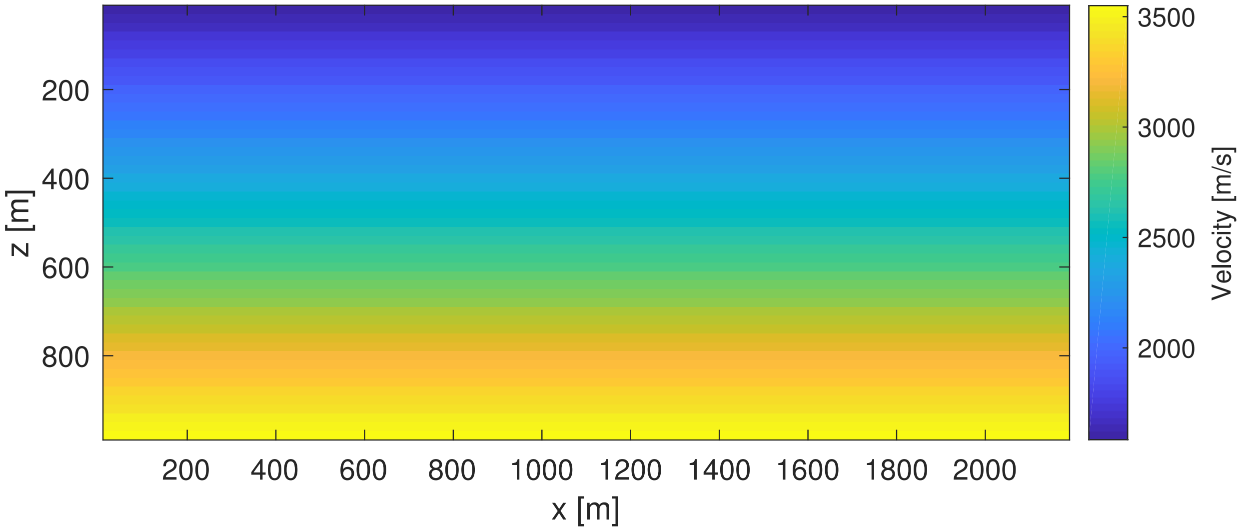
(b) *Initial model for Marmousi baseline*

Figure 4.4: *Depth dependent velocity models used as the initial model in the baseline inversion of; 4.4a the 2D reservoir model and 4.4b the Marmousi model.*

(a) *Reconstructed baseline model*

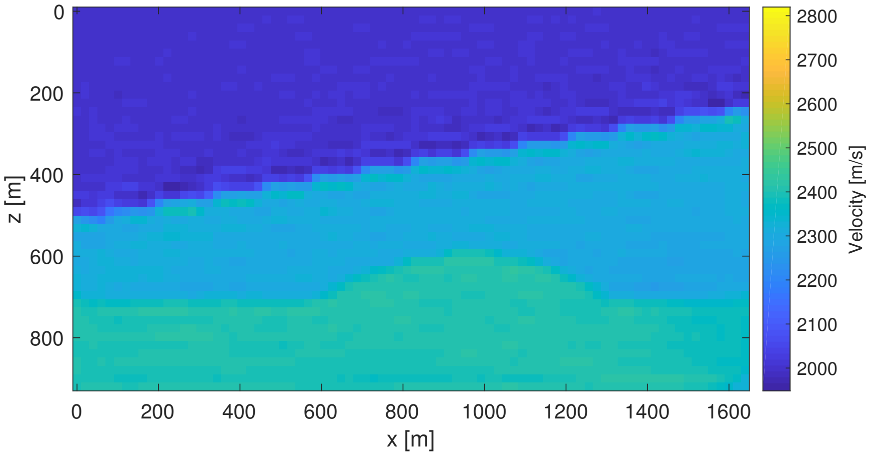

(b) *Reconstructed monitor model*

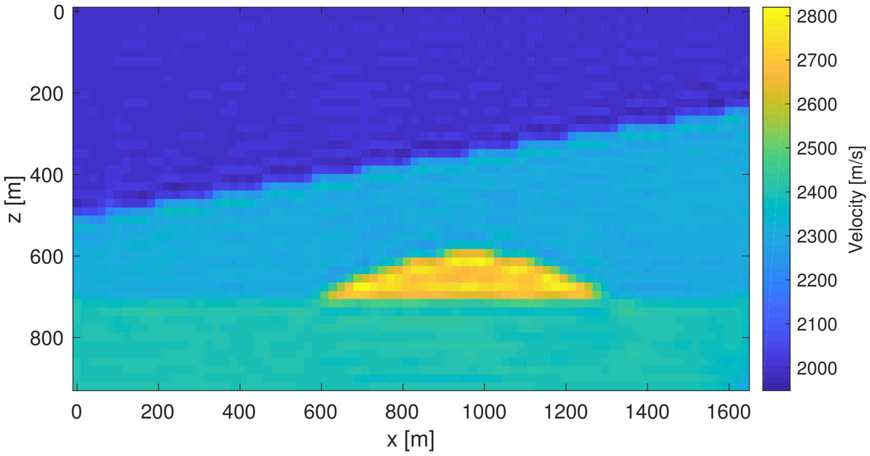

(c) *Reconstructed time-lapse*

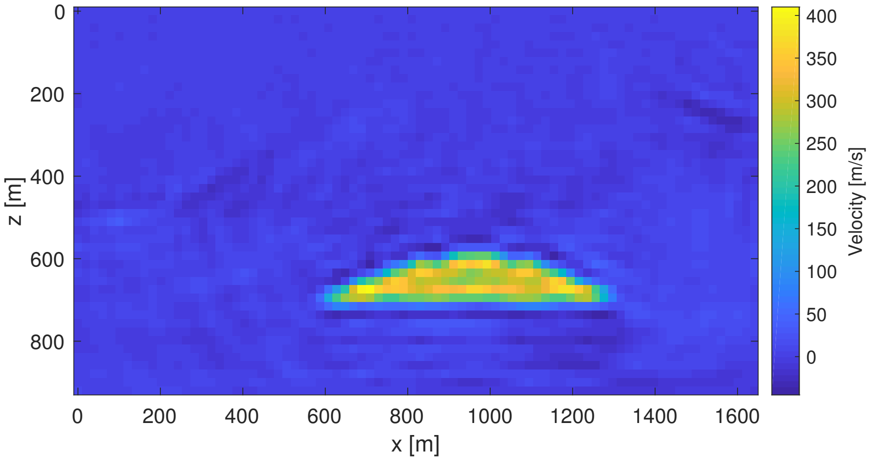

Figure 4.5: *Sequential time-lapse experiment in the 2D reservoir model. Reconstructed baseline (4.5a), monitor (4.5b) and time-lapse effect (4.5c). The inversions was done using the distorted Born iterative T-matrix inversion method and noise with SNR of 30 dB was added to the data components. All integer frequencies from 2 Hz up to 20 Hz were used*

(a) *Actual baseline model*

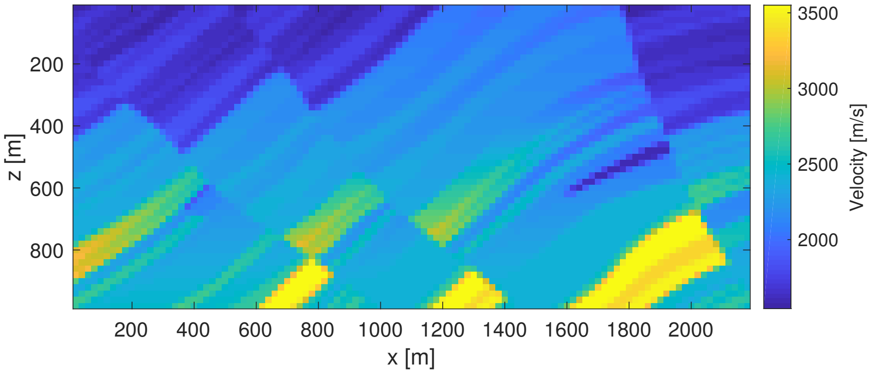

(b) *Actual monitor model*

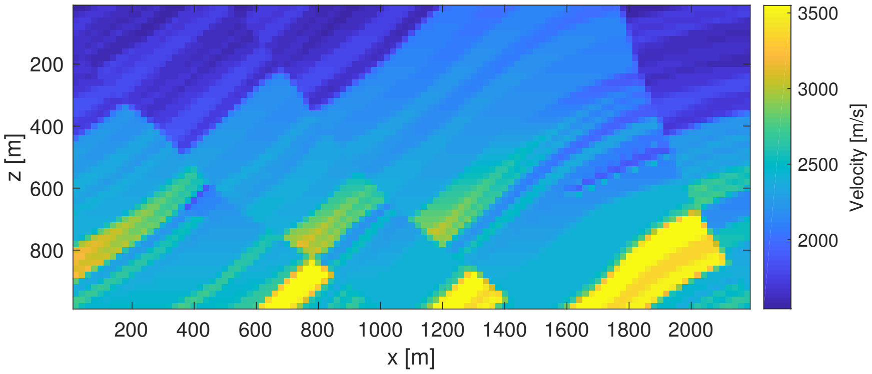

(c) *Actual time-lapse effect*

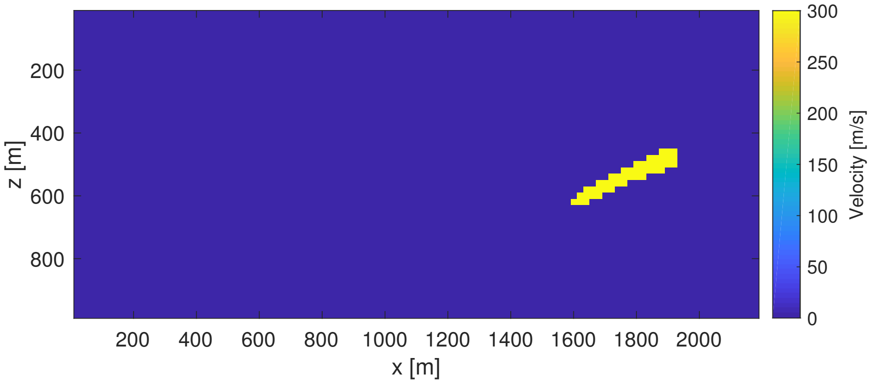

Figure 4.6: *Marmousi model of baseline (4.6a), monitor (4.6b) and time-lapse effect (4.6c).*

(a) *Reconstructed baseline model*

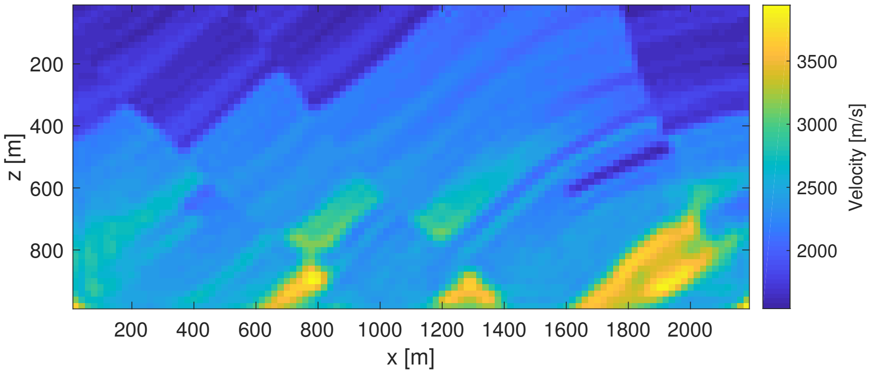

(b) *Reconstructed monitor model*

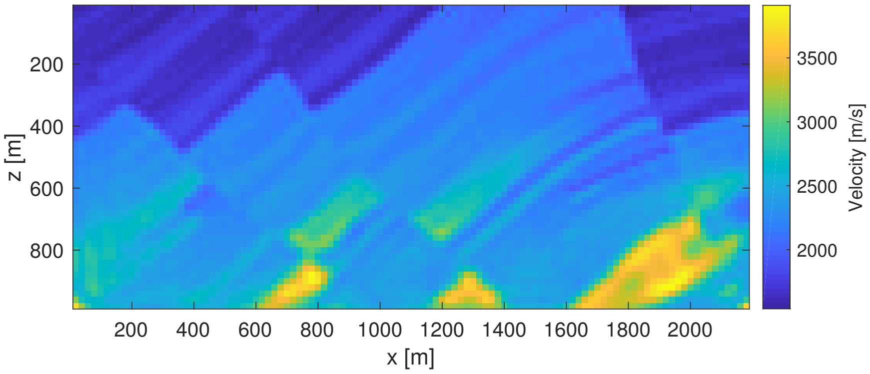

(c) *Reconstructed time-lapse*

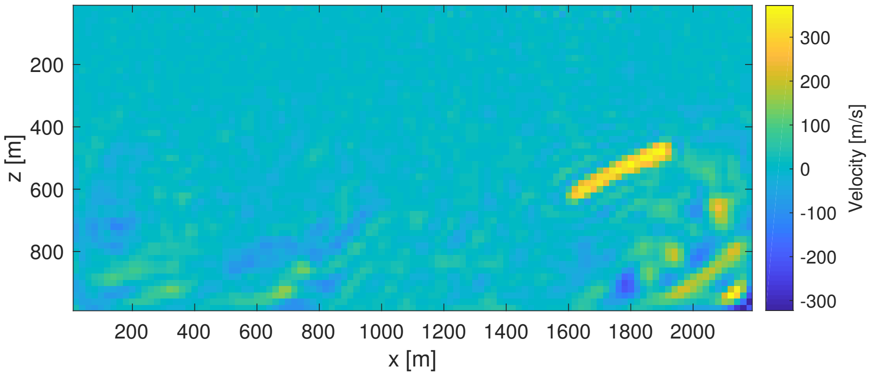

Figure 4.7: *Sequential time-lapse experiment in the re-sampled sub-grid of the Marmousi model Reconstructed baseline (4.7a), monitor (4.7b) and time-lapse effect (4.7c). The inversions was done using the distorted Born iterative T-matrix inversion method and noise with SNR of 30 dB was added to the data components. All integer frequencies from 2 Hz up to 20 Hz were used*

Chapter 5

Linear Bayesian inversion of time-lapse seismic data

5.1 Introduction

In the previous chapter, classic full waveform inversion has been applied to time-lapse seismic waveform data by use of regularization methods. However, in this chapter a Bayesian formulation of the inverse problem will be used, which solves the inverse problems for probability density functions that is expressed in the certainty of the estimates. As previously mentioned, time-lapse seismic data could be used to complement the updating of a reservoir model (referred to in litterature as history matching). During the integration of time-lapse seismic data and observed reservoir production data in ensemble based history matching, the posession of accurate weights to be applied for the fundamentally different data-sets is of great importance (Oliver and Chen, 2011).

In this chapter, the focus will be on the linear Bayesian inversion, which incorporates uncertainties by nature. First, some details will be presented on the implementation of linear Bayesian time-lapse seismic inversion. This will be followed by two numerical experiments where a Bayesian formulation of the linearised inverse time-lapse problem will be applied in the Marmousi model, as presented in Chapter 4.4.2. The first experiment will be performed using the actual baseline model as backgrond (reference) model. The second experiment will make use of the reconstructed baseline model from the previous chapter.

5.2 Implementation

To obtain a MAP solution (defined by Equation 3.15 and 3.16) of the time-lapse contrasts using linear Bayesian inversion, the forward model is linearised about some background medium, for instance the actual baseline model, and the change in model parameter (time-lapse) is inverted for using the distorted Born approximation to estimate the scattered wave-field. As was discussed in Section 2.4, the implementation of Born approximation for time-lapse inversion should be feasible if the perturbation between the baseline and monitor models is not too large. Time-lapse changes are usually small in nature, i.e. the hydrocarbon production mainly affects a small, restricted area, i.e. the actual reservoir, relative to a larger survey domain. Thus, the Born approximation may be considered valid in its role of approximating the scattered wave-field for a time-lapse change. Green's functions for the baseline medium can be calculated by the exact integral equation using the T-matrix, and is given by Equation 2.58. Using the calculated Green's functions for the baseline model, $\bar{\mathbf{G}}^{(b)}_{RV}$ and $\mathbf{G}^{(b)}_{VS}$, the scattered wave-field from a time-lapse effect, $\Delta\mathbf{d}$, could be estimated using the distorted Born approximation,

$$\Delta\mathbf{d} \equiv \bar{\mathbf{G}}^{(b)}_{RV}(\mathbf{V}^{(m)} - \mathbf{V}^{(b)})\mathbf{G}^{(b)}_{VS}\tilde{\mathbf{f}}_S. \tag{5.1}$$

In the equation above, $\bar{\mathbf{G}}^{(b)}_{RV}$ is the source-independent scattering to receiver domain Green's function, and $\mathbf{G}^{(b)}_{VS}$ is that of source-dependent source to scattering volume. For multiple sources (s) and discrete frequencies (j), Equation 5.1 can be written to its component form in the same way as was done in Chapter 2.5, using the combination counter, $\alpha = 1, \ldots, N_d = N_r N_s N_j$, to keep track of the data parameters. The Equation becomes

$$\Delta d_\alpha = \sum_{\alpha=1}^{Nd} J_{\alpha n}\Delta\chi_n, \tag{5.2}$$

or in matrix notation

$$\Delta\mathbf{d} = \mathbf{J}\boldsymbol{\Delta}\chi, \tag{5.3}$$

where the components of the matrix $\mathbf{J}$ are given by

$$J_{\alpha n} = G^{(b)}_{rn}(\omega_j)G^{(b)}_{ns}(\omega_j)\tilde{f}_s. \tag{5.4}$$

and $\Delta\boldsymbol{\chi} = \boldsymbol{\chi}^{(m)} - \boldsymbol{\chi}^{(b)}$ is the time-lapse change in the model parameters, as defined in Equation 2.9. This approach is similar to that of the double difference strategy where the inversion process is done directly for the difference in the model parameters. Using this method, a distorted Born approximation is used to estimate the scattered wave-field originating from the time-lapse change.

The prior information can for example come from well logs and geological knowledge of the survey area (Eikrem et al., 2016). The prior mean, $\mathbf{m}_p$, of the model is then given by a vector containing the expected mean values of the model parameters defined in Equation 2.9. In the time-lapse experiments to be tested in this thesis, all expected model parameters are set equal to zero. This is a reasonable choice, because the 4D effect of the hydrocarbon production will be restricted to the small part of a reservoir, and not the whole survey domain, which will remain unchanged. For the construction of the prior covariance matrix for the model parameters, $\mathbf{C}_m$, there are several approaches. In the case of no correlation (which can be assumed for simplicity), the diagonal elements are set equal to the expected variance, and padded with zeroes everywhere else. In most cases of time-lapse inversion, some correlation might be reasonable to assume because the change of a parameter in the model function is expected to be higher if it is located close to another model parameter with a change of significant magnitude. In the case of correlation, the prior covariance matrix is made using a variogram (see e.g. Eikrem et al., 2017) where the horizontal, vertical or equal correlation is defined by some length in horizontal and vertical direction. The data covariance matrix, $\mathbf{C}_d$, is a diagonal matrix with the variance of a new realization of the same distribution of the Gaussian random noise that was added to the data. It is then possible to use the Bayesian formulations derived in Chapter 3.3, i.e. Equation 3.15 and 3.16, for the MAP solution and corresponding posterior covariance matrix, respectively, when the prior information is defined as above.

5.3 Numerical results

In this section, two time-lapse experiments in the Marmousi model (as presented in the previous chapter) will be made. First, a Bayesian time-lapse inversion will be performed using the actual baseline model as fixed background model, under the assumption that it is a given reconstructed baseline model. Next, the experiment will be repeated. However, instead of using the actual baseline model as the fixed background model, the reconstructed baseline model from the previous chapter will be applied for this task. Moreover, both experiments will be tested with high, medium and very low levels of noise.

5.3.1 Fixed baseline

The actual baseline Marmousi model (see Figure 5.1a) was used as background medium in the linear Bayesian time-lapse distorted Born approximation. To mimic the time-lapse effect of a producing reservoir, a relatively large change of 300 m/s in P-wave velocity, as shown in Figure 5.1b, was introduced into the Marmousi model. In this section, the time-lapse experiments will be performed under the assumption that the baseline model has already been reconstructed. This involves using the actual Marmousi model as baseline model.

Next, the Green's functions for the actual baseline Marmousi model were calculated using the exact integral equation T-matrix method, as given in Equation 2.58. Forward modelling was then performed using a Ricker wavelet with a centre frequency of 7.5Hz used as source. 60 receivers and 15 sources were uniformly distributed on the surface. The sampling time was 10 ms and the total recording time was 3 seconds. The Nyquist frequency was 50 Hz. However, since the inversion is going to be done for the frequency group of $2, 3, \ldots, 20$ Hz, data were only generated for the selected frequencies. The experiment was then made more realistic, by adding three different levels of complex Gaussian noise to the data, using the same method as presented in Chapter 4.4. The following SNRs were used; 100 dB, 30 dB and 4 dB, corresponding to 0.001 %, 3.16 % and 63.1 % noise, respectively. The data covariance matrix, $\mathbf{C}_d$, was set diagonal with elements corresponding to the variance of a (new) realization of noise, with the corresponding SNRs. Furthermore, it was assumed that some knowledge of the position of the reservoir is known. The prior model covariance matrix was then created using the following equation

$$\mathbf{C}_m = \mathbf{D}\mathbf{B}\mathbf{D}^T + \mathbf{D}_1. \tag{5.5}$$

Here, $\mathbf{D}$ is a diagonal matrix, with values representing the standard deviation of the expected change in contrast as a function. These values was set to decrease as a function of distance from the centre of where the time-lapse change was expected to be (Eikrem et al., 2018). Matrix $\mathbf{B}$ was made using a variogram, with practical range of 30×30 grid blocks and 1 on the diagonal. Matrix $\mathbf{D}_1$ is a diagonal matrix with a small number on the diagonal, making $\mathbf{C}_m$ invertible. The prior standard deviation can be seen in Figure 5.1c. The inversion was then performed using Equation 3.15 and 3.16. In Figure 5.2, the posterior standard deviations can be seen for the three different noise levels. Since the standard deviation (both prior and posterior) are given in contrasts, the MAP solutions are plotted in both contrast and velocities, see Figure 5.3 and 5.4, respectively. The error was calculated by subtracting the actual time-lapse velocities from the MAP solutions and are shown for all three noise levels in Figure 5.5.

Next, a smaller time-lapse change of 100 m/s was tested. The forward modelling and inversion was done in the exact same manner as described above, with the exception of the prior standard deviation of the contrast. Thus, the prior model covariance was calculated using Equation 5.5 with a slightly lower standard deviation than in the previous experiment to account for less time-lapse change. The model prior covariance can be seen in Figure 5.6c, and the posterior standard deviations of the model can be seen in Figure 5.7. The MAP solutions are plotted in both contrasts and velocities in Figure 5.8 and 5.9, respectively. Figure 5.10 shows the corresponding errors in the MAP solution, given in m/s.

5.3.2 Fixed reconstructed baseline

In the previous experiment, the actual Marmousi model was used as fixed background medium in the distorted Born approximation for the reconstruction of 300 m/s and 100 m/s time-lapse changes. Instead of using the actual baseline as the fixed background, this experiment will employ the reconstructed baseline Marmousi model from Chapter 4.4.2. The baseline model can be seen in Figure 5.11a.

First, a time-lapse effect of 300 m/s, as shown in Figure 5.11b, was used. Next, the Green's functions were calculated for the reconstructed baseline Marmousi model and the scattered time-lapse seismic data were generated as explained in the previous section. The experiment was performed for three different SNRs of 100 dB, 30 dB and 4 dB. The posterior standard deviation for the 300 m/s time-lapse experiment is shown in Figure 5.12. The obtained MAP solutions for the contrasts and velocities are shown in Figure 5.13 and 5.14, respectively, with the corresponding error in velocities shown in Figure 5.15.

Using the same fixed baseline model (see Figure 5.16a), the experiment was repeated with a lower time-lapse change of 100 m/s (shown in Figure 5.16b). The prior standard deviation of the model covariance matrix is shown in Figure 5.16c, and the resulting posterior standard deviation for all three SNRs, can be seen in Figure 5.17. MAP contrasts and velocities for the 100 m/s time-lapse effect are shown in Figure 5.18 and 5.19, respectively. Figure 5.20 shows the corresponding error in the velocities.

5.4 Discussion

In these experiments, a linear Bayesian inversion method has been used, in conjunction with the exact integral equation T-matrix method to generate the synthetic data. This is a method farily close to the double difference method, presented in Chapter 4.3.2, in the sense that the method inverts directly for the difference in model parameters to directly obtain the time-lapse estimate.

In the first experiment, where a time-lapse effect of 300 m/s was introduced in the monitor model, the time-lapse reconstruction performed impressively well in the case of practically no noise in the data (see Figure 5.4a). The corresponding error in the time-lapse estimate (see Figure 5.5a) shows that the inversion has quite successfully recovered the time-lapse effect, and the larger errors are restricted to the edges of the time-lapse effect. For stronger SNRs, artefacts in the lower left side of the time-lapse model can be observed (see Figure 5.4b and 5.4c). However, if one study the error between actual and reconstructed time-lapse models (see Figure 5.5b and 5.5c), the largest errors seems to be restricted to the edges, as in the noiseless inversion. As a consequence to the overestimation in one part of the model, the rest of the time-lapse effect seems to be underestimated and predicts a time-lapse effect varying from 200 m/s to 300 m/s, which is not that far from the actual time-lapse effect of 300 m/s. In other words, apart from the overestimated lower left part of the time-lapse reconstructions in the noisy cases, the inversion seems to predict the time-lapse effect to a certain level of accuracy. The posterior standard deviation tend give good indications on where one might expect large errors (see Figure 5.2). Furthermore, the posterior standard deviation is higher in the noisy reconstructions than in the noiseless inversion (see Figure 5.2). This trend is observed in all experiments (see Figure 5.2, 5.7, 5.12 and 5.17).

In the case 100 m/s velocity difference (see Figure 5.6), the error in the lower left part of the time-lapse effect seems to be less dramatic (see Figure 5.9). Diffraction points can be caused by abrupt change in seismic parameters, for instance P-wave velocity. The area at the lower left side of the estimated models, may thus be caused by a diffraction from the sharp and sudden change in velocity. This problem could potentially be solved by the use of a finer resolved model. In Figure 5.9, the time-lapse change is relative accurately reconstructed, even using the noisy data.

When the reconstructed Marmousi baseline model (see Figure 5.11) is used as the fixed background medium in the inversion for the 300 m/s velocity contrast, the MAP solutions (Figure 5.14) tend to be more accurate than when the actual baseline model was used (Figure 5.4). This may be due to the fact that the reconstructed model tend to be more smooth than the actual Marmousi baseline model. For the time-lapse effect of 100 m/s in the reconstructed model, both the noiseless inversion and the intermediate noise of SNR = 30 dB (Figure 5.19a and 5.19b) accomplish a fairly accurate MAP estimate, of the actual time-lapse change. The inversion of high noise level data in the reconstructed model (see Figure 5.19c), has a very high error compared to the actual time-lapse effect of 100 m/s. However, some structure of the time-lapse effect is still visible. Thus, it does contain valuable time-lapse information, even though the data contained a considerable amount of noise.

(a) *Actual baseline model*

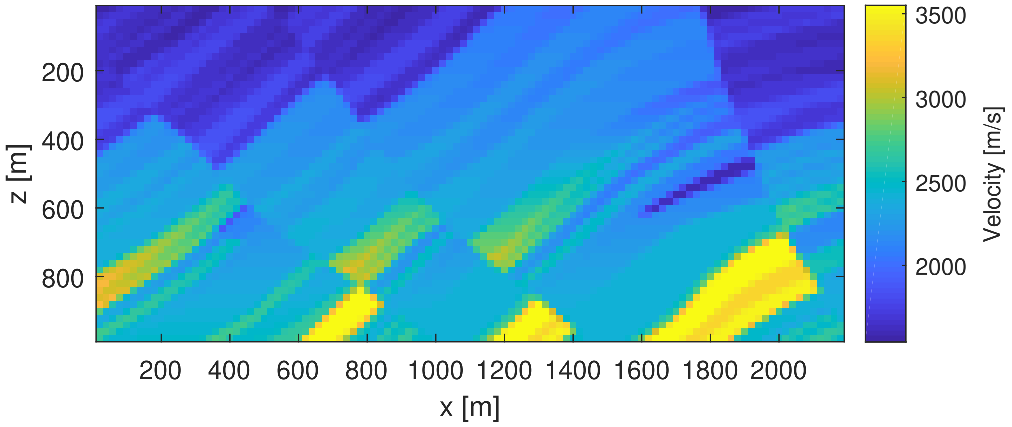

(b) *Actual time-lapse*

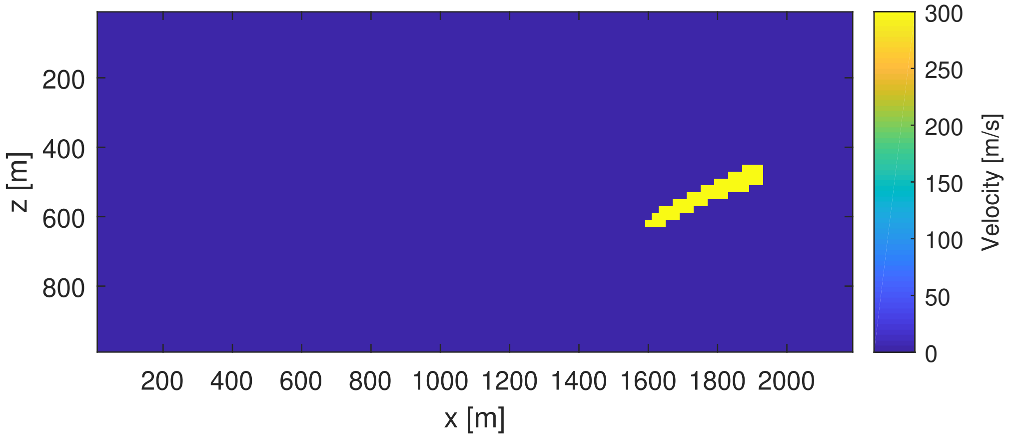

(c) *Prior standard deviation*

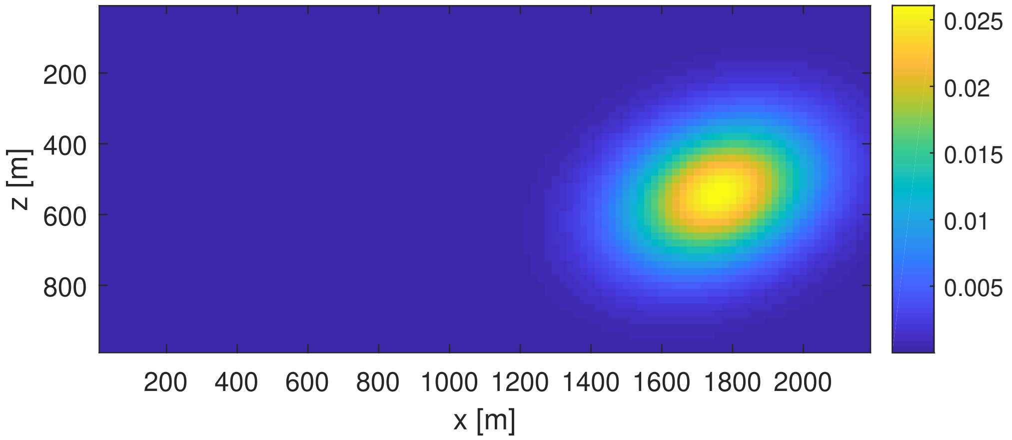

Figure 5.1: *The upper figure 5.1a shows the actual baseline Marmousi model, the middle figure 5.1b is the real time-lapse effect of 300 m/s and the lowermost figure 5.1c is the prior standard deviation.*

(a) *SNR = 100 dB*

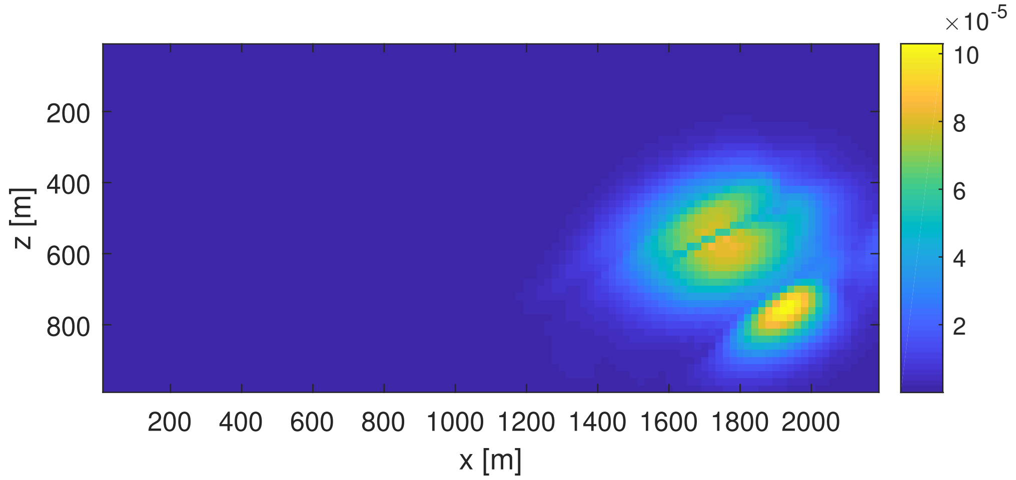

(b) *SNR = 30 dB*

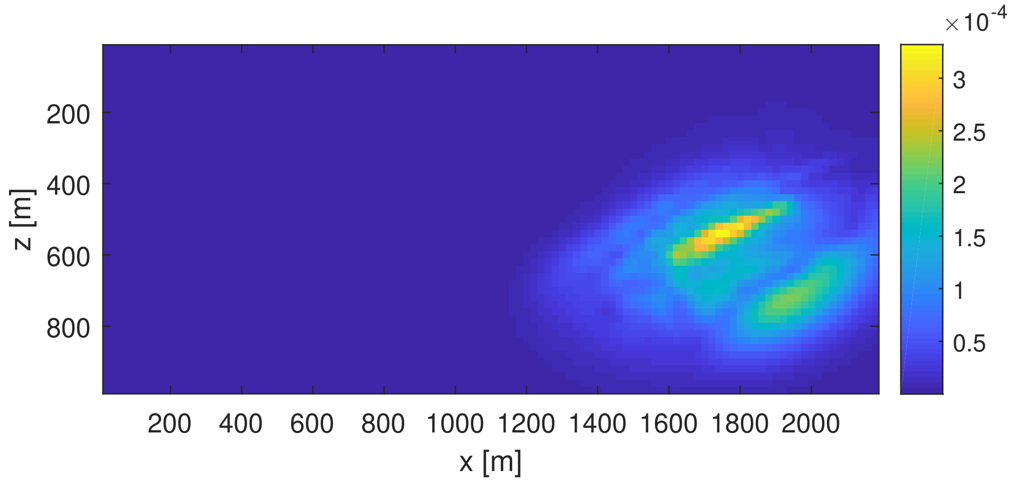

(c) *SNR = 4 dB*

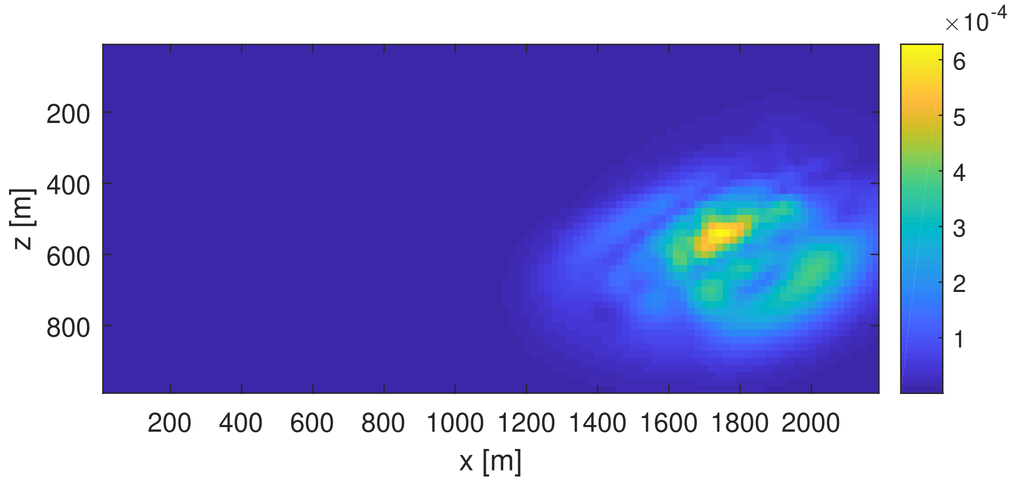

Figure 5.2: *Posterior standard deviations with different noise levels, from the inversion using the actual Marmousi model and the large time-lapse effect of 300 m/s.*

(a) *SNR = 100 dB*

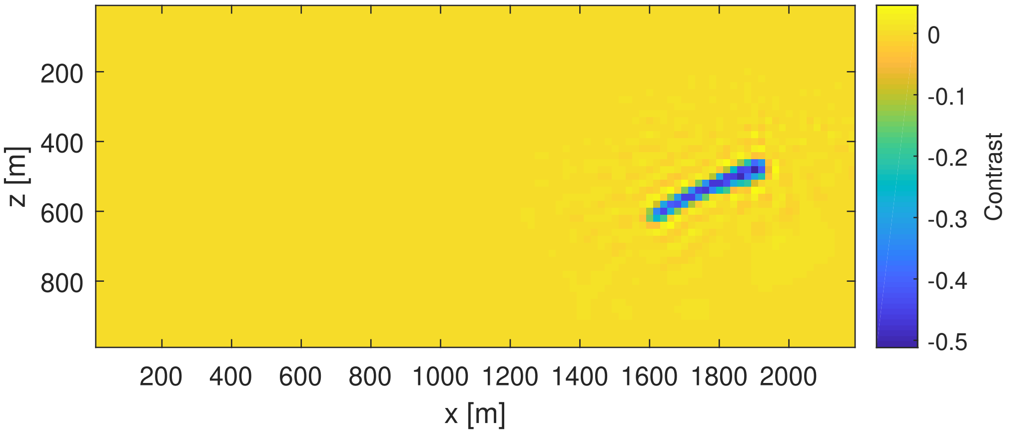

(b) *SNR = 30 dB*

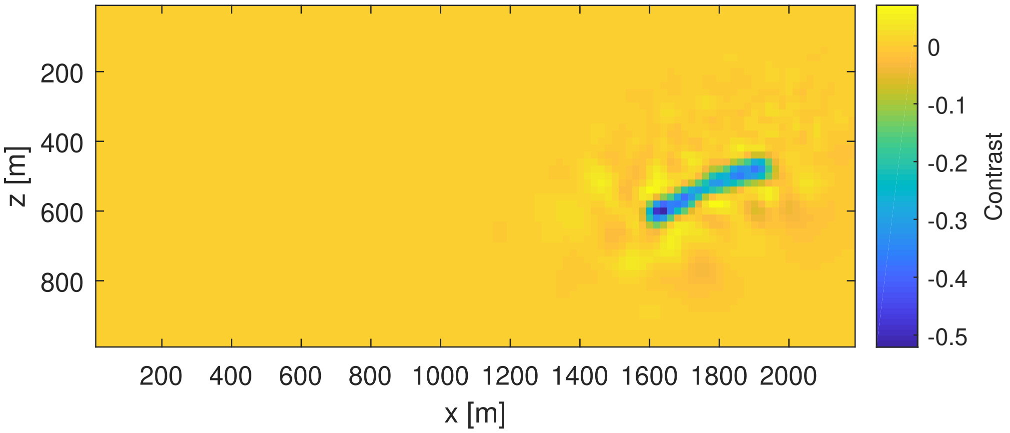

(c) *SNR = 4 dB*

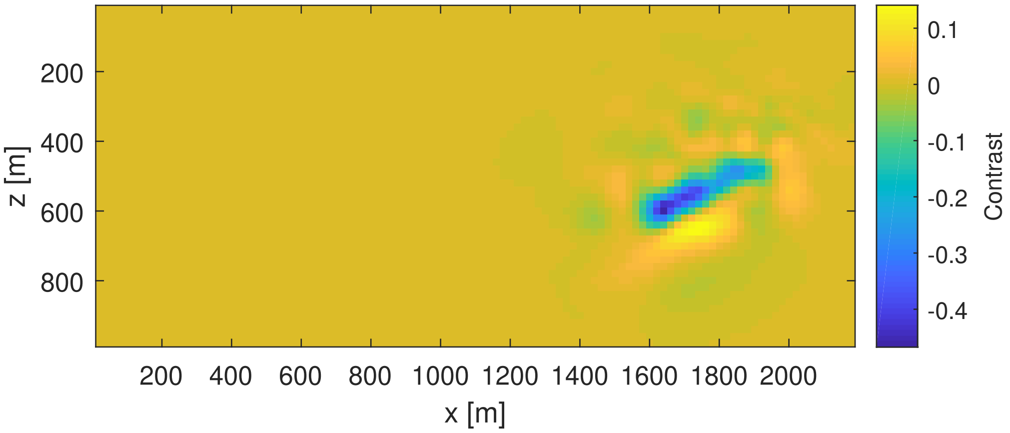

Figure 5.3: *MAP contrast solutions with different noise levels, from the inversion using the actual Marmousi model and the large time-lapse effect of 300 m/s.*

(a) *SNR = 100 dB*

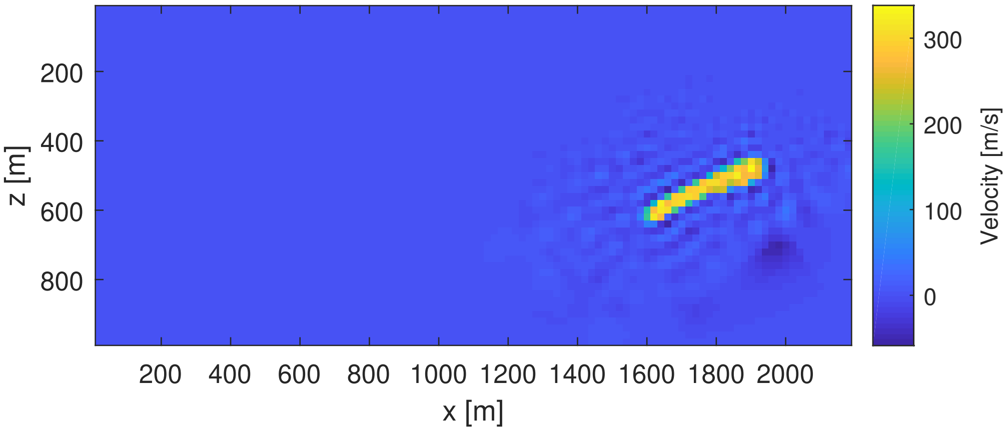

(b) *SNR = 30 dB*

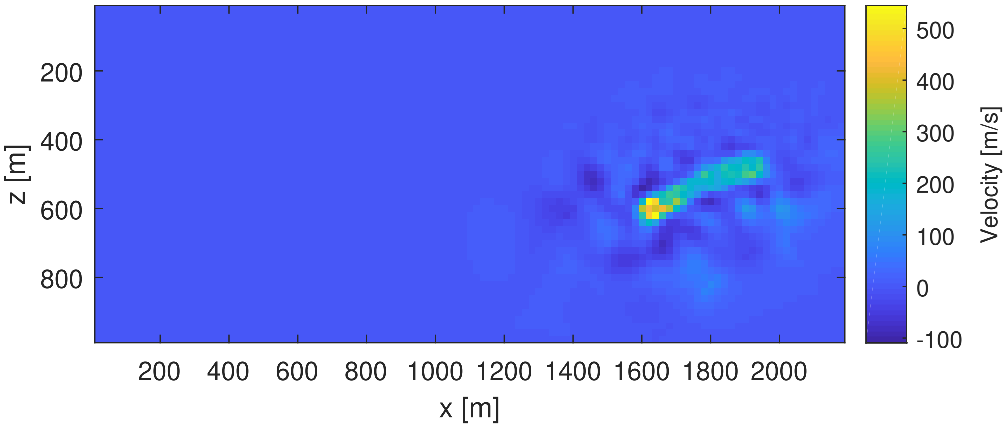

(c) *SNR = 4 dB*

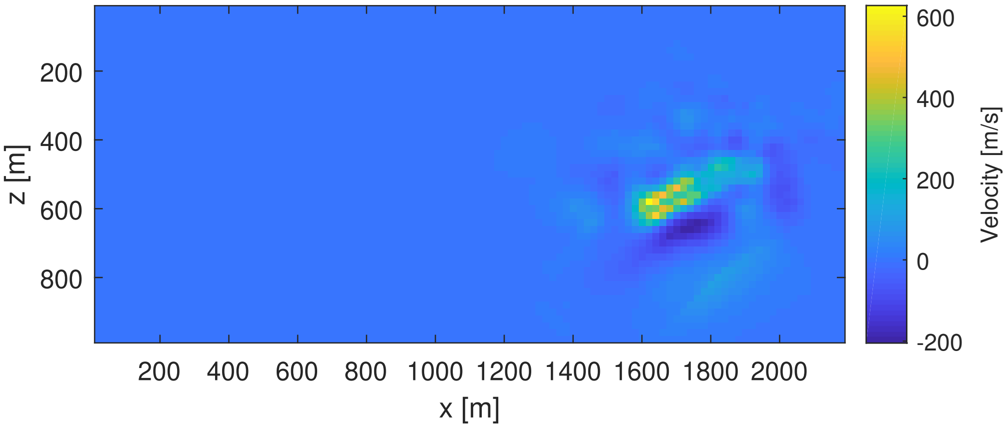

Figure 5.4: *MAP velocity solutions with different noise levels, from the inversion using the actual Marmousi model and the large time-lapse effect of 300 m/s.*

(a) *Error in velocity SNR = 100 dB*

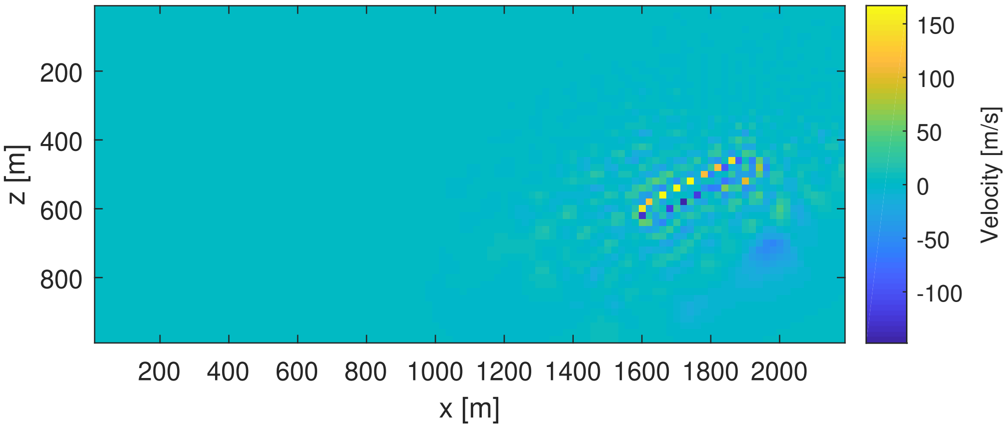

(b) *Error in velocity SNR = 30 dB*

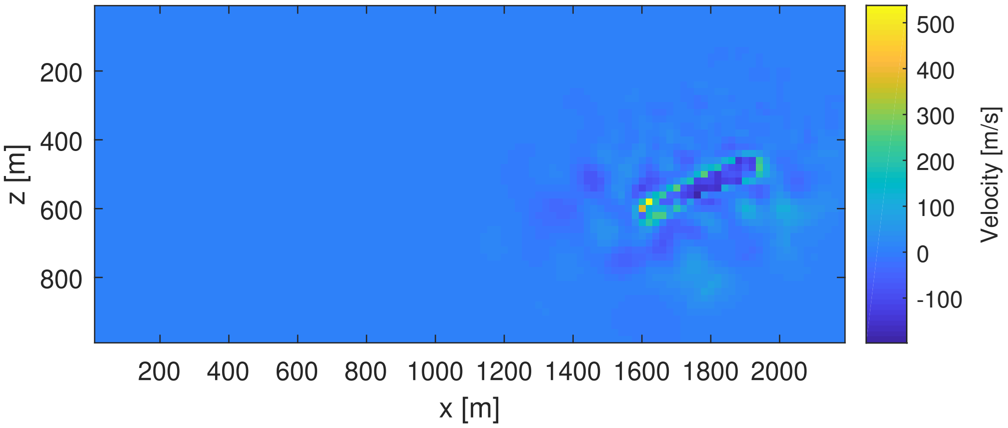

(c) *Error in velocity SNR = 4 dB*

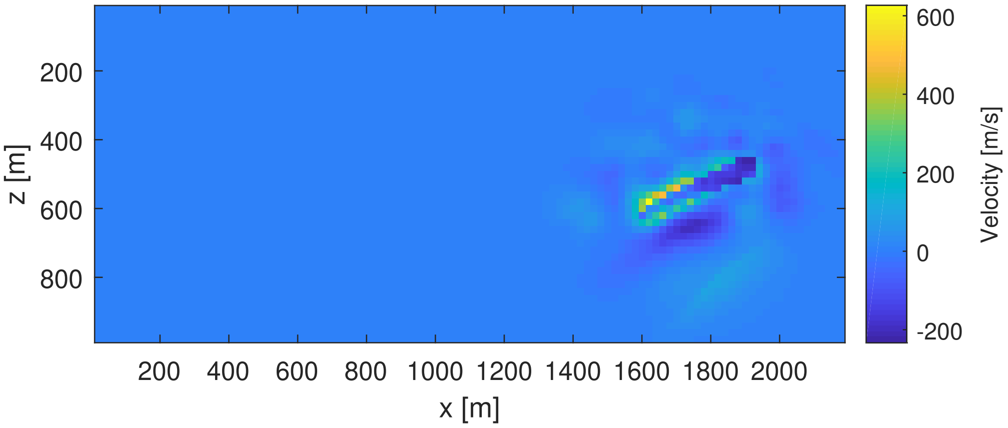

Figure 5.5: *The error in MAP velocity solutions with different noise levels, from the inversion using the actual Marmousi model and the large time-lapse effect of 300 m/s.*

(a) *Actual baseline model*

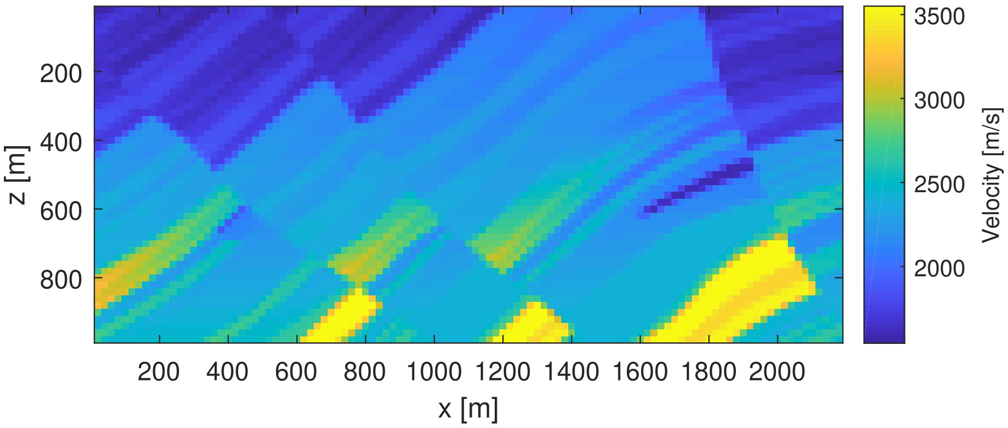

(b) *Actual time-lapse*

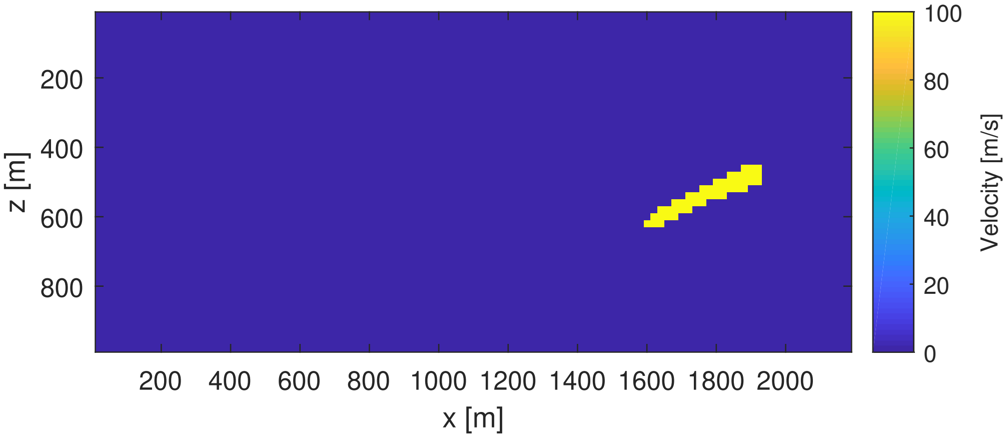

(c) *Prior standard deviation*

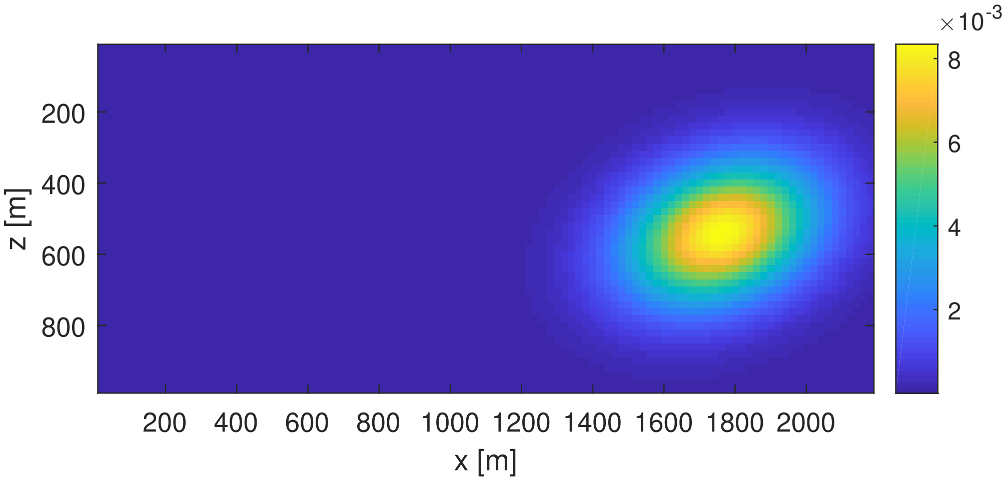

Figure 5.6: *The upper figure 5.6a shows the actual baseline Marmousi model, the middle figure 5.6b is the real time-lapse effect of 100 m/s and the lowermost figure 5.6c is the prior standard deviation.*

(a) *SNR = 100 dB*

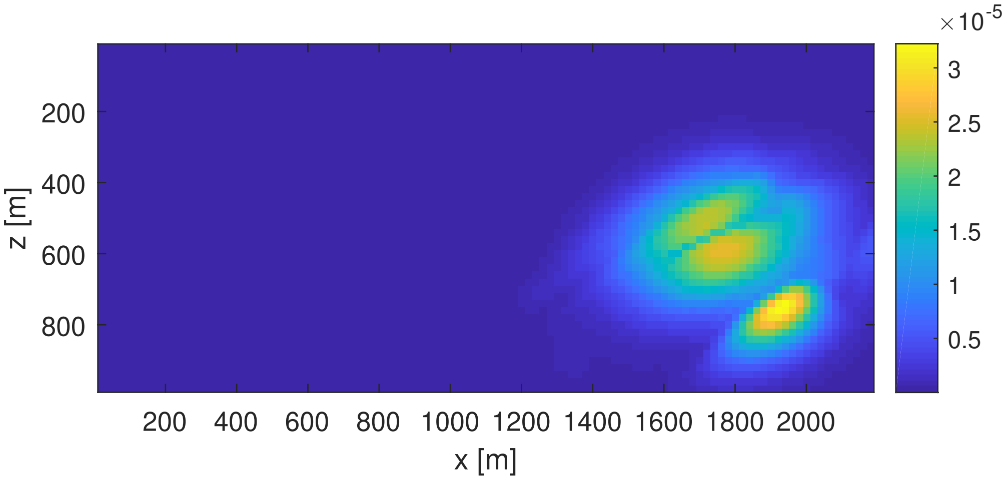

(b) *SNR = 30 dB*

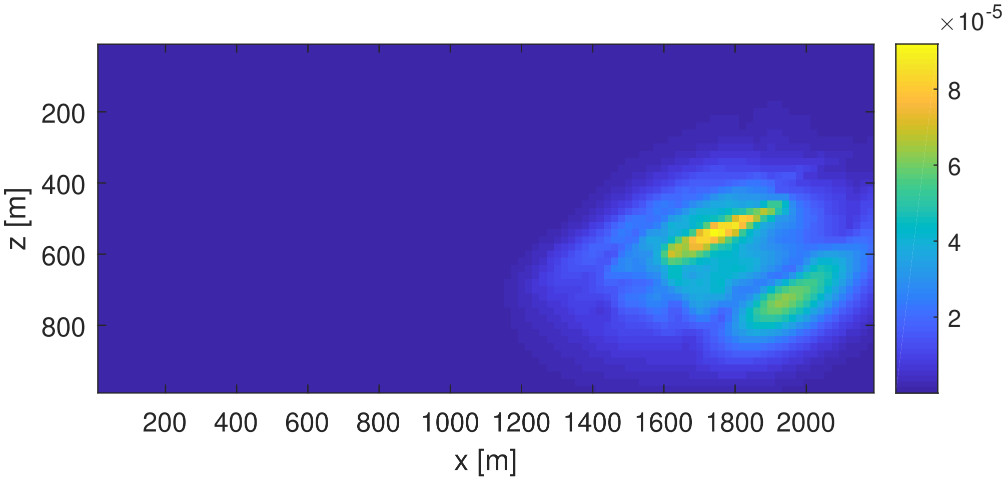

(c) *SNR = 4 dB*

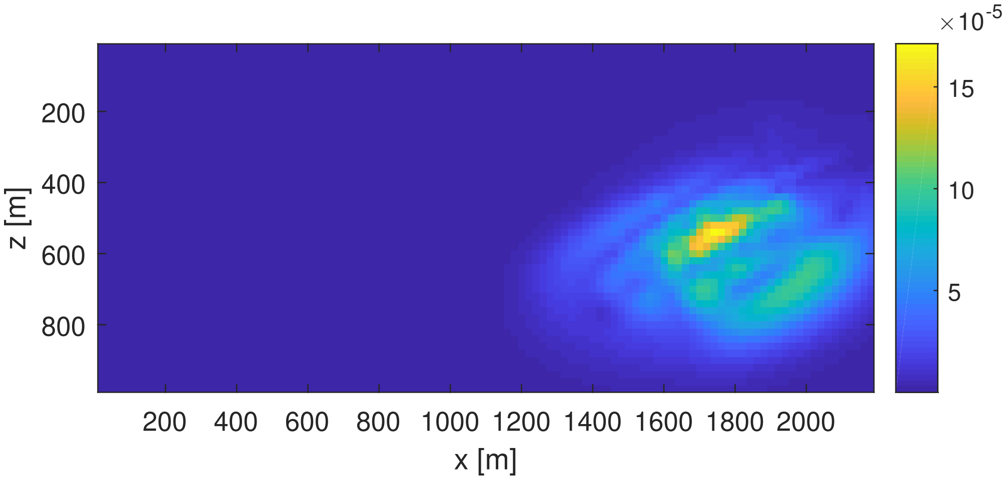

Figure 5.7: *Posterior standard deviations with different noise levels, from the inversion using the actual Marmousi model and the small time-lapse effect of 100 m/s.*

(a) *SNR = 100 dB*

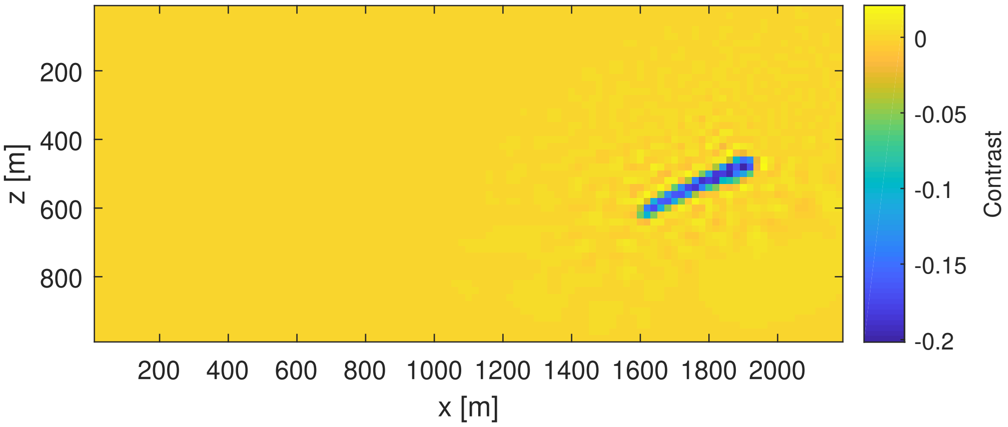

(b) *SNR = 30 dB*

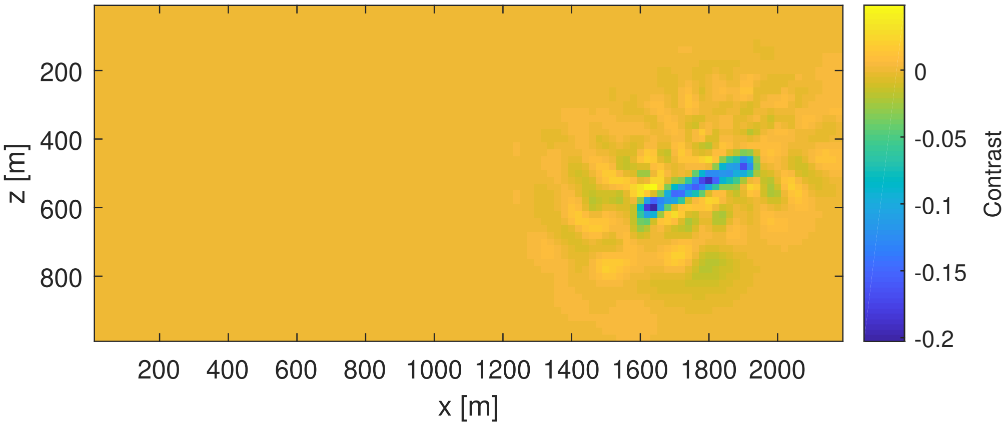

(c) *SNR = 4 dB*

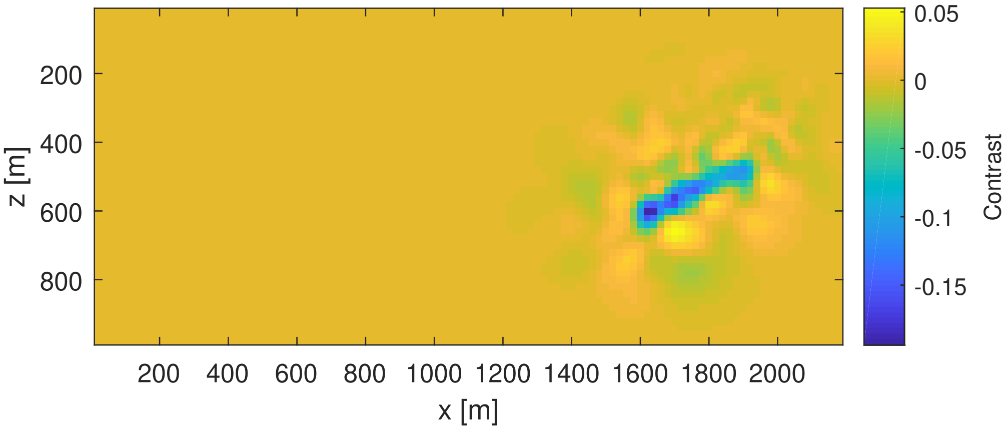

Figure 5.8: *MAP contrast solutions with different noise levels, from the inversion using the actual Marmousi model and the small time-lapse effect of 100 m/s.*

(a) *SNR = 100 dB*

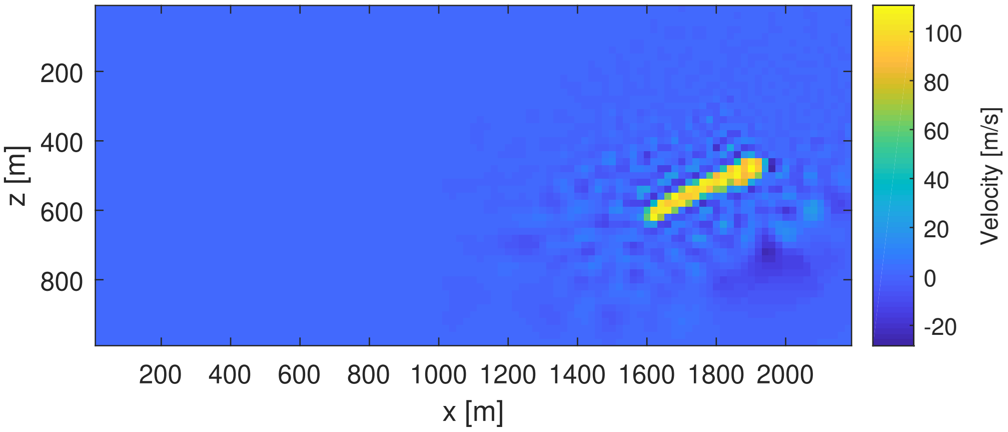

(b) *SNR = 30 dB*

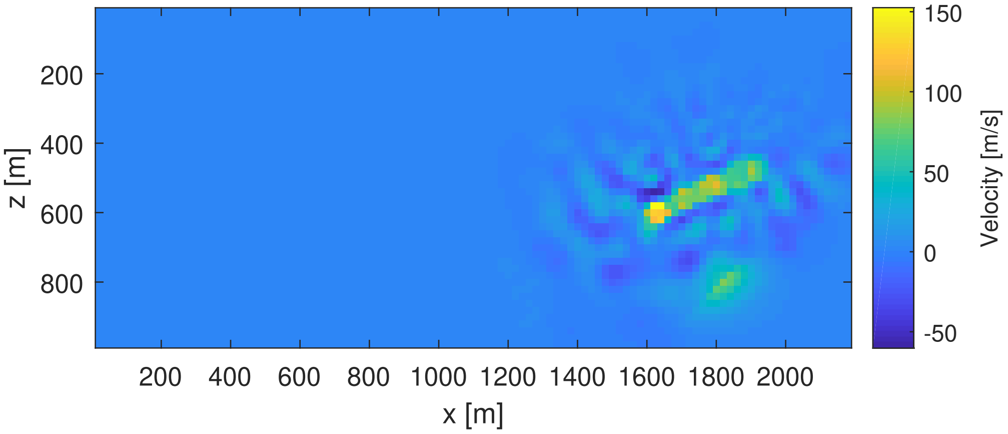

(c) *SNR = 4 dB*

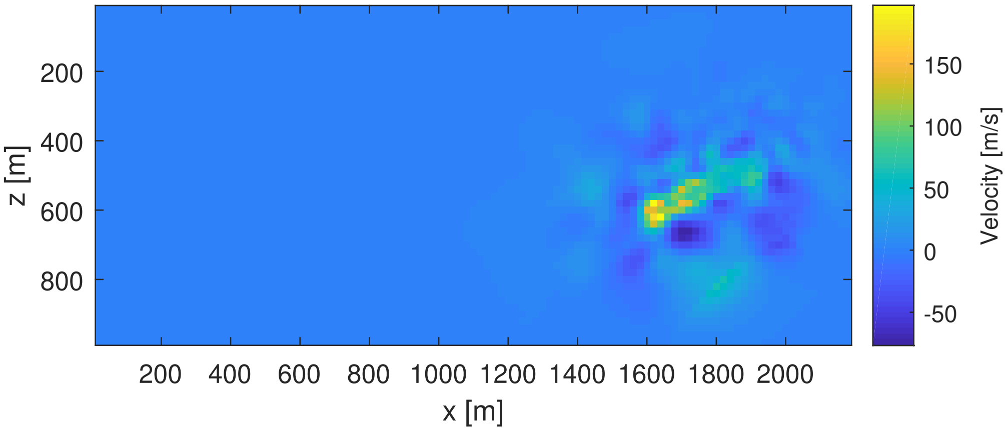

Figure 5.9: *MAP velocity solutions with different noise levels, from the inversion using the actual Marmousi model and the small time-lapse effect of 100 m/s.*

(a) *Error in velocity SNR = 100 dB*

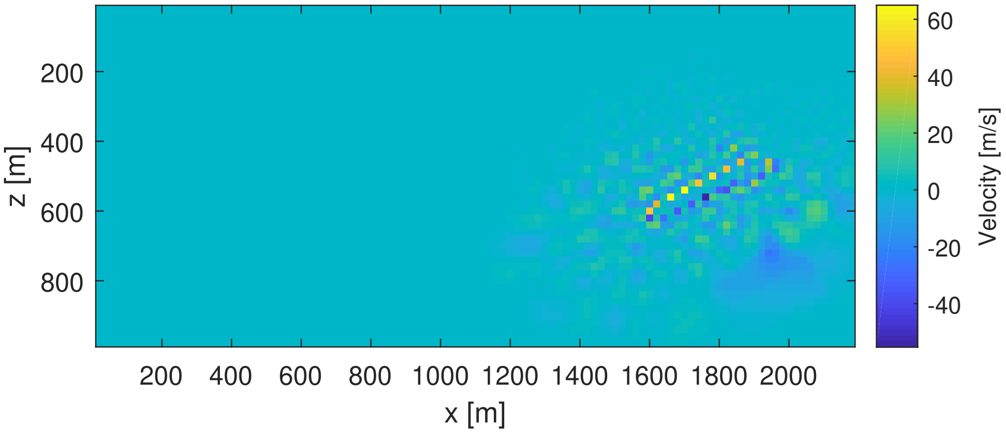

(b) *Error in velocity SNR = 30 dB*

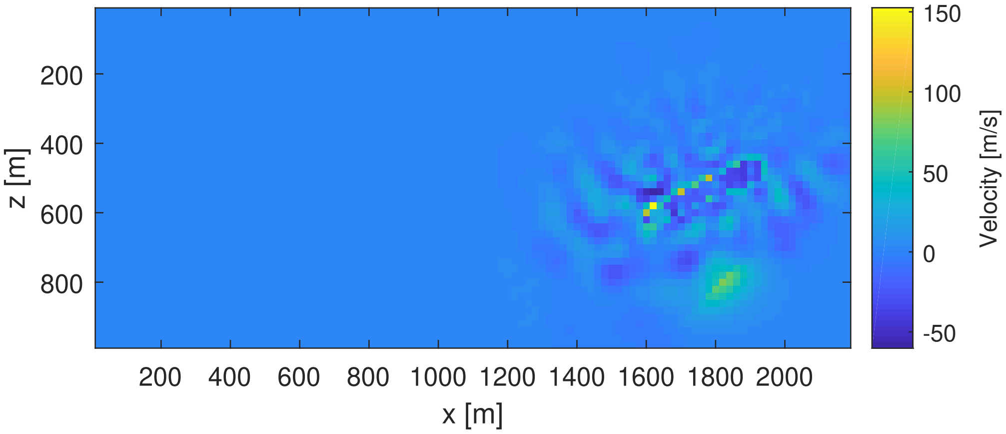

(c) *Error in velocity SNR = 4 dB*

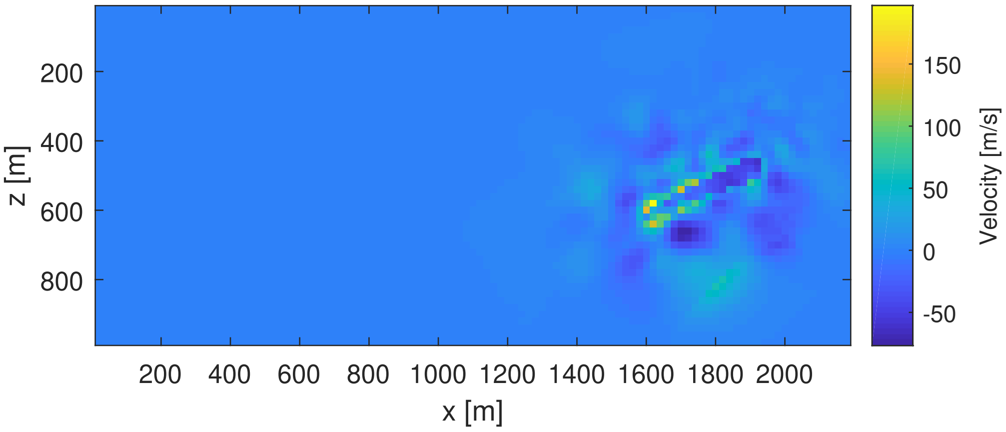

Figure 5.10: *The error in MAP velocity solutions with different noise levels, from the inversion using the actual Marmousi model and the small time-lapse effect of 100 m/s.*

(a) *Baseline model*

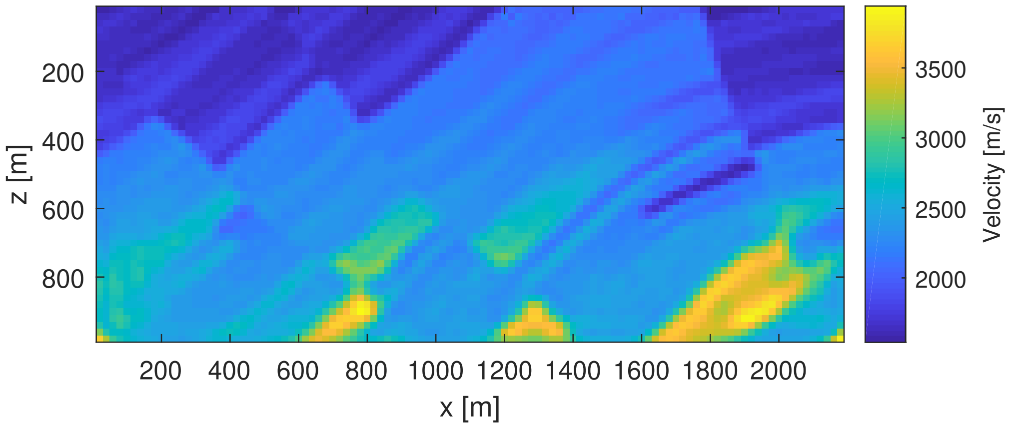

(b) *Actual time-lapse*

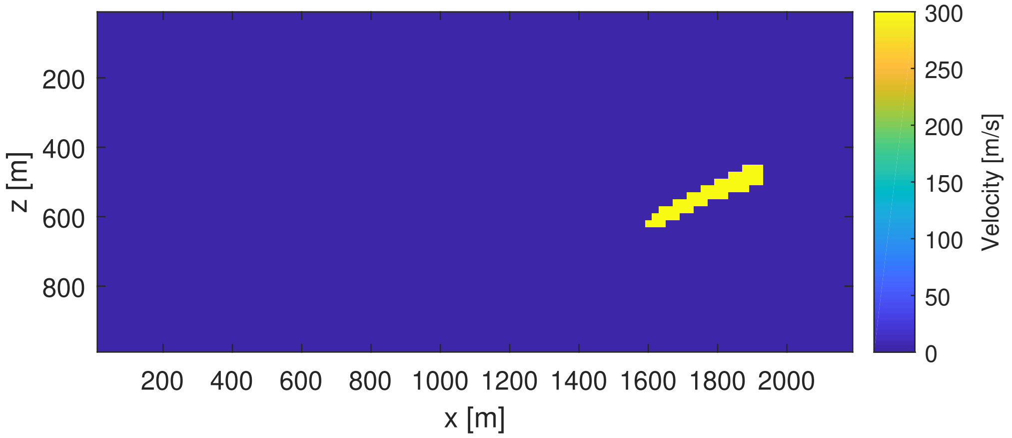

(c) *Prior standard deviation*

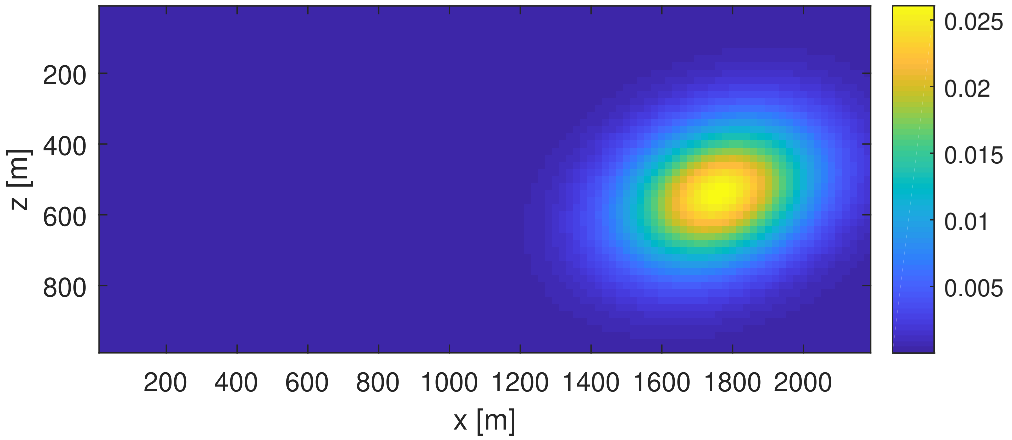

Figure 5.11: *The upper figure 5.11a shows the reconstructed baseline Marmousi model, the middle figure 5.11b is the real time-lapse effect of 300 m/s and the lowermost figure 5.11c is the prior standard deviation.*

(a) *SNR = 100 dB*

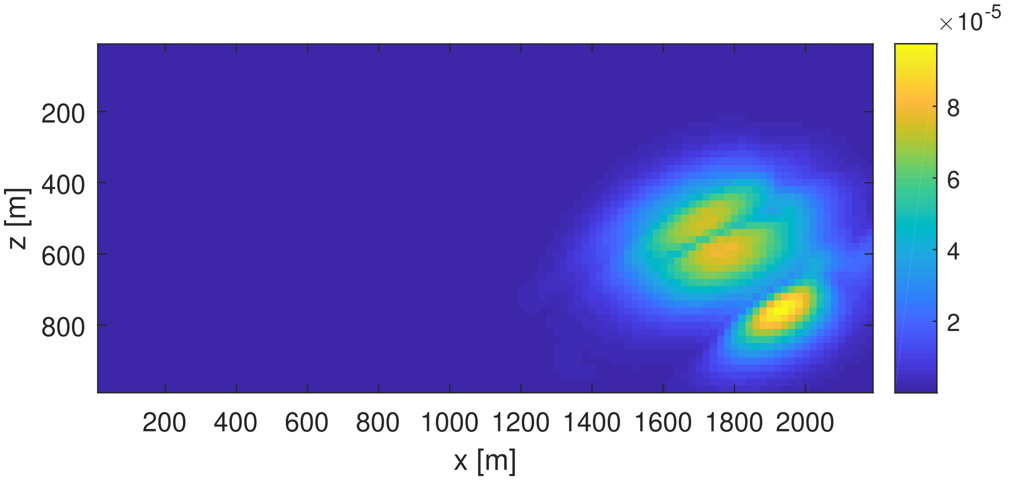

(b) *SNR = 30 dB*

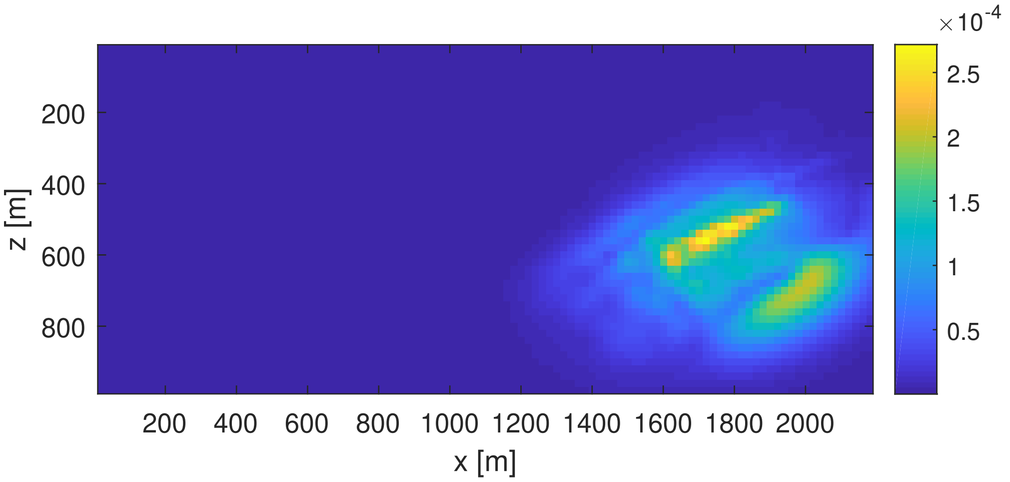

(c) *SNR = 4 dB*

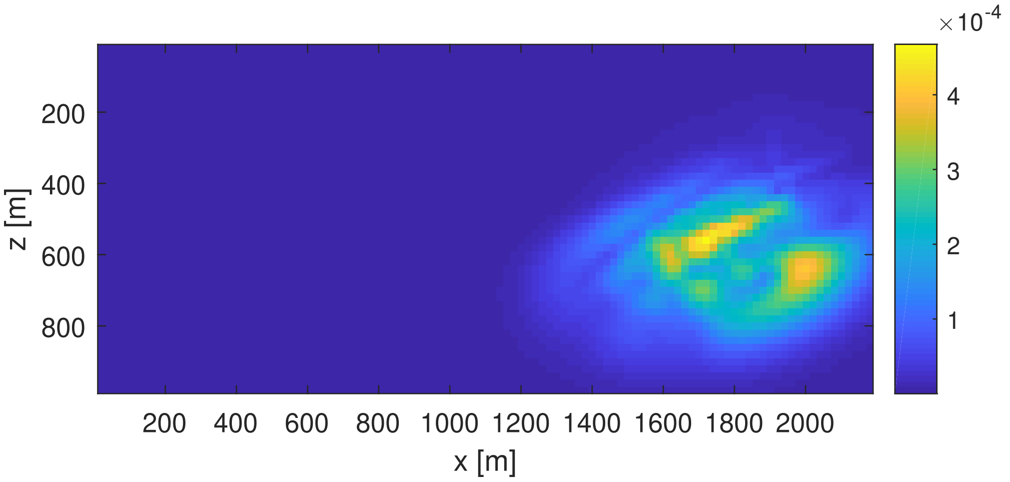

Figure 5.12: *Posterior standard deviations with different noise levels, from the inversion using the reconstructed Marmousi model and the large time-lapse effect of 300 m/s.*

(a) *SNR = 100 dB*

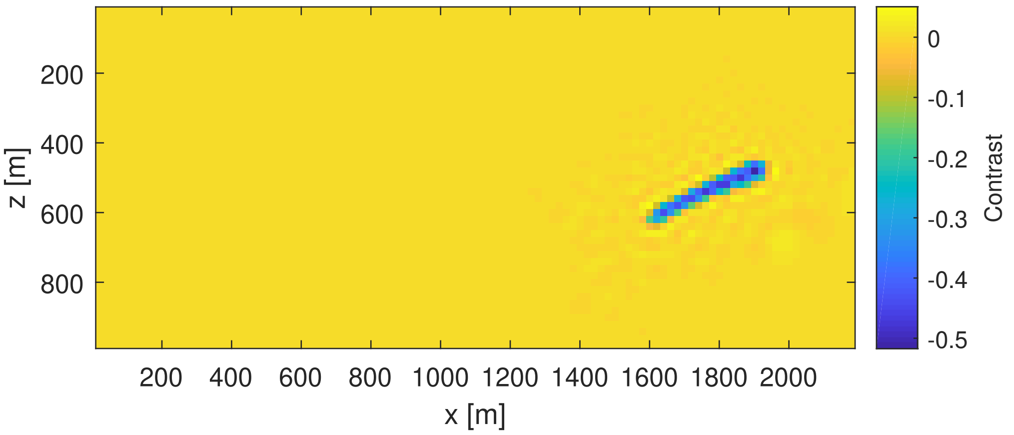

(b) *SNR = 30 dB*

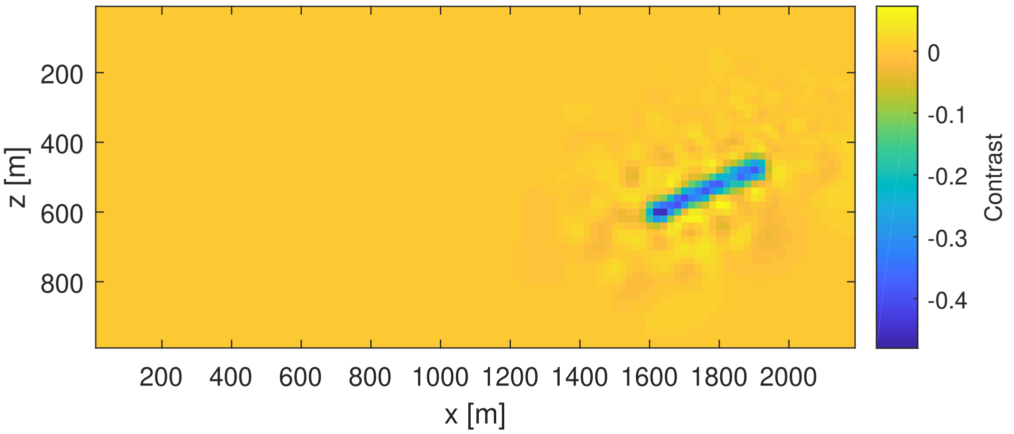

(c) *SNR = 4 dB*

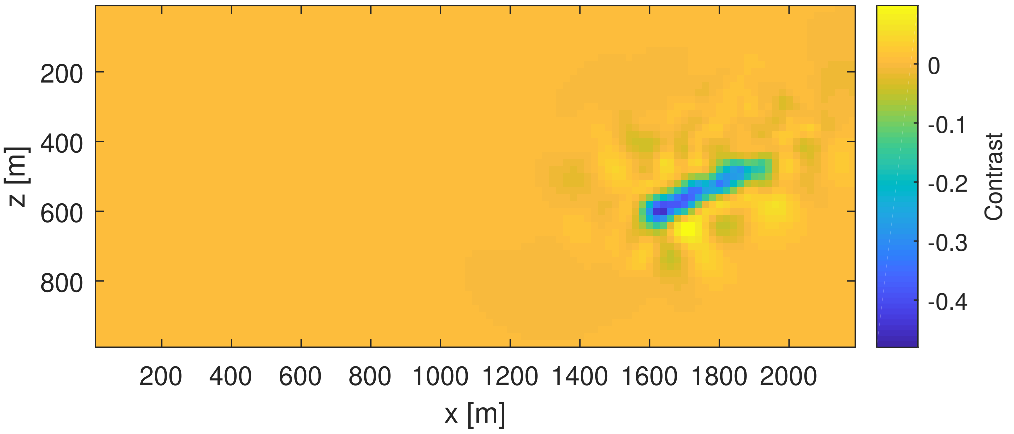

Figure 5.13: *MAP contrast solutions with different noise levels, from the inversion using the reconstructed Marmousi model and the large time-lapse effect of 300 m/s.*

(a) *SNR = 100 dB*

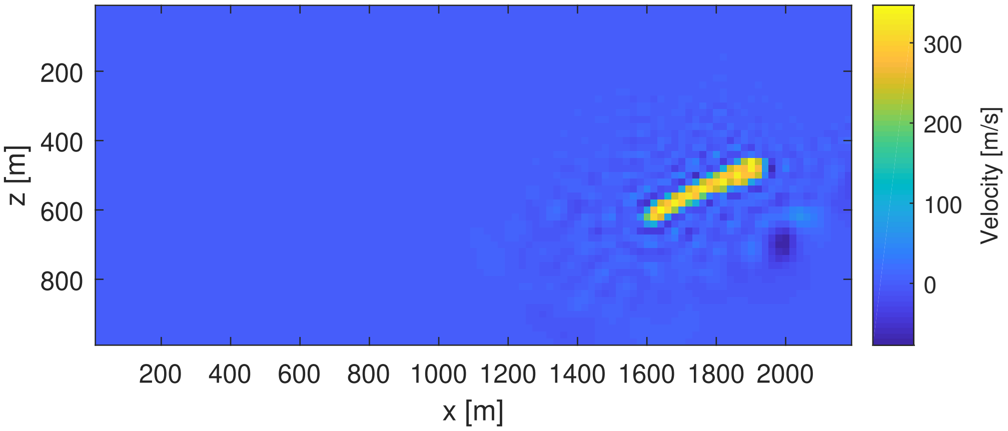

(b) *SNR = 30 dB*

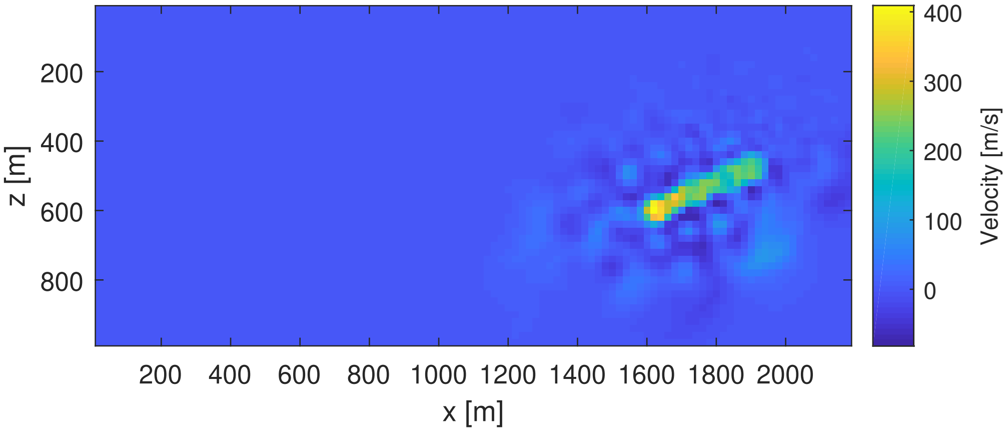

(c) *SNR = 4 dB*

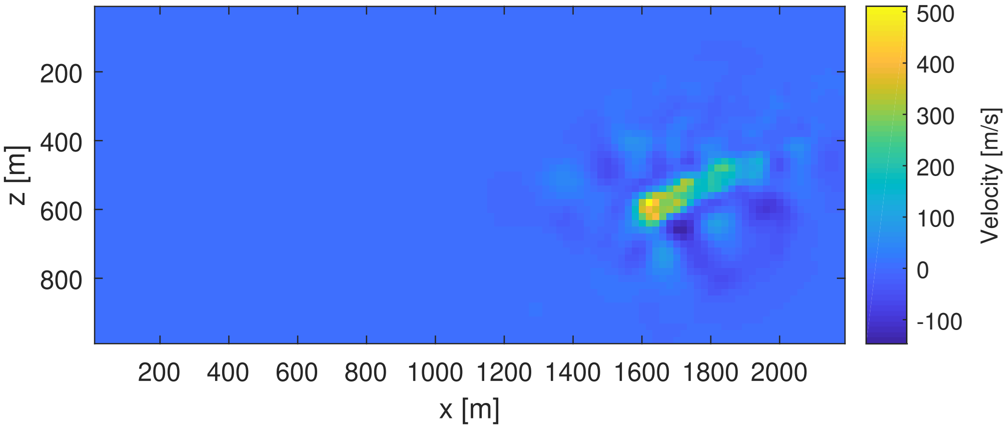

Figure 5.14: *MAP velocity solutions with different noise levels, from the inversion using the reconstructed Marmousi model and the large time-lapse effect of 300 m/s.*

(a) *Error in velocity SNR = 100 dB*

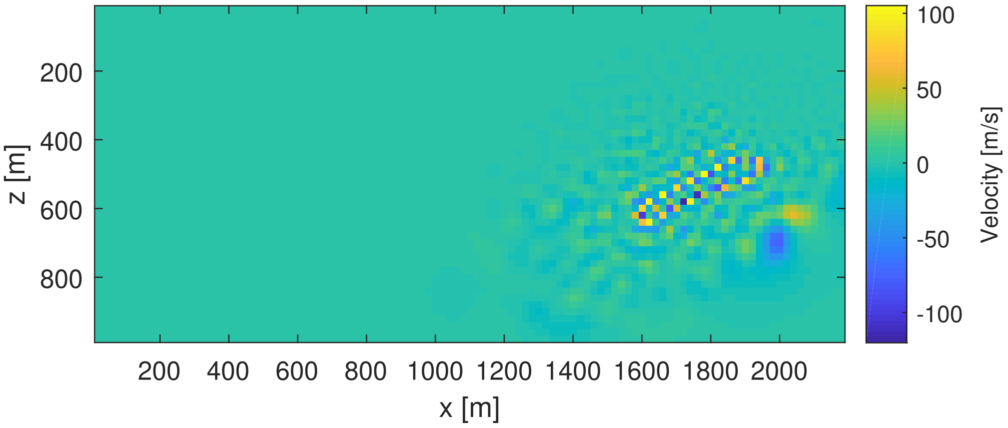

(b) *Error in velocity SNR = 30 dB*

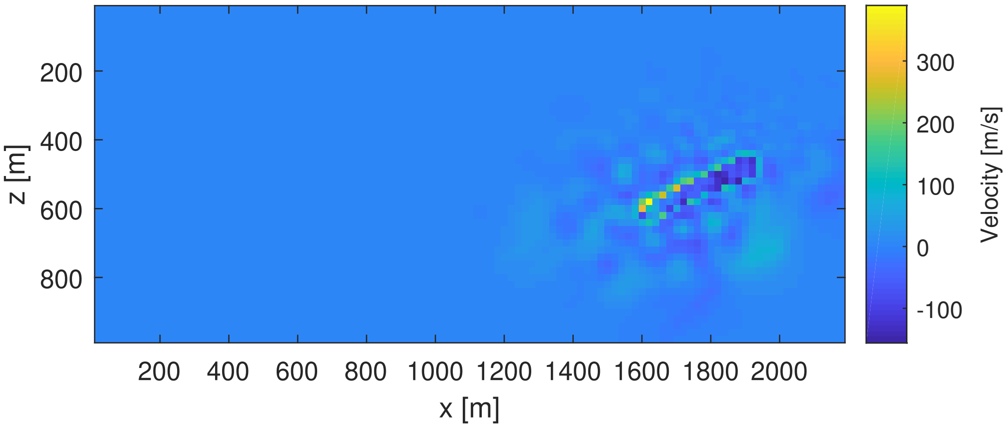

(c) *Error in velocity SNR = 4 dB*

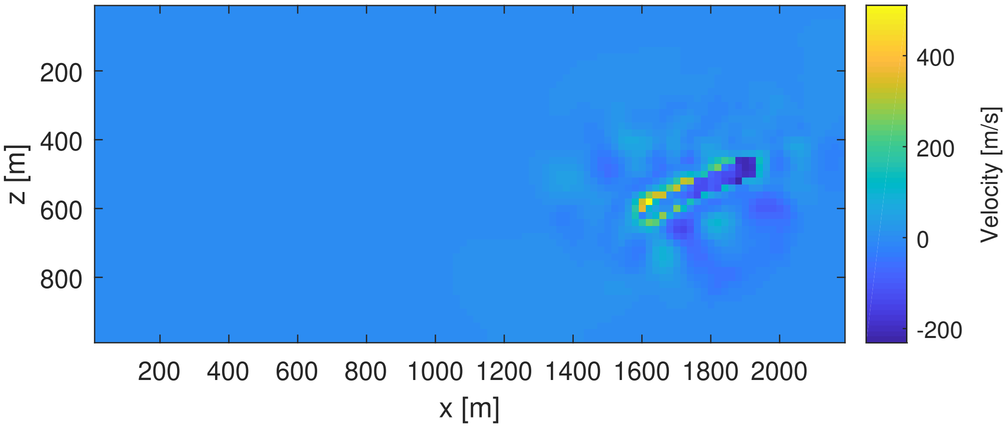

Figure 5.15: *The error in MAP velocity solutions with different noise levels, from the inversion using the reconstructed Marmousi model and the large time-lapse effect of 300 m/s.*

(a) *Baseline model*

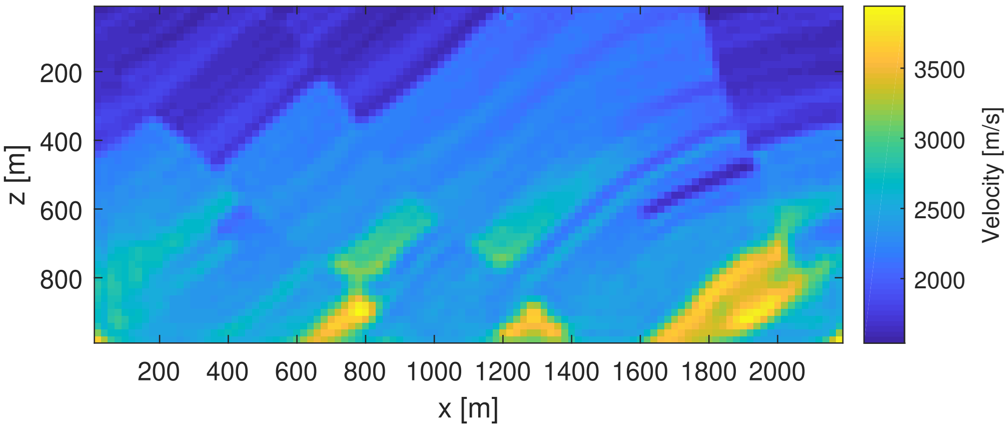

(b) *Actual time-lapse*

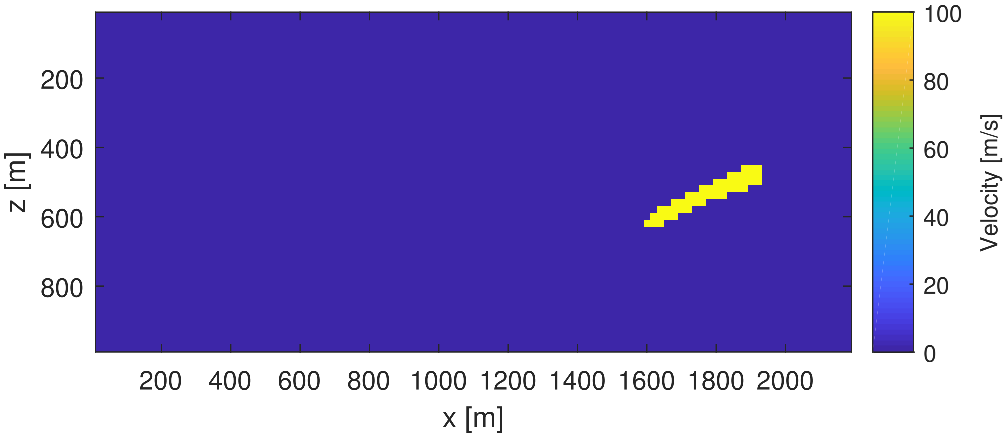

(c) *Prior standard deviation*

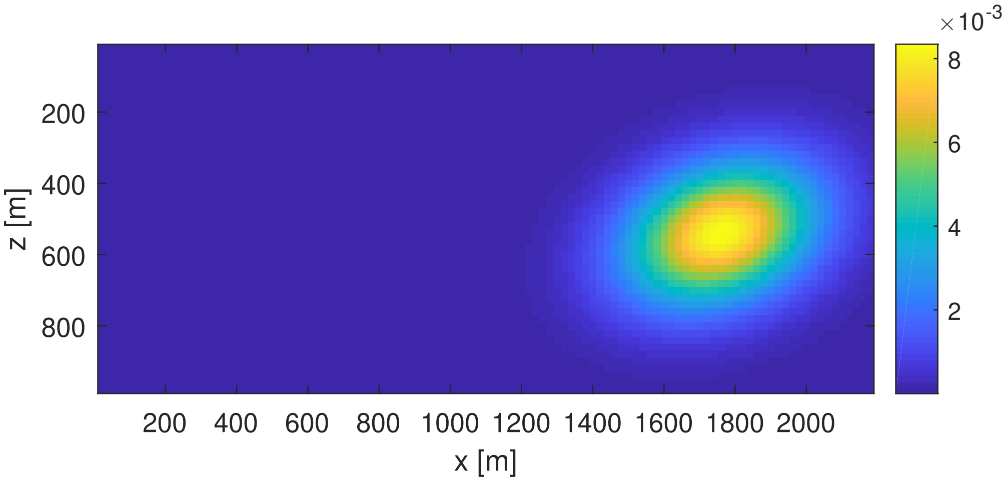

Figure 5.16: *The upper figure 5.16a shows the reconstructed baseline Marmousi model, the middle figure 5.16b is the real time-lapse effect of 100 m/s and the lowermost figure 5.16c is the prior standard deviation.*

(a) *SNR = 100 dB*

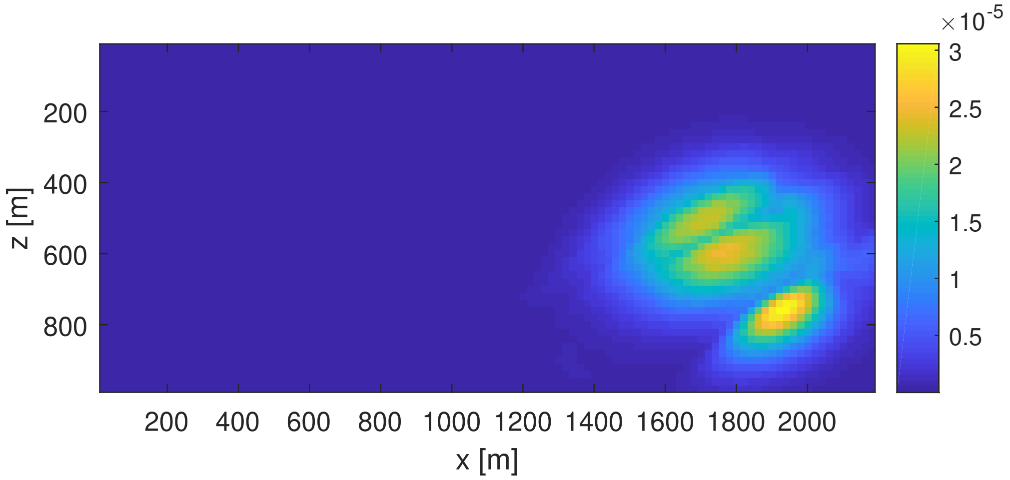

(b) *SNR = 30 dB*

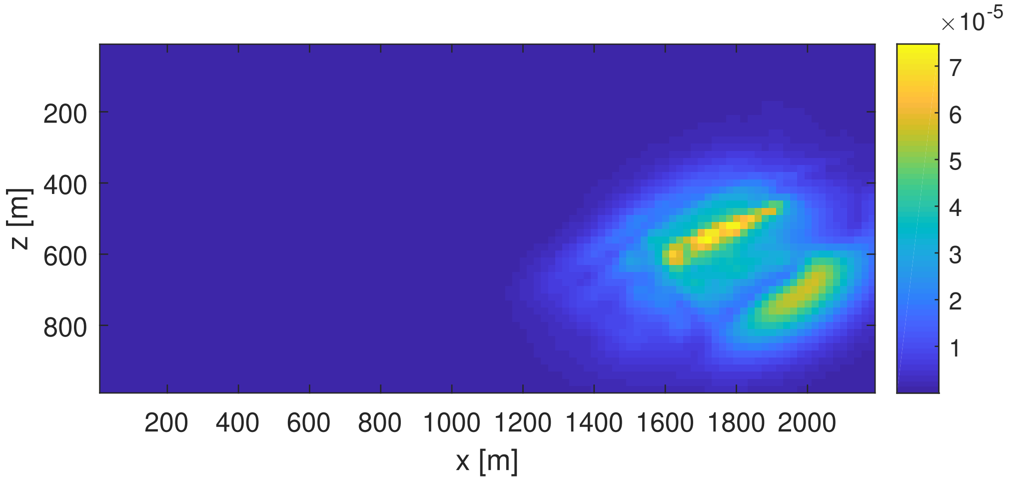

(c) *SNR = 4 dB*

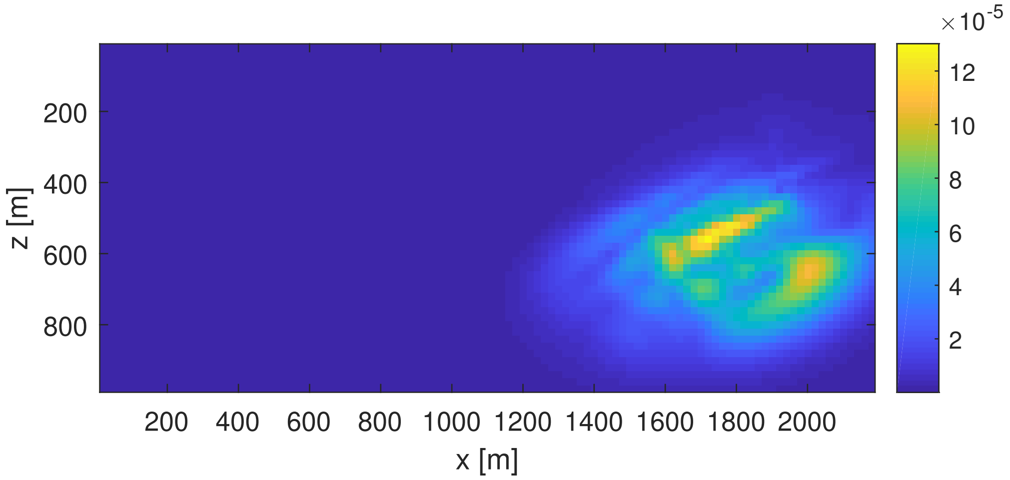

Figure 5.17: *Posterior standard deviations with different noise levels, from the inversion using the reconstructed Marmousi model and the small time-lapse effect of 100 m/s.*

(a) *SNR = 100 dB*

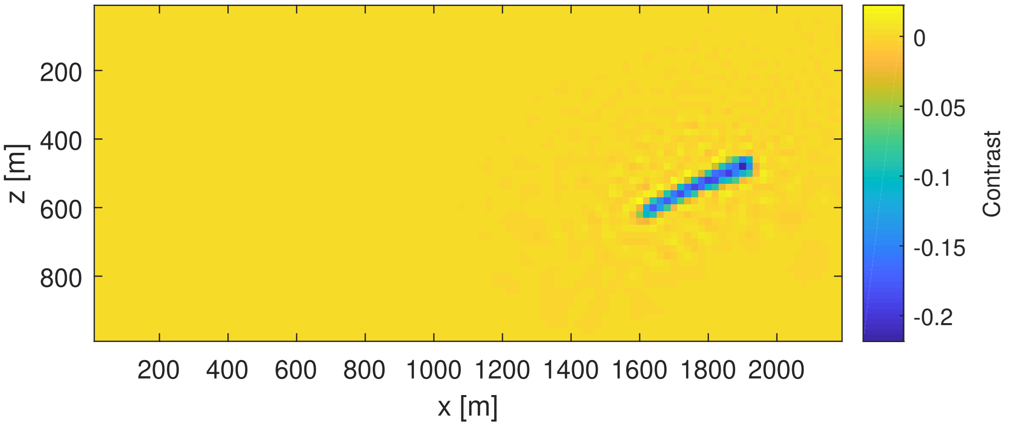

(b) *SNR = 30 dB*

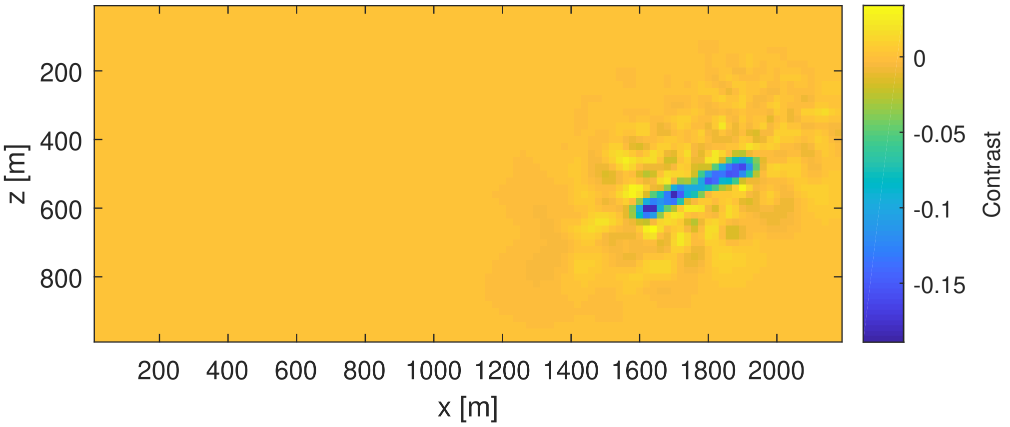

(c) *SNR = 4 dB*

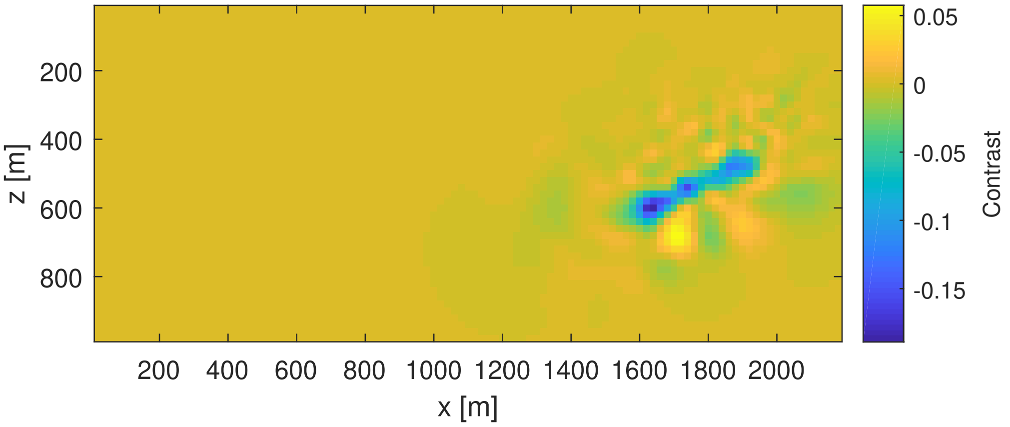

Figure 5.18: *MAP contrast solutions with different noise levels, from the inversion using the reconstructed Marmousi model and the small time-lapse effect of 100 m/s.*

(a) *SNR = 100 dB*

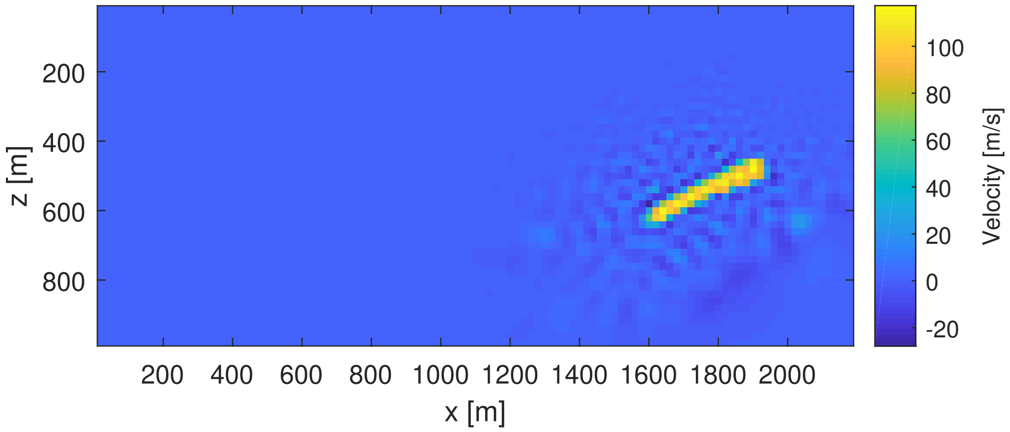

(b) *SNR = 30 dB*

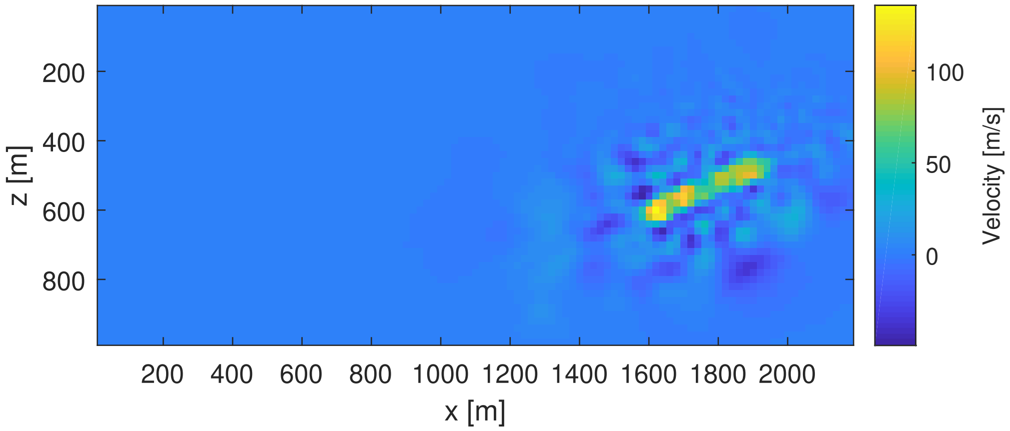

(c) *SNR = 4 dB*

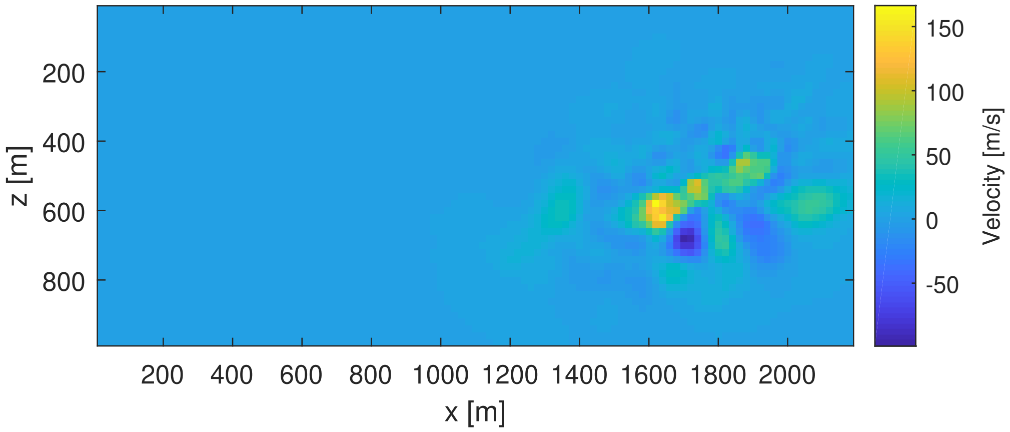

Figure 5.19: *MAP velocity solutions with different noise levels, from the inversion using the reconstructed Marmousi model and the small time-lapse effect of 100 m/s.*

(a) *Error in velocity SNR = 100 dB*

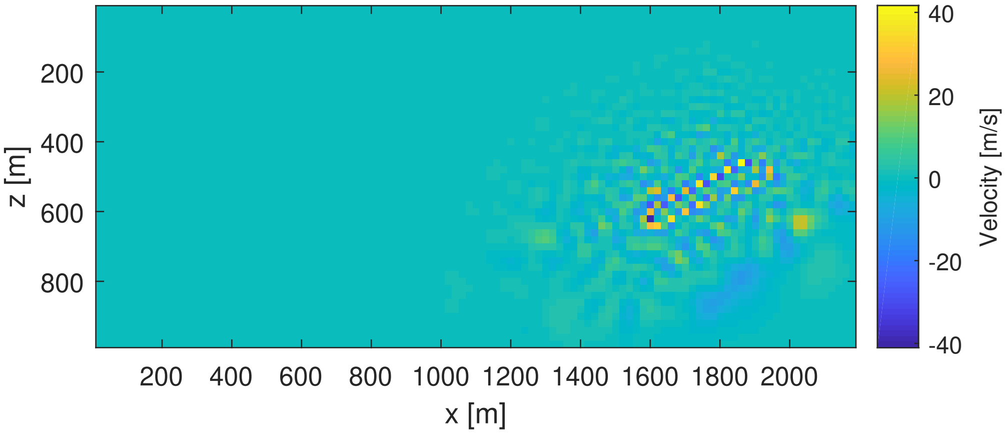

(b) *Error in velocity SNR = 30 dB*

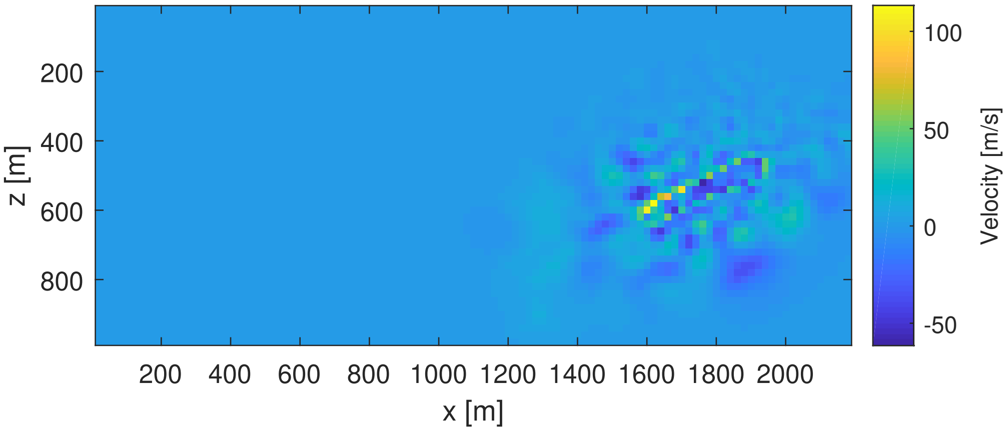

(c) *Error in velocity SNR = 4 dB*

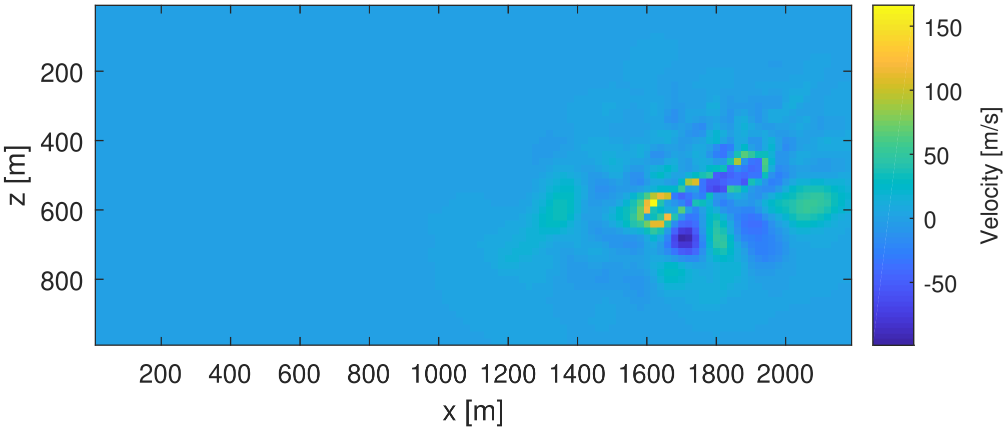

Figure 5.20: *The error in MAP velocity solutions with different noise levels, from the inversion using the reconstructed Marmousi model and the small time-lapse effect of 100 m/s.*

Chapter 6

Concluding remarks

6.1 Conclusions

The aim of this thesis has been to study seismic waveform modelling using integral equation methods. This has been applied to both forward and inverse time-lapse seismic problems. In Chapter 2.7 and 2.8, it was shown that it is important to be aware of the limitations of the Born approximation. Poor estimations of the seismic wave-field may be obtained, especially when used with a background medium inadequate of representing the actual model.

The distorted Born approximation was used to obtain a linear relation between the scattered time-lapse data, and the contrast function. This made it possible to use explicit expressions to calculate the MAP solutions of the contrast function and their corresponding covariance matrix that was illustrated as standard deviations in this thesis. This proves that the Born approximation, used with an appropriate (inhomogeneous) background medium still can be proven to be very useful, especially in the application of time-lapse seismic problems. The linear Bayesian time-lapse inversion performs efficiently in the sense that it does not need to iterate, as in the case of many non-linear methods which need to solve a computational demanding forward problem at each iteration. On the other hand, the inversion of a full covariance matrix is specially memory demanding.

Furthermore, the linear Bayesian method that was used, require that a full baseline reconstructed modell is provided. In this thesis, this was provided by the DBIT method, which successfully provided a baseline reconstruction of the Marmousi model. The sequential time-lapse experiment, performed in Chapter 4, illustrated the effect of additional reconstruction of parts in the monitor model, that was not properly resolved in the baseline inversion. Even though the extra parts that was reconstructed in the monitor inversion can be considered as a further convergence to the actual model, it was transformed into artefacts in the time-lapse model that was obtained by the sequential method. The importance of being aware of such errors in the time-lapse data, is essential for making correct interpretations that could be used for updating reservoir models.

6.2 Suggestions for future work

The work presented in this thesis does show potential in many applications. Despite the promising results, there is still plenty of room for further developments. In this section, some suggestions will be provided.

One way of extending the work, is by comparing the time-lapse estimates obtained by the double difference and sequential difference strategies. The second suggestion is speeding up the process of forward modelling, which can be implemented more efficiently by the use of FFT methods on a convergent Born series (see for example Osnabrugge et al., 2016). As an extension of the work done in Chapter 5, it would be interesting to test the same method for data generated by, for instance, finite difference. A similar, but deterministic, experiment was performed by Jakobsen and Ursin (2015), where the DBIT method was tested on synthetic data generated by the method of finite difference. It would be interesting to see how the linear Bayesian distorted Born approximation would perform on a set of real data. Furthermore, the implementation of the DBIT method and linear Byesian time-lapse inversion can be modified to work on models in 3 dimensions (3D). A time-lapse study is suggested with two reservoirs, for instance in the Marmousi model, could be implemented with domain-decomposition using the T-matrix. Another obvious direction would be to perform FWI in elastic media using integral equation methods. Further development could also be considered in target oriented time-lapse FWI in a Bayesian framework. Also worth mentioning is the study of integration of time-lapse seismic waveform inversion results with updating of a reservoir model, i.e. history matching. Enesmble based history matching could be applied conveniently if a Bayesian formulation of the seismic time-lapse problem was to be used.

6.3 Summary

In this thesis, investigations on the matter of seismic inverse problems by use off a non-linear deterministic method and a linear Bayesian method was implemented in the essential application of time-lapse seismic studies. First, the thesis presented a way of performing seismic forward modelling using integral equation methods. Next, general theory of linear inverse problems were covered. These methods were then applied to seismic inverse problems. It has been demonstrated that both the non-linear deterministic DBIT method and the linear Bayesian approach were fully capable of solving time-lapse seismic inverse problems contaminated with different amount of noise.

References

Asnaashari, A., R. Brossier, S. Garambois, F. Audebert, P. Thore, and J. Virieux (2015). Time-lapse seismic imaging using regularized full-waveform inversion with a prior model: Which strategy? *Geophysical Prospecting 63*(1), 78–98.

Aster, R. C., B. Borchers, and C. H. Thurber (2013). *Parameter Estimation and Inverse Problems* (2nd ed. ed.). Waltham,MA: Academic Press.

Auld, B. A. (1973). *Acoustic fields and waves in solids*, Volume 1. New York: Wiley.

Cerveny, V. (2001). *Seismic Ray Theory.* New York: Cambridge University Press.

Chew, W. C. and Y. M. Wang (1990). Reconstruction of Two-Dimensional Permittivity Distribution Using the Distorted Born Iterative Method. *IEEE Transactions on Medical Imaging 9*(2), 218–225.

Constable, S. C., R. L. Parker, and C. G. Constable (1987). Occam' s inversion: A practical algorithm for generatlng smooth models from electromagnetic sounding data. *52*(5), 289–300.

Denli, H. and L. Huang (2009). Double-difference elastic waveform tomography in the time domain. In *SEG Technical Program Expanded Abstracts 2009*, pp. 2302–2306. Society of Exploration Geophysicists.

Eikrem, K. S., M. Jakobsen, and G. Nævdal (2017). Bayesian Inversion of Time-lapse Seismic Waveform Data Using an Integral Equation Method. In *IOR 2017-19th European Symposium on Improved Oil Recovery.*

Eikrem, K. S., G. Nævdal, and M. Jakobsen (2018). Iterated extended Kalman filter method for time-lapse seismic full waveform inversion. *Geophysical Prospecting, Submitted*.

Eikrem, K. S., G. Nævdal, M. Jakobsen, and Y. Chen (2016). Bayesian estimation of reservoir properties—effects of uncertainty quantification of 4D seismic data. *Computational Geosciences 20*(6), 1211–1229.

Farquharson, C. G. and D. W. Oldenburg (2004). A comparison of automatic techniques for estimating the regularization parameter in non-linear inverse problems. *Geophysical Journal International 156*(3), 411–425.

Guéguen, Y. and V. Palciauskas (1994). *Introduction to the physics of rocks.* Princeton, N.J: Princeton University Press.

Hadamard, J. (1902). Sur les problèmes aux dérivées partielles et leur signification physique. *Princeton Uni. Bull. (1902).*

Hansen, P. C. (1997). *Rank-Deficient and Discrete Ill-Posed Problems.* Society for Industrial and Applied Mathematics.

Huang, X., M. Jakobsen, K. S. Eikrem, and G. Nævdal (2018). Fast repeat-inversion of time-lapse seismic waveform data. *Communications in Computational Physics, Submitted*.

Ikelle, L. T. and L. Amundsen (2005). *Introduction to Petroleum Seismology.* Society of Exploration Geophysicists.

Jakobsen, M. (2012). T-matrix approach to seismic forward modelling in the acoustic approximation. *Studia Geophysica et Geodaetica 56*(1), 1–20.

Jakobsen, M. and B. Ursin (2015). Full waveform inversion in the frequency domain using direct iterative T-matrix methods. *Journal of Geophysics and Engineering 12*(3), 400–418.

Jakobsen, M. and R.-S. Wu (2016). Renormalized scattering series for frequency-domain waveform modelling of strong velocity contrasts. *Geophysical Journal International 206*(2), 880–899.

Jakobsen, M. and R.-S. Wu (2018). Accelerating the T-matrix approach to seismic full-waveform inversion by domain decomposition. *Geophysical Prospecting, Early view, doi: 10.1111/1365-2478.12619*.

Kirchner, A. and S. A. Shapiro (2001). Fast repeat-modelling of time-lapse seismograms. *Geophysical Prospecting 49*(5), 557–569.

Krebes, E. S. (2004). Seismic forward modeling. *CSEG Recorder* (30), 28–39.

Landrø, M. (2001). Discrimination between pressure and fluid saturation changes from time-lapse seismic data. *Geophysics 66*(3), 836–844.

Landrø, M. (2010). 4D Seismic. In *Petroleum Geoscience: From Sedimentary Environments to Rock Physics*, Chapter 19, pp. 427–444.

Levinson, H. W. and V. A. Markel (2016). Solution of the nonlinear inverse scattering problem by T- matrix completion. II. Simulations.

Martin, G. S., R. Wiley, and K. J. Marfurt (2006). Marmousi2: An elastic upgrade for Marmousi. *The Leading Edge 25*(2), 156–166.

Menke, W. (2012). *Geophysical Data Analysis: Discrete Inverse Theory.* Elsevier.

Morse, P. and H. Feshback (1953). *Methods of theoretical physics.* New York: McGraw-Hill.

Moser, T. J. (2012). Review of ray-Born forward modeling for migration and diffraction analysis. *Studia Geophysica et Geodaetica 56*(2), 411–432.

Muhumuza, K. (2015). *Modelling and inversion of time-lapse seismic data using scattering theory.* Master's thesis, University of Bergen.

Muhumuza, K., M. Jakobsen, and T. Luostari (2018). Seismic monitoring of CO 2 injection using a distorted Born T-matrix approach in acoustic approximation. *Journal of Seismic Exploration, In press.*

Oliver, D. S. and Y. Chen (2011). Recent progress on reservoir history matching: A review. *Computational Geosciences 15*(1), 185–221.

Osnabrugge, G., S. Leedumrongwatthanakun, and I. M. Vellekoop (2016). A convergent Born series for solving the inhomogeneous Helmholtz equation in arbitrarily large media. *Journal of Computational Physics 322*, 113–124.

Plessix, R., S. Michelet, and H. Rynja (2010). Some 3D applications of full waveform inversion. In *72nd EAGE Conference and Exhibition - Workshops and Fieldtrips.*

Pratt, R. G. (1999). Seismic waveform inversion in the frequency domain, Part 1: Theory and verification in a physical scale model. *Geophysics 64*(3), 888–901.

Sayers, C. and S. Chopra (2009). Introduction to this special section: Seismic modeling. *The Leading Edge* (May 2009), 528–529.

Schuster, G. T. (2017). *Seismic Inversion.* Society of Exploration Geophysics.

Snieder, R. (2004). *A guided tour of mathematical methods for the physical sciences* (2nd ed.). Cambridge: Cambridge University Press.

Tarantola, A. (1984). Inversion of seismic reflection data in the acoustic approximation. *Geophysics 49*(8), 1259–1266.

Tarantola, A. (2005). *Inverse Problem Theory and Methods for Model Parameter Estimation.* Society for Industrial and Applied Mathematics.

Virieux, J. and S. Operto (2009). An overview of full-waveform inversion in exploration geophysics. *Geophysics 74*(6), WCC1–WCC26.

Waldhauser, F. and W. L. Ellsworth (2000). A Double-difference Earthquake location algorithm: Method and application to the Northern Hayward Fault, California. *Bulletin of the Seismological Society of America 90*(6), 1353–1368.

Wang, Y. M. and W. C. Chew (1989). An iterative solution of the two-dimensional electromagnetic inverse scattering problem. *International Journal of Imaging Systems and Technology 1*(1), 100–108.

Watanabe, T., S. Shimizu, E. Asakawa, and T. Matsuoka (2004). *Differential waveform tomography for time-lapse crosswell seismic data with application to gas hydrate production monitoring*, pp. 2323–2326.

Yang, D., M. Meadows, P. Inderwiesen, J. Landa, A. Malcolm, and M. Fehler (2015). Double-difference waveform inversion: Feasibility and robustness study with pressure data. *GEOPHYSICS 80*(6), M129–M141.

Zhang, Z. and L. Huang (2013, nov). Double-difference elastic-waveform inversion with prior information for time-lapse monitoring. *GEOPHYSICS 78*(6), R259–R273.